MODELLING THE SENSITIVITY OF DENSE SHELF WATER FORMATION IN THE MERTZ GLACIER REGION, EAST ANTARCTICA

by

Eva Audrey Cougnon,
Grad. Dip. Mar. Sci., B.Sc., M.Sc. (Toulouse III, France)

Submitted in fulfilment of the requirements
for the Degree of Doctor of Philosophy

A joint program between the Commonwealth Science and Industry Research Organisation and the Institution for Marine and Antarctic Studies
University of Tasmania
June, 2016

I declare that this thesis contains no material which has been accepted for a degree or diploma by the University or any other institution, except by way of background information and duly acknowledged in the thesis, and that, to the best of my knowledge and belief, this thesis contains no material previously published or written by another person, except where due acknowledgement is made in the text of the thesis.

Signed:

Eva Audrey Cougnon

Date: June 3, 2016

Signed:

Eva Audrey Cougnon

Date: June 3, 2016

Abstract

Given the importance of the overturning circulation to global climate, there is a need to improve our understanding of Antarctic Bottom Water (AABW) formation and its sensitivity to change. The offshore properties of AABW are changing. Within the Australian-Antarctic basin AABW has freshened and decreased in volume by about 50% over the last few decades. Understanding what is driving these changes requires focusing on the key formation region along the Adélie and George V Land (AGVL) coast. Here, the intense production of sea ice in the Mertz Glacier Polynya system drives Dense Shelf Water (DSW) formation, the precursor to AABW. This thesis uses a version of the Regional Ocean Modeling System (ROMS) that has been adapted for ocean/ice-shelf interactions to explore the sensitivity of DSW formation to surface heat and salt fluxes and ice shelf basal melting.

Interannual variability in surface heat and salt fluxes drives DSW export and ice shelf basal melting variability in the AGVL region. DSW export decreases by 86% during a sustained period (2000-2002) of weak polynya activity (sea ice production) before recovering during a sustained period of stronger polynya activity (2003-2005). Basal melting of the Mertz Glacier Tongue (MGT) doubles under weak polynya activity because more warm water reaches the base of the ice shelf. Idealised simulations highlight the importance of the air/sea fluxes on DSW formation and ice shelf basal melting. A mean to strong air/sea forcing drives convection of dense water to sink at the sea floor and drives melt near the deep grounding line. Weaker air/sea forcing limits the depth of the convection and allows greater intrusions of warm modified Circumpolar Deep Water within the ice shelf cavity and increases basal melting. The resultant input of glacial meltwater produces a buoyant plume that stratifies the water column.

Two simulations are run to investigate the impact of the calving of the MGT in 2010. Weaker polynya activity after calving results in an 89% increase in area-averaged ice shelf basal melting and an 80% decrease of DSW export from the Adélie depression. Most importantly a distinct warming of the exported DSW leads

to a decrease in AABW production downstream. This thesis demonstrates the sensitivity of Antarctic ocean-cryosphere interactions to interannual variability and episodic changes to the local icescape (ice shelves, icebergs and sea ice), finding that ice shelf basal melting and DSW formation in the AGVL region is dramatically impacted by the MGT calving.

Acknowledgements

"L'océan, c'est quoi l'océan?" A question that many kids ask when they see the ocean for the first time: *"The ocean, what is the ocean?"*. This sentence is extracted from the opening of the french documentary "Océan" by Jacques Perrin and Jacques Cluzaud that built even more my passion of the ocean and my wish to understand its dynamic.

I feel lucky to have had the opportunity to study physics oceanography, particularly in the Southern Ocean and the interactions between the Southern Ocean and Antarctic ice shelves. I also feel lucky to have had the opportunity to complete this Ph.D. in Hobart with amazing people. Thank you to my supervisors, Ben Galton-Fenzi, Guy Williams, Steve Rintoul and John Hunter for your patience, your guidance and the scientific conversations over these three and a half years (and a bit!). Without you this thesis would not have been possible.

I also would like to thank Steve for providing me with the opportunity to participate on the Antarctic oceanographic voyage aboard the R.V. Tangaroa with Mike Williams (voyage chief scientist), it was an amazing experience with great people onboard. Also, thank you Guy and Franck for my second voyage opportunity on the R.V. Nathaniel B. Palmer where I had the privilege of working with Raul and others from the scientific team. During these two voyages I have met incredible people.

This PhD all became possible through an internship I completed in Hobart as part of my Masters in Toulouse. As such I would like to thank Benoit who first introduced me to the Hobart science community and polar ocean oceanography, specifically in the Mertz Glacier region, which has since become my passion and focus for the internship and later Ph.D.

This work would not have been possible without the support of several institutes: the Antarctic Climate & Ecosystems Cooperative Research Centre (ACE-CRC); the Institute for Marine and Antarctic Studies (IMAS) Quantitative Marine Science (QMS) PhD Program; and, the Commonwealth Scientific and Industrial Research

Organisation (CSIRO). I also would like to acknowledge the International Postgraduate Research Scholarship (IPRS). Computing resources were provided by both the Tasmanian Partnership for Advanced Computing and the National Computational Infrastructure under grant m68 and gh8.

Thank you Wen, Claire and Christine for your support, particularly in the in the last few months of my thesis. You have made the administration side of the thesis a lot smoother. When a month before submitting, my computer crashed, thank you Tze for saving all my data.

This thesis would not have been possible without the support of many other friends in Hobart, at ACE-CRC, IMAS and beyond. It is impossible for me to name everyone. However some specific groups of people made this experience what it has been. All those involved in Joga Bonito, thank you for the friendly and relaxing football (soccer) games, no matter the weather. The Tas Uni Dive Club and other dive buddies, for all the amazing dives around Tasmania. The Cream Horns and the Drop Scones for awesome touch football games when I was writing.

I would like to specifically thank a few particularly close friends who were always there for me during the PhD. Alyce and Eleri for volunteering to proof-reading this manuscript, and enlightening some of my ideas. Dave, Mauro, Alex, Eric, Jessica and Sjoerd for your help and advices when I had a science questions. Mana, Molly, Julie, and Mauro for your patience in listening to my brain storming sessions and then numerous complaints during our tea breaks, when I know all you wanted to do was have a relaxing cup of tea! This Ph.D. would never have been possible if it wasn't for the amazing life I had outside of the PhD. Thank you to Lauren, Malou, Vero and Alyce for all the amazing hikes, surfing and snorkelling sessions. Also thank you to my housemates at Cartela, Aal, Elias, Trent, Josie and Rowena for all the great moments we had at home. Back in France I would like to thank Anne, Nina and my friends in Brest where I wrote the final words of my thesis. It was such an amazing place to finish this amazing journey, particularly with my writing spot in the library with a amazing view facing the ocean.

Thank you all for your smiley faces, a smile always makes the day better.

Finally, gracias Javier for your support and guidance, particularly at the end of the Ph.D. where you always made sure I had an amazing meal ready to fill my stomach and relax my mind. Thank you.

"Sous la mer vous cherchez le passé, vous allez découvrir le futur"

–

Jean Cocteau

Statement of Co-Authorship

The following people contributed to the publication of work undertaken as part of this thesis:

Paper 1 / Chapter 2 (Modeling interannual dense shelf water export in the region of the Mertz Glacier Tongue (1992-2007)):

- **Eva A. Cougnon**, University of Tasmania (70%)
- Benjamin K. Galton-Fenzi, Australian Antarctic Division (15%)
- Andrew J. S. Meijers, British Antarctic Survey (10%)
- Benoit Legrésy, Commonwealth Scientific and Industrial research Organisation, Marine and Atmospheric Research (5%)

Details of the authors roles:

Benjamin K. Galton-Fenzi contributed with extensive project development and refinement, technical and conceptual aspects, and manuscript preparation.

Andrew J. S. Meijers contributed with project development and refinement, and assisted extensively with technical and conceptual aspects of this research.

Benoit Legrésy contributed with concept development and manuscript development.

We, the undersigned, agree with the above stated "proportion of work undertaken" for each of the above published peer-reviewed manuscripts contributing to this thesis:

Signed:

Dr. Benjamin K. Galton-Fenzi

Supervisor
Australian Antarctic Division, and
Antarctic Gateway Partnership, and
Antarctic Climate & Ecosystems Cooperative Research Centre

Date: June 3, 2016

Signed: _____
Prof. Nathan Bindoff

Head of school
Oceans and Cryosphere Program
Institute for Marine and Antarctic Studies

Date: October 31, 2016

TABLE OF CONTENTS

LIST OF TABLES

LIST OF FIGURES

Chapter 1

Introduction

Since its discovery more than a century ago, the region of the Mertz Glacier has intrigued explorers and now many scientists. Sir Douglas Mawson left Hobart, Tasmania in 1911, to lead the Australasian Antarctic Expedition in an unexplored area south of Australia; the Adélie and George V Land. He arrived at Cape Denison in Commonwealth Bay, and realised that this region was unique. In fact, this area is one of the windiest regions in the world. An account of the expedition can be found in his book *"The Home of the Blizzard"* [Mawson 1915].

It was only at the end of the 20^{th} century that scientists realised the importance of this particular region to the global ocean circulation. Understanding the interactions and impacts of the Antarctic continental ice on the formation of dense water masses is an emerging field and the primary motivation for this thesis. In this chapter, an overview of the role of the global ocean circulation and the importance of the Antarctic ice sheet in a global context is presented before focusing on the region of interest.

1.1 Antarctic Bottom Water

1.1.1 Thermohaline circulation and the Southern Ocean

A key component of global climate is the overturning circulation of the ocean that is formed due to surface water losing sufficient buoyancy from air/sea and sea ice exchanges to sink to the sea floor [Orsi et al. 1999]. The global overturning circulation is responsible for storing large amounts of heat and carbon in the oceans, and therefore has a direct and strong influence on the rate of climate change. Accord-

ing to Rhein et al. [2013], ∼93% of the global heat increase has been stored in the world's oceans over the past 50 years. The Southern Ocean also has a key role in the uptake and storage of anthropogenic carbon dioxide (CO_2) emissions [Sabine et al. 2004; Le Quéré et al. 2009; Siedler et al. 2013, *(Chapter 30)*].

Deep water formation sites that produce North Atlantic Deep Water (NADW) and Antarctic Bottom Water (AABW) are in specific locations in the North Atlantic Ocean and around Antarctica, respectively (Figure 1.1). NADW is formed via deep convection in the Greenland and Labrador Seas and flows southward at mid depths to the Antarctic Circumpolar Current (ACC) in the southwestern Argentine Basin. Thereafter it circulates eastward within the ACC to mix with local water masses to become Circumpolar Deep Water (CDW) [Orsi et al. 1999]. AABW is the densest water mass in the global ocean and spreads northward from Antarctica into the abyssal Southern Hemisphere Ocean, mixing into overlying deep water [Orsi et al. 1999]. The overlying deep water corresponds to the NADW that flows southward and is lighter than AABW.

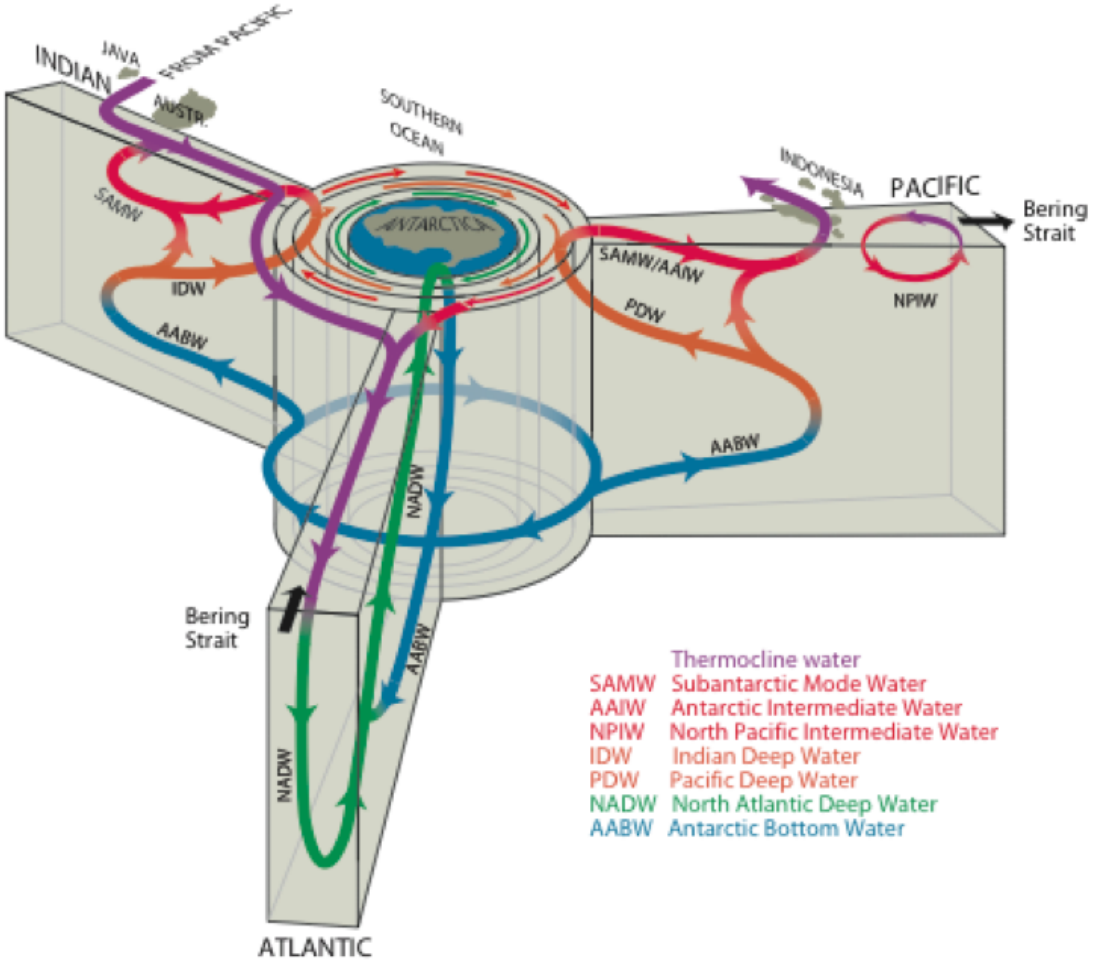

Figure 1.1: Global overturning circulation schematics from a Southern Ocean perspective. *Source: from Talley [2011], after Gordon [1991], Schmitz [1996] and Lumpkin and Speer [2007].*

AABW is produced from Dense Shelf Water (DSW) formed in discrete locations around the Antarctic continent by atmospheric cooling, brine rejection (sea ice formation), and interactions with Antarctic ice shelves (Figure 1.2), such as in the regions of the Weddell Sea, Ross Sea and Adélie Land, in the East Antarctica [e.g. Rintoul 1998; Orsi et al. 1999; Jacobs 2004]. More recently, other sources have been found in East Antarctica, in particular near Cape Darnley immediately west of the Amery Ice Shelf [Kusahara et al. 2010; Fukamachi et al. 2010; Ohshima et al. 2013] and from Vincennes Bay [Kitade et al. 2014]. When exported from the continental shelf, this dense water mixes with relatively warm (>0 °C) CDW to form AABW [Reid 1979].

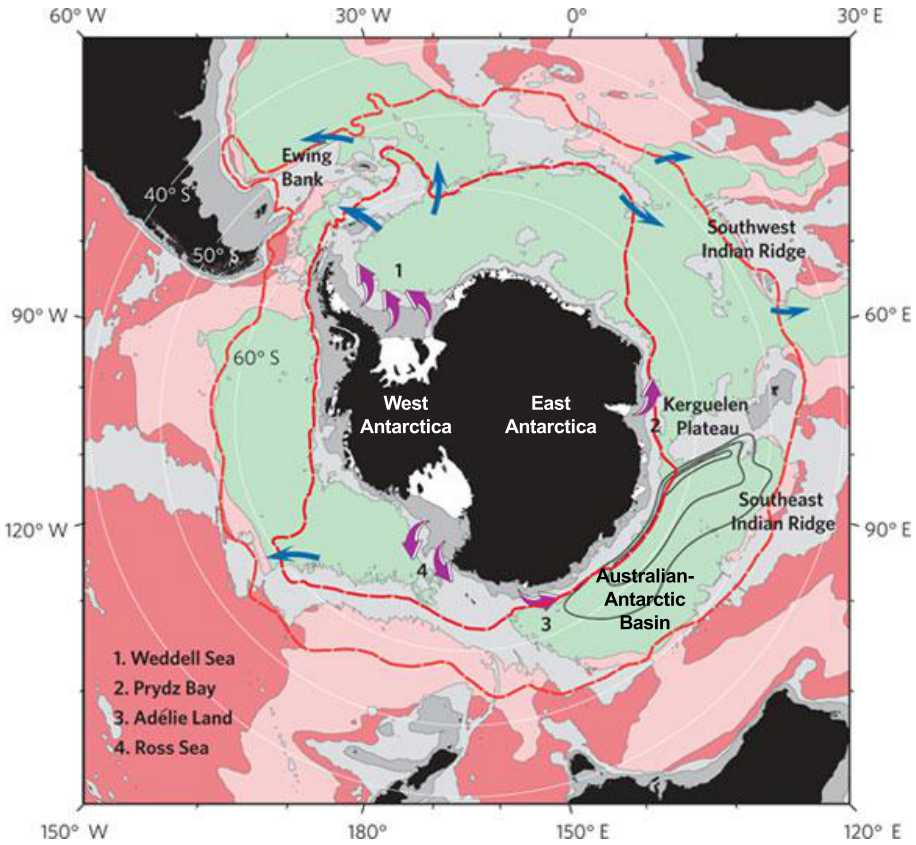

Figure 1.2: Main regions of AABW outflow from the continental shelf (purple arrows) and in the abyssal ocean (blue arrows). The location of AABW from the 4 main sources (labelled on the figure) is shown in green. The areas of pink shades represent AABW after mixing with the Antarctic Circumpolar Current deep water (located within the red contours). *Source: Orsi [2010].*

1.1.2 Australian-Antarctic Basin

AABW in the Australian-Antarctic basin is a mixture of two types of Bottom Water defined by their region of formation (Figure 1.2). Ross Sea Bottom Water (RSBW) enters the basin from the east and is relatively warm, saline and oxygen-poor compared to the second water mass found in the basin. This second water mass is the Adélie Land Bottom Water (ALBW) that is formed locally along the Adélie and George V coast. ALBW is colder and fresher than RSBW and is also oxygen-rich [e.g. Rintoul 1998]. This mixture of RSBW and ALBW within the Australian-Antarctic basin contributes significantly to the total AABW production. Orsi et al. [1999] suggest that this mixture should contribute as much as 40% of the total AABW production but neglects more recently found sources.

Within the Australian-Antarctic basin, AABW has freshened, [Aoki et al. 2005; Rintoul 2007; Shimada et al. 2012; Aoki et al. 2013] warmed and decreased in volume by about 50% over the last four decades [van Wijk and Rintoul 2014]. The observed changes in AABW properties (potential temperature, salinity, density and volume) are not fully understood. To understand these changes better, it is important to investigate the water properties of the two sources, ALBW and RSBW, their rate of production, and their interactions with the icescape (sea ice, ice shelves and icebergs) near the Antarctic continent.

1.2 Antarctic ice sheet and Southern Ocean

1.2.1 Antarctic ice sheet mass balance and sea level rise

Ice sheets are the main control on sea level over millennia and longer time scales [*Chapter 2:* Siedler et al. 2013]. The largest ice sheet on Earth is the Antarctic ice sheet, and accurate estimates of its mass balance are important for sea level rise predictions and climate variability. The Antarctic ice sheet has a potential contribution to sea level rise of 58 m on the global ocean [Fretwell et al. 2013]. The West Antarctic ice sheet has the greatest observed thinning for the Antarctic continent, and has accelerated over the present decade [e.g. McMillan et al. 2015; Flament and Rémy 2012]. The average rate of thinning between 2010 and 2013 was 31% higher than it was during the period 2005-2010, while in East Antarctica and along the Antarctic Peninsula, the average change in ice sheet mass remains small [McMillan et al. 2015], but the uncertainties in ice-mass changes remain large [Hanna et al. 2013].

The Antarctic ice sheet drains into the Southern Ocean through floating ice shelves around the continent. As a result, ice shelves are the link between the Antarctic ice sheet and the Southern Ocean. Ice shelf basal melting and iceberg calving into the Southern Ocean are the main processes for Antarctic ice sheet mass loss [Pritchard et al. 2012]. Most of the Antarctic ice shelves are thinning and ocean driven basal melting is responsible for twice the ice shelf mass loss compared to iceberg calving [Liu et al. 2015; Depoorter et al. 2013; Pritchard et al. 2012]. Ice shelves around Antarctica buttress the flow of the grounded Antarctic ice sheet onto the Southern Ocean. The thinning of an ice shelf decreases the buttressing effect on the ice sheet and increases the ice sheet discharge onto the ocean [Paolo et al. 2015; Pritchard

et al. 2012]. Antarctic ice shelves have been observed to be thinning over recent decades, mainly in West Antarctica. Paolo et al. [2015] estimate an increase of about 70% of the mass loss in West Antarctica in the past decade, while East Antarctica seems to be stable overall after gaining volume during the previous decades with some regional differences.

The East Antarctic ice shelves are particularly important in that they buttress an ice sheet that includes more than 73% of the Antarctic grounded ice sheet below mean sea level (marine ice sheet) [Fretwell et al. 2013]. The implications of a marine ice sheet can be dramatic when the ice shelf is unstable [Schoof 2007; Gudmundsson 2013]. If the grounding line (transition between grounded ice sheet and floating ice shelf) retreats on bedrock that deepens inland, the ice shelf can be unstable under specific conditions [Gudmundsson 2013], increasing the ice shelf discharged rate and subsequently increasing the retreat of the grounding line and releasing more fresh glacial meltwater into the Southern Ocean. Thus, ocean/ice shelf interactions play an important role in controlling the flow of the grounded ice sheet into the ocean, and thereafter the ice shelf basal melting and input of glacial meltwater into the ocean that may contribute to the freshening of water masses on the continental shelf.

1.2.2 Different modes of sub-ice shelf melting

Ice shelf basal melting produces a buoyant, fresh and cold (colder than the surface freezing temperature) water-plume that rises along the underside of the ice shelf, giving rise to 'ice pump' circulation [Lewis and Perkin 1986]. This fresh water plume interacts with the surrounding water masses to form Ice Shelf Water (ISW). Jacobs et al. [1992] describe three different modes of ice shelf basal melting related to the ocean circulation. Intense sea ice formation in specific areas around Antarctica and associated brine rejection drive convection of the relatively dense High Salinity Shelf Water (HSSW), which sinks at the sea floor and can flow below local ice shelves. At depth, HSSW is warmer than the *in situ* freezing temperature that decreases with depth as a result of increasing pressure, and hence the flow of HSSW can drive ice shelf basal melting (Figure 1.3). This melting is concentrated in the deepest part of the ice shelf cavity and corresponds to mode 1 of the sub-ice shelf melting scenarios described by Jacobs et al. [1992].

The second mode of sub-ice shelf melting is related to an inflow of relatively warm

modified CDW (mCDW) accessing the continental shelf and the ice shelf cavity at the sea floor. In the Pine Island Glacier area, in West Antarctica, *in situ* temperatures near the grounding zone of the ice shelf are almost 4 °C above the *in situ* freezing temperature [Jacobs et al. 2011]. This mode can drive strong melting where warm water interacts with the ice shelf. On large ice shelves the inflow can also be restricted in an area with part of the heat available recirculating outside of the ice shelf cavity. Lastly, mode 3 melting is related to shallower processes, where summer surface water and tidal processes interact with the upper part of the ice front to drive melting. In the next section, gaps and uncertainties about the impact of the glacial meltwater input on AABW production, from the ice shelves to the continental slope, are presented.

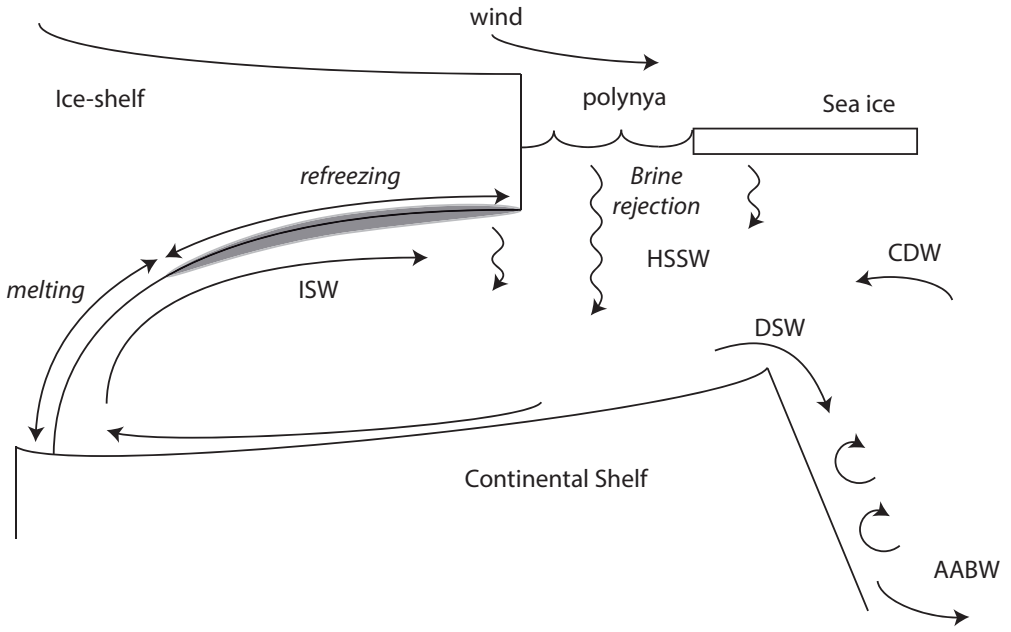

Figure 1.3: Schematic of wintertime ocean/ice shelf processes and description of the 'ice-pump' mechanism. Winds blow from the Antarctic continent and freeze the ocean to push the sea ice away (polynya, see Section 1.4.2) forming High Salinity Shelf Water (HSSW) due to the brine rejection. HSSW can sink at the sea floor and interact with the ice shelf at depth, forming Ice Shelf Water due to the release of glacial meltwater. The buoyant plume released by the melting can refreeze at shallower depth underneath the ice shelf. Dense Shelf Water (DSW) is the result of HSSW, ISW and Circumpolar Deep Water (CDW) inflowing onto the shelf that mixes with surrounding water masses. DSW then flows across the shelf break and descend the slope to contribute to the Antarctic Bottom Water (AABW) formation. *Adapted from Galton-Fenzi et al. [2012].*

1.3 Gaps around AABW sensitivity to ice shelf melting

1.3.1 Uncertainties about AABW variability

Long term analyses of AABW properties within the Australian-Antarctic basin have shown important trends and interannual variability that are not yet fully explained. Aoki et al. [2013] noticed a sustained freshening in the variation of bottom water properties of the Australian-Antarctic basin from measurements between 1994 and 2012. van Wijk and Rintoul [2014] observed that the volume of AABW (with neutral density (γ^n) > 28.30 kg m^{-3}) decreases in thickness at a rate of > 100 m per decade. As mentioned before, AABW found in the Australian-Antarctic basin is a mixture of a locally formed bottom water (ALBW) and of RSBW. Jacobs and Giulivi [2010] and Shimada et al. [2012] observed a freshening of the RSBW that could explain part of the freshening observed within the Australian-Antarctic basin. However, interannual variability from the ALBW source is also likely to be important to the ALBW production, given that variability in sea ice production (atmospheric variability) or major changes in the icescape would affect the formation rate of DSW that contributes to the ALBW formation.

The impact of ocean/ice shelf interactions on DSW formation and subsequent AABW formation is still poorly known. Most of the uncertainties in global climate models, used in CMIP5, are related to biases in the Southern Ocean water masses [Sallée et al. 2013]. Therefore, improving our understanding of ocean/ice shelf and continental shelf processes around Antarctica has become a priority for ice sheet and oceanographic based studies, as well as climate projections. In regions where HSSW drives ice shelf basal melting (mode 1 melting [Jacobs et al. 1992]), meltwater mixes with locally formed water masses (on the continental shelf), such as with HSSW as described earlier. In this case, glacial meltwater has a cooling and freshening impact on HSSW and subsequent DSW. Therefore, water mass properties on the continental shelf will likely be impacted by an increase of the basal ice shelf melt rate (increase in glacial meltwater input). The rate at which sea ice forms controls the salinity of HSSW formed on the continental shelf. As a result, the vertical convection due to brine rejection is directly affected by sea ice production variability, and impacts on water masses that are entrained by this vertical convection.

Other factors may also drive variability in water mass properties on the continental

shelf, such as CDW intrusions that modify shelf water properties and the subsequent DSW. CDW intrusions are highly associated with the bathymetry at the shelf break [e.g. Walker et al. 2007; Moffat et al. 2009; Wåhlin et al. 2010; St-Laurent et al. 2013]. At high latitudes, due to a small radius of deformation, small scale bathymetry features such as troughs, will lead CDW onto the continental shelf. For instance, St-Laurent et al. [2013] describe three mechanisms that are able to maintain warm water within the ice shelf cavity in the presence of a trough: deep onshore flow can be driven by strong ice shelf meltwater outflow, interactions between the mean flow along the shelf break and the trough, and the interactions of the Rossby wave along the shelf break and the trough due to the small radius of deformation. Dinniman et al. [2011] also demonstrated the strong relation between along shelf break wind stress and warm water intrusion events in the West Antarctic Peninsula.

1.3.2 Limited observations beneath ice shelf

Collecting oceanographic data around the Antarctic continent is an onerous and expensive task and often limited to measurements during summer. This task becomes even harder when attempting to make observations beneath ice shelves and on the continental shelf where sea ice impacts shipping routes. Hydrographic data beneath ice shelves have been measured by drilling boreholes [e.g. Nicholls et al. 2001; Herraiz-Borreguero et al. 2013; 2015], and Autonomous Underwater Vehicles (AUV) have been deployed underneath a few Antarctic ice shelves to describe the ocean circulation and water mass properties within the ice shelf cavity [e.g. Nicholls et al. 2006; Dutrieux et al. 2014]. More recently, Autonomous Phase-sensitive Radio Echo Sounders have been deployed on top of the ice shelf to monitor the basal melt rate and deformation of an ice shelf [Nicholls et al. 2015]. While these techniques are a big step forward, their deployments remain sparse around the Antarctic margin.

Modelling studies need to be combined with these observational studies to improve our knowledge of ocean/ice shelf processes which are difficult to measure. Ocean/ice shelf modelling is an emerging field and many uncertainties still remain. In an ocean model that includes ocean/ice shelf thermodynamics, the accuracy of the ice shelf draft and bathymetry (within the ice shelf cavity as well as on the continental shelf) is crucial to reduce uncertainties. The shape of the ice shelf base controls the melt rate estimates. For instance, an ice shelf base with a steep slope will have its melting enhanced by the buoyant meltwater plume rising along the base of the ice shelf and

driving stronger melting than an ice shelf with a gentle slope. Little et al. [2009] indicate that the ice shelf shape can influence the basal melting as strongly as ocean properties on the continental shelf.

As described earlier, the bathymetry at the shelf break is an important control on the access of relatively warm CDW onto the continental shelf. The presence or absence of troughs between the shelf break and ice shelf is thought to be critical for CDW to access the ice shelf cavity. However, for most regions around Antarctica, the bathymetry on the continental shelf and in particular beneath the ice shelves is poorly known. As an example, radar sounding measurements, which aim to estimate the ice shelf thickness as well as the bathymetry of the sea floor, have revealed small features (troughs) underneath the Totten Ice Shelf (East Antarctica) [Greenbaum et al. 2015] that could provide an alternate route to lead relatively warm water towards the grounding line. Gwyther [2015, *Chapter 6*] has used a regional ocean model to estimate the melt rates of three different ice shelf cavities of the Totten Ice Shelf, both with and without the trough revealed in Greenbaum et al. [2015]. Gwyther [2015, *Chapter 6*] found that the area-average melt rate is similar between the three geometries but the greatest change is seen in the spatial distribution of the basal melting. Schodlok et al. [2012] have shown similar results for the Pine Island Glacier (West Antarctica), using two bathymetries to study the role of the ocean on the ice shelf mass loss. The more up-to-date bathymetry leads to a 25% increase in the melt rate.

1.4 Region of interests

1.4.1 DSW production in the AGVL region

The Adélie and George V Land (AGVL) is one of the most monitored region in East Antarctica with many studies covering the ice draft of the main ice shelf in the area; the Mertz Glacier Tongue (MGT) [e.g. Legrésy et al. 2004], the continental shelf and slope bathymetry [e.g. Beaman et al. 2011], and the ocean circulation [e.g. Bindoff et al. 2000; Williams and Bindoff 2003; Williams et al. 2008; 2010; Lacarra et al. 2011; 2014; Shadwick et al. 2013]. The AGVL region was not considered as an important source of AABW until the mid to late 1990s. AABW within the Australian-Anatrctic basin was known from the 1970s [Gordon and Tchernia 1972] but thought to be primarily a mixture of the RSBW and WSBW with some

negligible contribution from the AGVL coast [Carmack 1977]. Using measurements from the 1990s, Rintoul [1998] estimated the contribution of ALBW to be 25% of total AABW formation (66% from the WSBW, and 7% from the RSBW), and Fukamachi et al. [2000] detected the injection of cold ALBW at 140 °E, using data from offshore moorings.

The first and so far only wintertime experiment within the AGVL region occurred in winter 1999 (July to August) [Bindoff et al. 2001; Williams and Bindoff 2003]. These wintertime analyses together with summer hydrographic data and year-round mooring observations [Williams et al. 2008; 2010] have shown that DSW accumulates within the Adélie depression, flowing across the shelf break and contributing to ALBW production (Figure 1.4). The export of DSW across the shelf break at the main pathway outflow was estimated to be about 0.1-0.5 Sv by Williams et al. [2008]. They also described that the circulation on the continental shelf is driven by HSSW due to the high rate of sea ice production as seen on Figure 1.4, interacting with the local ice shelf (MGT) and the inflowing mCDW onto the continental shelf to form DSW that flows across the shelf break and downslope. Lacarra et al. [2011] uses summer hydrographic observations to reconstruct the summer water mass distributions on the continental shelf and confirm the ocean circulation within the depression described by Williams et al. [2008].

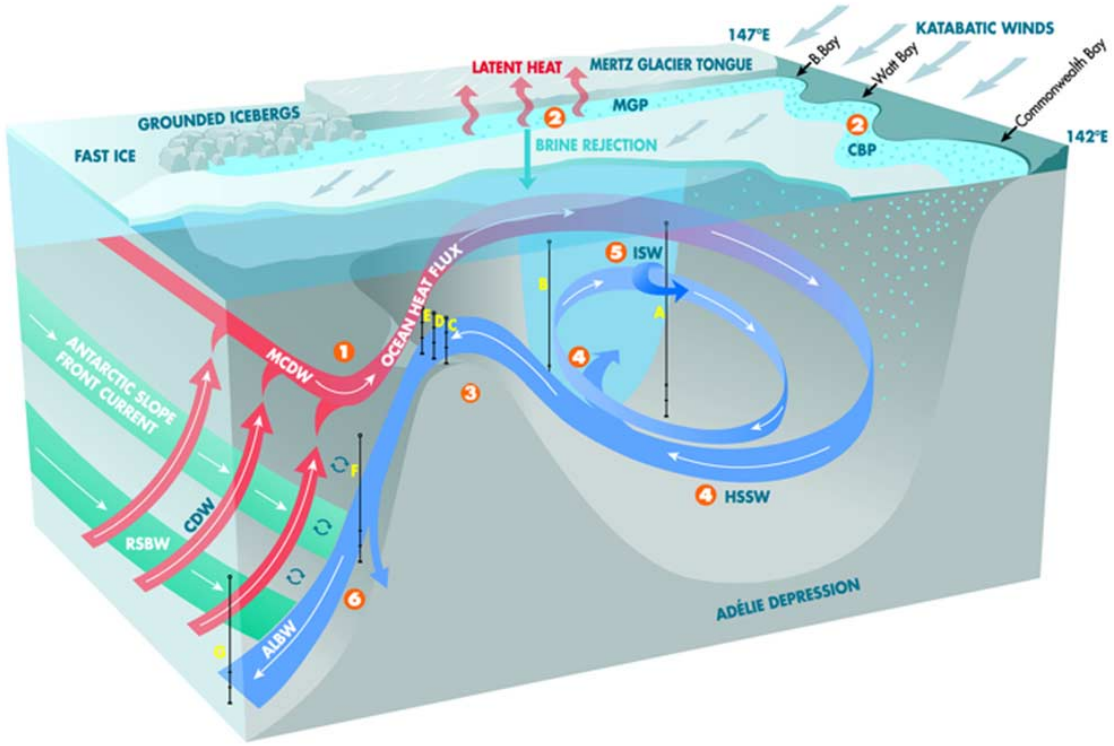

Figure 1.4: A schematic diagram of the circulation in the Adélie Depression and the processes involved in the production of ALBW. Numbers represent the following: 1, modified Circumpolar Deep Water (MCDW) intrusions; 2, brine rejection beneath Mertz Glacier Polynya (MGP) along the Mertz Glacier Tongue (MGT) and in the Coastal Bay Polynya (CBP) region including Commonwealth, Watt, and Buchanan bays; 3, Dense Shelf Water (DSW) export through the Adélie Sill; 4, High Salinity Shelf Water (HSSW) circulation at the base of the depression and beneath the MGT; 5, Ice Shelf Water (ISW) in Buchanan Bay in a cold, fresh westward coastal current; and 6, downslope mixing of DSW contributing to the production of ALBW. *Source: Williams et al. [2008].*

1.4.2 Importance of polynyas

Relative to the large continental embayments where AABW is formed in the Weddell and Ross seas, the formation of ALBW is located in a restricted latent heat polynya area called the Mertz Glacier Polynya (MGP). Polynyas are regions of open water within the ice pack, and are categorised into sensible and latent-heat varieties (Figure 1.5). Sensible heat polynyas (Figure 1.5a) are thermally driven and are formed due to relatively warm water that upwells to the surface and melts any pre-existing ice to prevent the growth of new sea ice [Morales Maqueda et al. 2004]. For instance, in the Canadian Arctic several sensible heat polynyas are found due

to the presence of relatively warm water reservoir at depth and strong tidal mixing [Hannah et al. 2009]. In this case, no sea ice is produced and therefore there is no DSW formation. It is important to note that sensible heat polynyas are different from "leads" that are small breaks between ice floes.

Latent heat polynyas (Figure 1.5b) are related to a change in the phase of the sea water that freezes at the surface of the ocean. These polynyas are wind-driven and often located in specific regions along the coast or along an ice shelf edge. The location of the polynyas along the coast is determined by the presence of gravity winds (katabatic winds) in certain regions where the topography channels the gravity-fed winds from the interior of the continent. Katabatic winds act to maintain the open water area of the polynya by actively driving any newly-formed sea ice away. These regions are also called "ice factories" as they generate a very large amount of sea ice growth relative to the average sea ice pack, and subsequently a large amount of brine-rejection. This is the main mechanism to form very dense water on the continental shelf. In the strongest polynyas this results in wintertime convection throughout the water column and the formation of DSW.

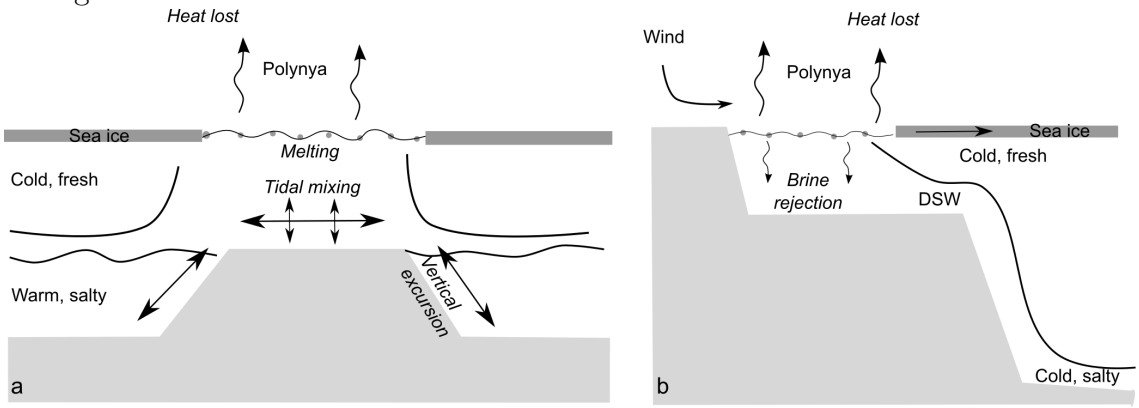

Figure 1.5: Schematics of polynya formation. Sensible heat polynyas (a) are driven by the presence of relatively warm water that is able to reach the sub-surface [after Hannah et al. 2009] and latent heat polynyas (b) are driven by winds from the continent that push the sea ice away and contribute to the formation of Dense Shelf Water (DSW). *Adapted from Talley [2011].*

The AGVL coast has the strongest katabatic wind regime of anywhere in Antarctica [Wendler et al. 1997]. Mawson [1915] was the first to measure the strength and duration of the storms in Commonwealth Bay (see Figure 1.6 for location) during his expedition in 1911-1914 and called this region "The Home of the Blizzard". The factors influencing the formation of the MGP are the MGT which forms a topographical barrier (140 km long 25 km width) and prevents the westward advection

of sea ice along the coast, as seen on Figure 1.6. Inland ice-sheet topography also funnels strong and persistent katabatic winds from the continent to enhance rapid sea ice formation. The MGP is one of the largest coastal polynyas in East Antarctica [Massom et al. 1998; Tamura et al. 2008]. These strong and persistent winds influence the ocean by driving strong bottom salinity due to strong brine rejection convecting through the whole water column in particular within Commonwealth Bay [Lacarra et al. 2011].

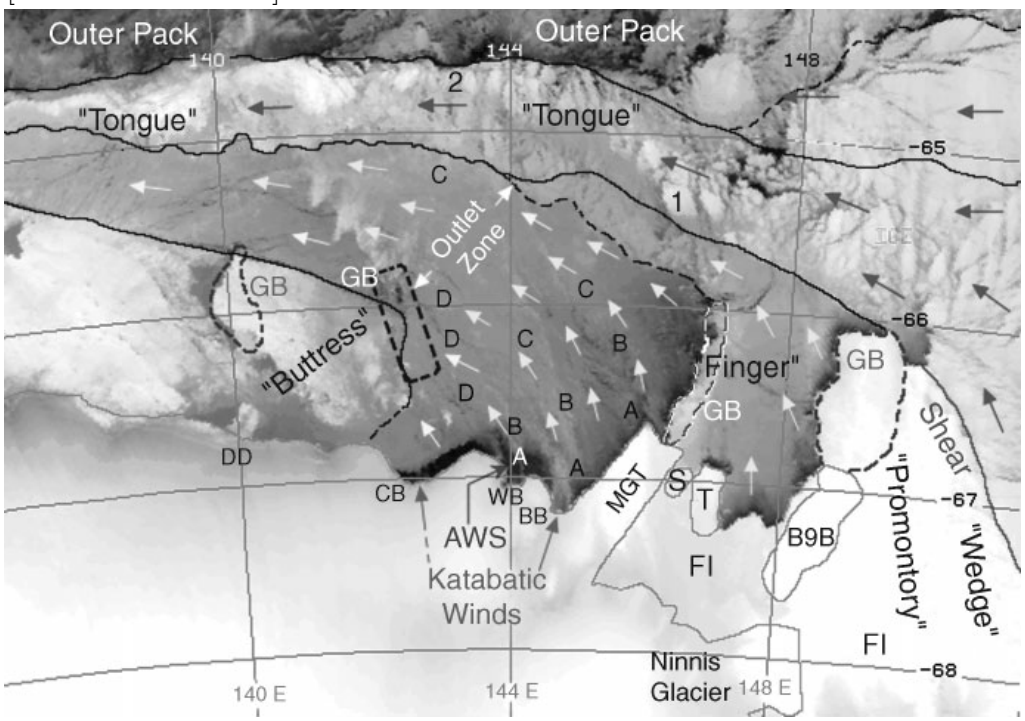

Figure 1.6: Satellite imagery of the Mertz Glacier Polynya, taken from Massom et al. [2001]. Dumont d'Urville (DD), Commonwealth Bay (CB), Watt Bay (WB) and Buchanan Bay (BB) are shown. The MGT and extended region of grounded icebergs (labeled "finger") are outlined, with the 1999 position of the Ninnis Glacier tongue. Other areas of grounded bergs are labeled GB and are estimates. FI refers to fast ice and the large iceberg B9B is also shown. Arrows denote the approximate large-scale ice-drift direction (light denote new ice, dark denote thick, multi-year and broken-out ice).

1.4.3 Major Calving of the Mertz Glacier in 2010

In February 2010, the MGT calved and reduced its length by about half of its original size to become about 80 km long. The B9B iceberg, previously grounded east of the MGT, became ungrounded and collided with the MGT. This movement changed the ocean circulation via the tidal regime around the MGT during the calving event, and

possibly triggered the MGT calving [Mayet et al. 2013] that was already weakened by two large rifts [Lescarmontier et al. 2015]. This calving event led to a decrease of 14 to 20% of the sea ice production in the region [Tamura et al. 2012] and a freshening and lightening of the densest water mass on the continental shelf that likely reduced the production of ALBW [Shadwick et al. 2013; Lacarra et al. 2014]. Modelling studies in the AGVL region have shown similar results. Kusahara et al. [2011b] estimate a reduction in DSW outflow (across the shelf break) of 23% from the AGVL region associated with a decrease in density of the outflowing DSW. It is important to note that the model used in Kusahara et al. [2011b] does not incorporate sub-ice shelf processes, with ice shelves treated as land [Kusahara et al. 2010].

Interannual variability of sea ice production is also known to have an important impact on the DSW production and bottom salinity, as shown by the observations [Shadwick et al. 2013; Lacarra et al. 2014] and modelling studies [Marsland et al. 2004; Cougnon et al. 2013]. From the observations pre-calving, the year-to-year summer bottom salinity changes could reach 0.12 in the area with the highest sea ice production, while in the same area after the calving event, the salinity dropped by 0.15 between 2010 (pre-calving) and 2011 (post-calving) [Lacarra et al. 2014]. Modelling studies with pre-calving conditions have shown the importance of atmospheric interannual variability on DSW formation. Marsland et al. [2004] focussed on the interannual variability and estimated a 60% increase of the DSW outflow between a period of relatively weak polynya activity (low sea ice production rate) and a period with strong polynya activity (high sea ice production rate) during the pre-calving conditions. Results from Cougnon et al. [2013] are discussed in Chapter 2 of this thesis.

1.4.4 Modelling the region

In this study, the main results are drawn from a regional model used to study the interannual variability of the DSW outflow and the ice shelf basal melt rate of the MGT with the heat and salt fluxes (sea ice production) interannual variability. A modified version of the three-dimensional Regional Ocean Modeling System (ROMS) [Shchepetkin and McWilliams 2005] is used in this study. This modified version of ROMS includes ocean/ice shelf and frazil thermodynamics following the model set up in Galton-Fenzi et al. [2012]. Also, ROMS has a free surface and uses

terrain-following vertical s-coordinates system, which has been adapted to allow the coordinates to follow the ice shelf draft, as used in several studies around Antarctica [e.g. Dinniman et al. 2007; Mueller et al. 2012; Galton-Fenzi et al. 2012; Gwyther et al. 2013; Hattermann et al. 2014]. The vertical coordinates allow a higher resolution at the bottom and at the surface of the water column, including just below the ice shelf, to better parameterise the ocean/ice shelf interactions.

The ocean/ice shelf thermodynamics in the model are described by three equations representing the conservation of heat, salt and a linearised version of the freezing temperature, as a function of salinity and pressure, as described in Holland and Jenkins [1999]. These equations are also dependant on the friction velocity, defined in terms of the shear stress at the ocean/ice shelf interface. This parameterisation allows melting and freezing at the ocean/ice shelf boundary. Also, frazil ice formation within the water column, in particular within the sub-ice shelf layer, is allowed and parameterised as in Galton-Fenzi et al. [2012]. Frazils are ice crystals formed in polynyas and leads, and is the first stage of pancake ice formation (grease) when waves are present. They are also formed underneath the ice shelf, within a supercooled layer adjacent to the ice shelf, when the buoyant glacial meltwater rises along the base of the ice shelf. This is due to the local freezing temperature that increases with decreasing pressure. Large accretion of frazil ice crystals beneath an ice shelf leads to the formation of marine ice and can enhance the ice shelf stability by insulating the ice shelf from the direct impact of the ocean [Holland et al. 2009; Craven et al. 2009].

The bathymetry and the ice shelf draft are based on RTopo-1 [Timmermann et al. 2010]. For the AGVL region, RTopo-1 is a combination of data from GEBCO [Smith and Sandwell 1997] for the ocean and an ice draft estimated with BEDMAP topography [Le Brocq et al. 2010]. For this study, RTopo-1 is modified to include local high-resolution bathymetry data from Beaman et al. [2011] based on multibeam swath sonar and singlebeam bathymetry data with about 250 m resolution for the AGVL region (138-148°E and 63-69°S). This local high resolution bathymetry significantly improve the the complexity of the glacial trough on the continental shelf as well as the spatial distribution of the submarine canyons on the continental slope [Beaman et al. 2011]. The iceberg positions and the MGT ice draft were created using high-resolution SPOT5 imagery and radar profiles from Legrésy et al. [2004], and more recent airborne radio echo sounding (ICECAP project from International Polar Year and Greenbaum et al. [2010]). The bathymetry beneath the MGT has

been created to accommodate the grounding line position and thickness [Legrésy et al. 2004] and is similar to Mayet et al. [2013].

Small features, such as grounded icebergs, are important for the formation of polynyas in the region (see Section 1.4.2). Coastal polynyas and icebergs are often poorly resolved in modelling studies due to the low resolution of winds that does not resolve katabatic winds, or are not parameterised. Katabatic winds are crucial in the representation of buoyancy fluxes resulting from the polynya as detailed in Section 1.4.2, removing heat from the ocean and releasing salt into the ocean. Therefore, heat and salt fluxes based on sea ice concentration observations derived from Special Sensor Microwave Imager (SSM/I) from 1992 to 2013 [Tamura et al. 2016] following Tamura et al. [2011] are prescribed in this study to force the open ocean surface of the model. During summer, the Tamura et al. [2016] data are supplemented with open-water heat and salt fluxes using monthly climatologies from the European Centre for Medium-Range Weather Forecast Re-Analysis data (ERA-Interim) or the National Centers for Environmental Prediction/Department of Energy Re-Analysis data (NCEP2) data base.

1.5 Aim and thesis outline

In this thesis, the interannual variability of the MGT basal melting and the DSW export from the Adélie and George V Land region before and after the Mertz calving is investigated with the previously described ocean/ice shelf model. Interannual variability in sea ice production and episodic changes to the coastal icescape are part of the natural forcing around Antarctica. DSW production and ice shelf basal melting can be dramatically impacted by these events. This study aims to understand the sensitivity of DSW formation, the main source of AABW in East Antarctica, to variability in surface fluxes and glacial meltwater. AABW formation, downstream of the AGVL region is also quantified.

This thesis is structured as follows:

- **Chapter 2** investigates the influence of the interannual variability in surface heat and salt fluxes in driving DSW export and ice shelf basal melting variability in the AGVL region for pre-calving conditions and compares the model results with other studies.

- **Chapter 3** uses idealised two-dimensional (no Coriolis) overturning numerical simulations to further investigate the sensitivity of ice shelf basal melting and DSW export to changes in air/sea forcing intensity and associated changes in vertical convection.

- **Chapter 4** investigates the impact of the MGT calving on its basal melting, as well as basal melting of two other ice shelves east of the MGT. Ocean properties within other ice shelf cavities in the region are also studied in this chapter.

- **Chapter 5** uses the same set of simulations as presented in Chapter 4 to investigate the ocean circulation changes on the continental shelf and changes in DSW properties and export after the calving event. The impact on the downslope flow of newly-formed AABW is also investigated to quantify the impact of the calving event on AABW downstream of the AGVL.

- **Chapter 6** summarises the key findings before opening a discussion on future work.

Chapter 2

Modelling interannual dense shelf water export in the region of the Mertz Glacier Tongue (1992-2007)

The following chapter is sourced from the peer-reviewed article: Cougnon, E. A., Galton-Fenzi, B. K., Meijers, A. J. S., and Legrésy, B. (2013). Modeling interannual dense shelf water export in the region of the Mertz Glacier Tongue (1992-2007). *Journal of Geophysical Research: Oceans*, 118(10):5858-5872. It has been edited for formatting and the abstract has been removed. The content remains unaltered.

2.1 Introduction

Antarctic Bottom Water (AABW) is an important part of the global thermohaline circulation, and is known to form in the Weddell Sea, Ross Sea and Adélie Land [Rintoul 1998; Orsi et al. 1999; Jacobs 2004]. More recently, AABW has been observed to form in the vicinity of Cape Darnley, located immediately west of the Amery Ice Shelf [Tamura et al. 2008; Kusahara et al. 2010; Fukamachi et al. 2010; Ohshima et al. 2013]. The Australian-Antarctic Basin (80 ^{o} - 150 ^{o}E) contains two types of AABW, defined by their sources: Ross Sea Bottom Water enters the basin from the east and mixes with Adélie Land Bottom Water that is formed locally in geographically restricted latent heat polynyas around the East Antarctic coastline [Rintoul 1998]. AABW in the Australian-Antarctic Basin has been observed to be freshening, possibly due to an increased supply of glacial meltwater from Antarctica [Aoki et al. 2005; Rintoul 2007].

The high rate of sea ice formation in latent heat polynyas and the associated brine rejection drives convection due to the formation of relatively dense water (e.g. High Salinity Shelf Water – HSSW). HSSW can sink below adjacent ice-shelves and drive basal melting of these ice-shelves leading to the creation of fresher Ice Shelf Water (ISW), which is defined as having a temperature below the surface freezing temperature [Lewis and Perkin 1986]. The mixture of HSSW, ISW and to some degree the overlying Circumpolar Deep Water (CDW) and Modified Circumpolar Deep Water (MCDW) can form Dense Shelf Water (DSW). DSW may be exported from the continental shelf, sinking into the deep ocean and mixing further with the MCDW, forming AABW. Changes in the volume of ISW and HSSW formed on the shelf can significantly alter subsequent formation rates of AABW at the continental shelf break [Hellmer 2004; Kusahara and Hasumi 2013].

During the period of this study (1992-2007), the Mertz Glacier Polynya (MGP), centred at about 67 °S and 145 °E, was the second largest polynya in area (23,300 km^2) along the East Antarctic coastline [Massom et al. 2001], and was a key source of DSW that ultimately becomes AABW [Rintoul 1998; Williams and Bindoff 2003; Williams et al. 2008]. From satellite remote sensing observations, the MGP estimated to produce an annual cumulative volume of sea ice of about 120±11 km^3 yr^{-1} [Tamura et al. 2008]. The factors that influence the ice production of the MGP are the steep ice-sheet topography inland from Commonwealth Bay and Buchanan Bay (Figure 2.1) that funnel strong and persistent katabatic winds into the area, the distribution of grounded icebergs and surrounding fast ice, and the position of the Mertz Glacier floating ice Tongue (MGT) and other icebergs (like the large grounded iceberg B9B) which form a barrier against westward moving sea-ice [Massom et al. 2001]. The MGT was 20 to 40 km wide and extended 150 km northward from the grounded ice-sheet, prior to its calving in 2010, which cut its length in half.

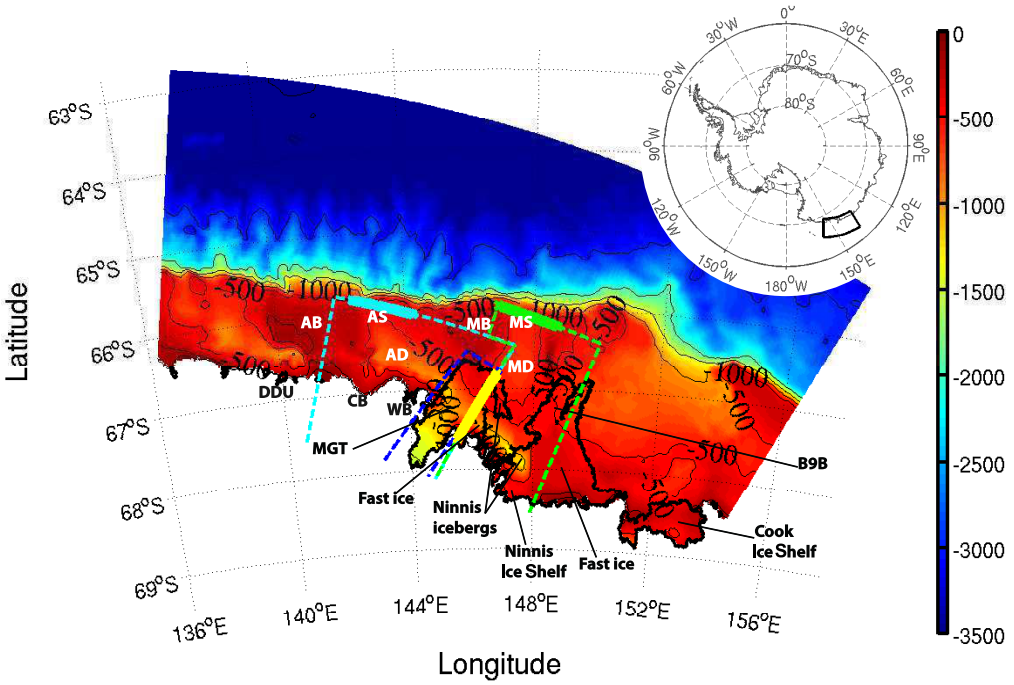

Figure 2.1: Bathymetry of the model and features of note around the Adélie and Mertz depressions. In the ocean: (AB: Adélie Bank; AD: Adélie Depression; AS: Adélie Sill; MB: Mertz Bank; MD: Mertz Depression; MS: Mertz Sill), with the ice draft (dark line) of the Mertz Glacier Tongue (MGT; 140 km long, 25 km width), the B9B (with a draft of ∼300 m) and of the fast ice (∼30 m thick for the fast ice south east of the MGT and ∼10 m for the fast ice south east of B9B). Along the continent: Watt Bay (WB), Commonwealth Bay (CB), and Dumont D'Urville base (DDU). Cyan, green and blue dashed lines indicate the boxes (Adélie, Mertz and MGT boxes), used for averaging model results. The eastern edge of the cyan box is partially obscured by the green box and the yellow line. Cyan and green bold lines show the Adélie and Mertz sill section respectively, and the yellow bold line along the MGT shows the cavity section.

Direct observations of the ocean in the vicinity of the MGT during winter are rare, due to the extreme conditions making access difficult. The first and the only wintertime experiment in the Adélie region occurred in July-August 1999 [Bindoff et al. 2001; Williams and Bindoff 2003; Williams et al. 2008]. This wintertime experiment and associated summer observations have shown that DSW accumulates in the Adélie depression, and the Adélie sill is one of the primary outflow region for dense water to escape from the depression to the abyssal ocean [Bindoff et al. 2000; Williams et al. 2008]. The annual mean export of DSW through the Adélie sill was estimated to be 0.1–0.5 Sv [Williams et al. 2008], subsequently revised

down to 0.073 ± 0.086 Sv using improved analysis methods [Meijers et al. prep]. DSW exported at the sill depth (425 m) is dense enough relative to the offshore water masses to mix down the continental slope and slope canyons to form AABW [Williams et al. 2008]. More recent observations taken along the slope and over the deep ocean suggest that the Mertz sill, to the east of the MGT, may also be a region of DSW export [Williams et al. 2010]. The region to the east of the MGT also has a deep depression, called the Mertz depression or Trough, a sill (600 m) and an active local polynya in the lee of B9B. Modelling results also support the hypothesis that the Mertz sill is a key region of DSW export from the Mertz depression to the continental slope [Kusahara et al. 2011a].

Earlier model studies such as Marsland et al. [2004], using the Mertz-HOPE (Hamburg Ocean Primitive Equation) model (as described by Marsland et al. [2007]) and Kusahara et al. [2011a] using the Center for Climate System Research Ocean Component (COCO) model [Hasumi 2006], have studied the Adélie/Mertz depressions area. Both are coupled sea-ice/ocean models and have a global domain with high horizontal resolution over the study area. Neither of these studies include ice shelf/ocean interaction processes the circulation underneath ice-shelves or the formation of ISW. Our study uses a high resolution (∼2.16-2.88 km) regional ocean model, based on the Regional Ocean Modeling System (ROMS) [Shchepetkin and McWilliams 2005] to study the interannual variability of DSW export from the Adélie and Mertz depressions region from 1992-2007. The model is unique in that it has been modified to include ice shelf/ocean interactions and frazil dynamics and thermodynamics, and includes the ocean cavity beneath the MGT and other ice-shelves, icebergs and fast ice in the region [following Galton-Fenzi 2009; 2010; Galton-Fenzi et al. 2012]. Marsland et al. [2004] have shown a strong interannual variability of DSW outflow from the Adélie depression linked to variability in atmospheric forcing. In this study, we investigate the link between the variability of the surface polynya forcing and the shelf water, and how it impacts the density and volume of exported DSW.

Section 2.2 describes the model setup and forcing, and details the analysis procedure. A similar approach to Marsland et al. [2004], using heat flux variability, is used in section 2.3 to define different polynya states. Using these polynya states, we examine relationships between the intensity of polynyas and dense water export, and the interactions with the ice shelf. In section 2.4 and 2.5 we discuss key findings relating to dense water export. These include the different pathways for DSW export and

the importance of including the cavity under the MGT, as well as the link between polynya activity and DSW export in comparison with previous model studies.

2.2 Methods

2.2.1 Model and forcing

The three-dimensional ice shelf/ocean cavity model used here is based on the Rutgers version of the Regional Ocean Modeling System (ROMS) [Shchepetkin and McWilliams 2005]. ROMS has a free surface and uses a terrain-following vertical s-coordinate system controlled by the applied surface pressure, which has been adapted to allow the coordinates to follow the ice shelf draft [Dinniman et al. 2003], and has been applied to other area of Antarctica [Dinniman et al. 2007; Mueller et al. 2012]. The version of the model we use here was initially developed for studies of the Amery Ice Shelf/Ocean system [Galton-Fenzi 2009; Galton-Fenzi et al. 2012] and used in circum-Antarctic modelling studies [Galton-Fenzi 2010]. In the region of our study, a version of this model has been used to simulate the circulation patterns and water mass properties in the vicinity of the Adélie and Mertz depressions [Hemery et al. 2011; Cottin et al. 2012]. It has also been compared directly with summertime ship observations and year long current meter moorings at the Adélie sill and found to accurately reproduce the seasonality and circulation within the depression [Meijers et al. prep].

The model setup used here is similar to the one described by Galton-Fenzi et al. [2012] and only the major features and differences from the previous model are described below. The model includes realistic tides and thermodynamic interactions with the ice shelf, including the addition of a frazil subroutine. The ice shelf/ocean interaction is described by three equations of state representing the conservation of heat, salt, and a linearized version of the freezing point of seawater (as a function of salinity and pressure) [e.g. Holland and Jenkins 1999], which are solved to simultaneously find the temperature and salinity in the boundary layer beneath the ice shelf and the melt rate at the ice shelf base. The model grid extends from 135.77 °E (west of the French base Dumont D'Urville) to east of George V land at 158.08 °E and covers the Adélie and Mertz depressions from the coast line up to the deep ocean at 62.72 °S (Figure 2.1). The horizontal grid has a resolution of about 2.16 km near the southern boundary and 2.88 km near the northern boundary. The

vertical grid uses 31 contour following σ levels, arranged to give higher resolution near the top and the bottom of the water column.

The bathymetry and ice shelf draft is based on RTopo-1 [Timmermann et al. 2010] and was modified to include local high-resolution bathymetry data from Beaman et al. [2011], which is based on multibeam swath sonar and singlebeam bathymetry data with about 250 m resolution. The iceberg positions present in the region, and the MGT ice draft was created using high resolution SPOT5 imagery, radar profiles from Legrésy et al. [2004] and more recent airborne radio echo sounding (ICECAP project from International Polar Year and Greenbaum et al. [2010]). The bathymetry beneath the MGT has been created to accommodate the grounding line position and its thickness [Legrésy et al. 2004; Mayet et al. 2013]. The ice draft of the MGT is shown in Figure 2.5, while the B9B icebergs has a draft of 300 m and Ninnis icebergs have a comparable thickness. Fast ice is an important factor to consider in the region because of its thickness and its multi-annual presence in some areas [Massom et al. 2009]. We include a climatology from Fraser et al. [2012], which produces two main areas of permanent fast ice near the MGT. These regions are southeast of the ice tongue and southeast of the B9B iceberg, where fast ice is continuously present with a relatively constant area (see Figure 2.1). Southeast of the MGT fast ice attached to the glacier tongue is relatively old (at least 25 years) and thick (from 10 to 55 m). This is about 10 times thicker than the mean thickness of pack ice in the region [Massom et al. 2010].

Following Galton-Fenzi et al. [2012], the model is forced with monthly data over the period from January 1992 to December 2007. Previous studies highlighted the importance of small scale features, such as grounded icebergs, many of which are only a few hundred meters in scale. These features are important for the formation of polynyas and lead to localised enhanced DSW production [Kusahara et al. 2010]. However, coastal polynya and icebergs are often poorly resolved or are not parameterised in models, and so no sea ice model is coupled to the ocean in the present study. Instead, heat and salt fluxes, based on ice concentration from a climatology derived model using Special Sensor Microwave Imager (SSM/I) observations from 1992 to 2007 [Tamura et al. 2008; 2011], are used to adequately resolve the fine-scale polynya in the region, as has been done for other similar studies as Dinniman et al. [2003; 2007]. During summer, the Tamura et al. [2008] data are supplemented with open-water heat and salt fluxes using monthly climatologies from NCEP-2 [Kanamitsu et al. 2002]. Surface winds are derived from the second version of CORE data

developed by Large and Yeager [2009] for global ocean-ice modelling [Griffies et al. 2009]. The surface kinematic wind stress, τ, is calculated in the i and j-direction from the wind velocity field, $\mathbf{u}$ as:

$$\tau_{i,j} = \rho_a c_a \mathbf{u}_{i,j} |\mathbf{u}_{i,j}|$$

where, ρ_a is the air density (1.3 kg m^{-3}) and c_a is the dimensionless air-sea friction coefficient (1.4×10^{-3}). Lateral boundary fields, including potential temperature, salinity and horizontal velocities are relaxed to monthly fields from ECCO2 over the period [Menemenlis et al. 2008; Wunsch et al. 2009]. The model was run for 48 years, including a spinup phase of 32 years to reach equilibrium using a repeating loop of synoptic forcing from between 1992 to 2007. The final 16 years are used in the analysis.

2.2.2 Analysis regions and experiments

To investigate the exchange between both shelf depressions and the export of DSW over the shelf break, our analysis is focused on three boxes around the Adélie and Mertz depressions and the MGT (Figure 2.1), and on three sections at the Mertz and Adélie sills and at the MGT cavity. These regions are chosen so as to facilitate comparisons with other studies [e.g. Marsland et al. 2004; Kusahara et al. 2011a; Meijers et al. prep]. The variables that are examined are potential temperature, salinity, horizontal velocities and the volume transport of the main water mass classes (defined below). The boxes chosen completely surround the MGT in order to investigate the circulation through the cavity and ISW formation. They also include both the Adélie and Mertz depressions and their corresponding polynya areas, where the formation of shelf water occurs, and finally include both sills, where the export of DSW from the depressions is thought to occur [Williams et al. 2010; Kusahara et al. 2011a].

Different types of water interact within our study area, coming from offshore or forming over the shelf (Table 2.1). Antarctic Surface Water (AASW) is relatively warm and is the least dense water mass in the region, appearing at the surface. Below the surface offshore there is warm and saline CDW, and the deepest water mass off the shelf break is AABW. CDW moves southward and becomes Modified CDW (MCDW) through mixing with AASW and water over the shelf, before crossing the shelf break and entering the shelf region in the mid-water column where it

can interact with HSSW and ISW created during sea ice formation and ice tongue melting respectively. Low Salinity Shelf Water (LSSW), corresponds to a water mass similar to the HSSW in potential temperature but with a salinity less than 34.5 psu. We define DSW here as any water having a potential density greater than 1027.88 kg m^{-3}. This potential density has been used in previous studies as being the minimum potential density capable of sinking off the shelf and reaching abyssal depths, eventually contributing to the formation of AABW [Bindoff et al. 2001; Williams et al. 2008; Kusahara et al. 2010].

To highlight the importance of considering ocean/ice shelf thermodynamics in modelling studies of shelf processed and dense water export, two experiments are performed for this paper:
1 – "Reference simulation": the reference simulation uses the best version of the model described above, including ice shelf/ocean thermodynamics.
2 – "Without ice shelf thermodynamics": reference simulation, but without ice shelf basal melting/freezing, so no ISW will be generated.

Table 2.1: Water masses defined by potential temperature (θ), salinity (S) and potential density (ρ). fp is the in-situ freezing temperature of sea water at 50 dbar.

Water type	θ (°C)	S(psu)	ρ (kg m^{-3} -1000)
$AASW$	-1.75 $\leq \theta \leq$ 2	-	$\rho \leq$ 27.75
$MCDW$	-1.75 $\leq \theta <$ 1	-	27.75 $< \rho <$ 27.88
$HSSW$	fp $< \theta <$ -1.75	S $>$ 34.5	-
$LSSW$	fp $< \theta <$ -1.75	S $\leq$ 34.5	-
ISW	$\theta \leq$fp	-	-
DSW	-	-	$\rho \geq$ 27.88

2.3 Results

2.3.1 Polynya activity

The 16 year time series of heat fluxes from Tamura et al. [2008; 2011] shows an interannual variability in polynya activity (intensity) in the region (Figure 2.2). This figure shows the cumulative heat flux anomalies and the average wintertime heat flux anomalies for an area including both the Adélie and Mertz depressions (black line). It also shows those anomalies for smaller areas, one centred on the Mertz

Glacier Polynya (MGP) over the Adélie depression (dashed line) and the other on the polynya in the lee of B9B iceberg over the Mertz depression (dotted line). The polynya activity is slightly different between the MGP and the region over the B9B polynya, but not dramatically so. For simplicity, we define the state of polynya activity as changes over the combined area of the depressions. The cumulative heat flux anomalies from monthly means over the Adélie and Mertz depressions (Figure 2.2a), shows a sudden change in polynya activity occurring in 2002. A positive cumulative flux trend indicates that the flux of heat from the ocean to the atmosphere is less than the normal trend over the whole period, and therefore indicates a decrease in polynya activity. A negative trend in polynya activity indicates intensified heat loss and increased polynya strength. In Figure 2.2a, interannual variability is observed with a net increased cumulative flux from 1999 to 2001 inclusive (about +550 MJ m^{-2}) with a sudden change in 2002 and a strong decrease of the cumulative flux until 2004 (about -600 MJ m^{-2}). From 1992 to 1996, the cumulative heat flux anomalies are relatively constant before increasing from 1997 to 1999 (+300 MJ m^{-2}), although at a weaker rate than from 1999 to 2001.

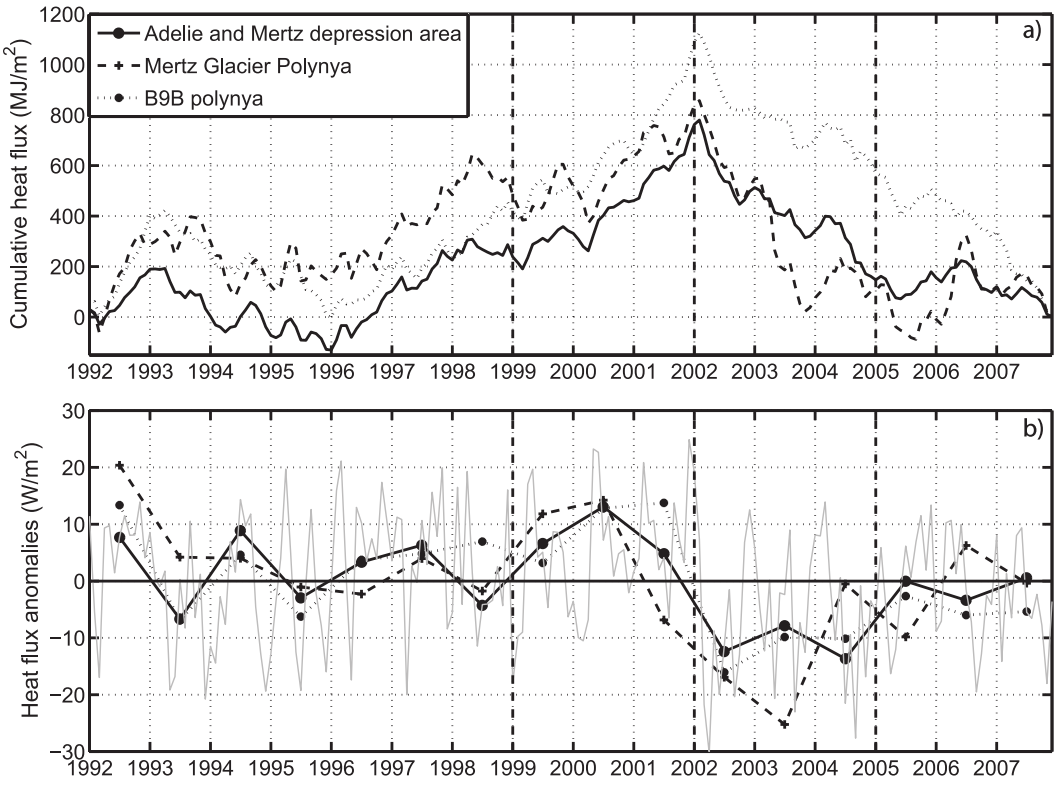

Figure 2.2: a) Cumulative heat flux anomalies for the shelf area including both the Adélie and Mertz depressions (black line), for a small area over the Adélie depression (Mertz Glacier Polynya, dashed line) and a small area over the Mertz depression (B9B polynya, dotted line). Vertical dashed lines show the different states in polynya activity described in the text. b) Heat flux anomalies for monthly means from Tamura et al. [2011] (fine grey line) and wintertime averages from May to September inclusive over the shelf area including both Adélie and Mertz depressions (black line with dots), the Adélie depression (Mertz Glacier Polynya, dashed line) and the Mertz depression (B9B polynya, dotted line). Negative anomalies indicate increased polynya strength and Dense Shelf Water formation.

The average heat flux anomalies (Figure 2.2b) for the wintertime average (from May to September inclusive), show the same pattern in terms of interannual variability, with the same two key periods of polynya activity. The period from 1999 to 2001 inclusive has a wintertime positive heat flux anomaly of approximately 8±4 W m^{-2}, corresponding to a 'weak polynya state'. The period from 2002 to 2004 inclusive has a wintertime negative heat flux anomaly of approximately -11±3 W m^{-2}, corresponding to a 'strong polynya state'. It is more difficult to define persistent strong or weak states for the other years because negative heat flux anomalies alternate with positive anomalies each year, corresponding to a constant cumulative heat flux. We therefore call the period from 1992 to 1998 the 'mean polynya state'. Marsland

et al. [2004] defined similar periods in polynya activity for the years in which the studies overlap (1992-2001). They defined a strong polynya state from 1993 to 1999, corresponding to the 'mean' polynya state in our study, and weak polynya years (1999 and 2000) corresponding with our weak polynya state. As our study is longer, we define another period of 'strong' polynya activity from 2002 to 2005.

2.3.2 Transport from the Adélie and Mertz depressions

The export by time for each density class between 1027.65 kg m^{-3} and 1028.00 kg m^{-3} is shown in the colored panels of Figure 2.3. The export is binned in density increments of 0.01 kg m^{-3} for the Adélie and Mertz boxes and both sills. This export is calculated as monthly averages over the entire period (from 1992 to 2007). The critical DSW density limit (1027.88 kg m^{-3}) is represented by the horizontal dashed line. Figure 2.3 clearly shows interannual variability in the export of DSW for both depressions and sills, but also seasonal variability. The minimum density for exported water is denser at the end of each winter and slightly lighter during summer, and does not always exceed the critical value. Over the 16 study years, three distinct periods of DSW export can be defined, as indicated by the vertical dashed lines. The first period is from 1992 to 1998, where the DSW export is strong for the Adélie box, and the two sills, associated with an import of the densest DSW into the Mertz box. 1999 is a transition year with lighter water exported, too light to be considered DSW but dense enough to be still exported from the Adélie box. This transition period is followed by a second period from 2000 to 2002, where there is almost no export of DSW from any of the boxes and sections. The last period is from 2003 to 2005 where there is an increase of DSW export mainly seen to flow out of the Adélie box and circulate through the cavity to the Mertz box. These periods lag the previously defined periods of polynya activity (shown by the arrows on the figure) by about a year.

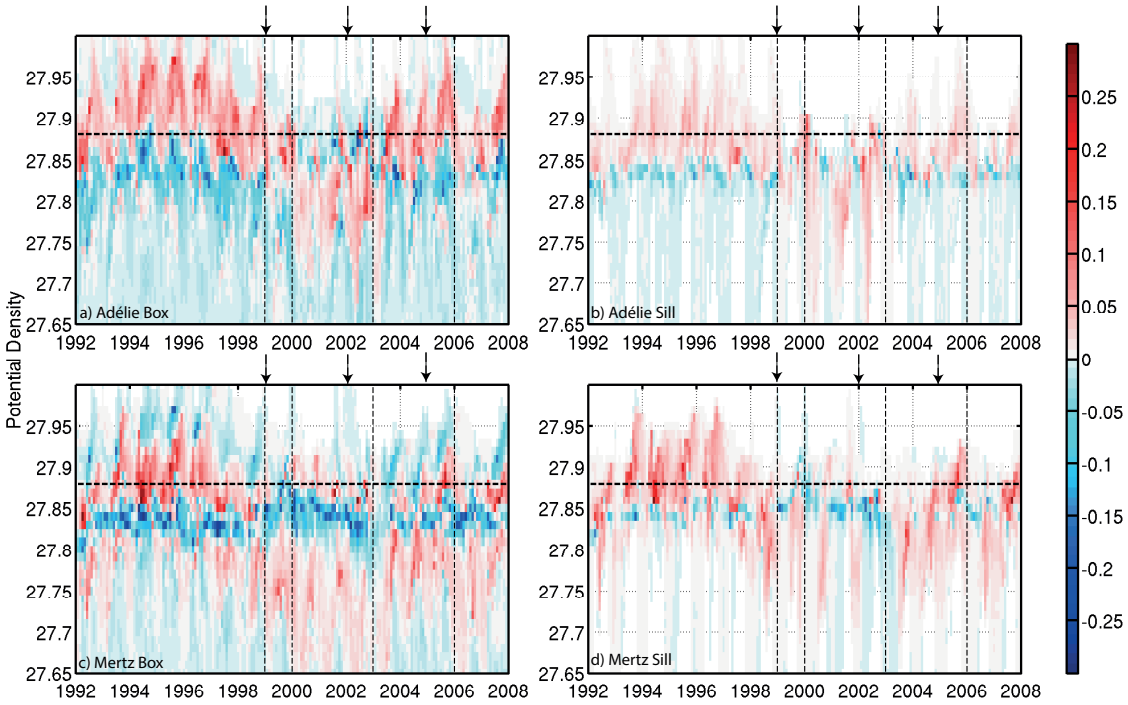

Figure 2.3: Transport (in Sv) by potential density class (in kg m^{-3} -1000) for each box and sill. Positives values (red) correspond to an export; negative values (blue) correspond to an import. Horizontal dashed line is the critical density 1027.88 kg m^{-3}. Vertical dashed lines show the limits of different states of DSW export, as discussed in the text. The arrows at the top of each panel show the transition between polynya activity states.

Different water masses can share the same density characteristics, so it is therefore useful to consider the transport results presented in Figure 2.3 together with potential temperature and salinity characteristics to determine the transport pathways of each of the main water masses. Figure 2.4 shows the net transport across both boxes and sills binned by potential temperature and salinity, averaged over the periods 1992-1998, 2000-2002 and 2003-2005. This projection allows us to see the different water masses that enter and exit each depression. The different water masses defined in Table 2.1 are labelled in Figure 2.4a, and we focus on the variability of the four main water masses: MCDW, HSSW, ISW and DSW. ISW is defined here to be colder than the freezing temperature of sea water at 50 dbar. Using a depth below the surface is a necessary condition so that very shallow ISW produced by melting of thick fast ice east of the MGT (at about 35 m) is excluded. The averaged transport for each water mass (in 10^3 m^3 s^{-1} or milli-Sverdrups) and period for the Adélie and Mertz boxes and sills, and also for the cavity are summarized in Table 2.2 a, b and c. Averages are also calculated for each case during the annual 'peak export' period,

which is defined as July to November, following Marsland et al. [2004] and which also corresponds to the peak dense water formation from observations [Williams et al. 2008].

The density transport for both the Adélie and Mertz depressions differs between each period. However, in all three periods there is an import of relatively warm MCDW (between 0 °C and 0.5 °C, see Figure 2.4a, b, c, g , h and i) with a density between 1027.80 kg m^{-3} and 1027.85 kg m^{-3}. For the Adélie box, an export of water denser than 1027.85 kg m^{-3} (dense enough to exist below the imported MCDW) is seen for both the first period (1992-1998) and the last period (2003-2005). This contributes to an export of DSW of 378 mSv for the first period and of 273 mSv for the last (Table 2.2 a). During the first period, 29% of the DSW exported from the Adélie depression flows out through the Adélie sill (110 mSv), while only 19% goes through the sill during the last period (51 mSv). During the second period the export is less dense, more spread in terms of density and salinity, and is only marginally denser than the imported water, so there is very little net DSW exported through the sill ($<$ 30 mSv).

An export of very salty and dense HSSW is observed from the Adélie box with a transport of 212 mSv and 159 mSv for each period respectively. This export has the same characteristics as the very dense water imported into the Mertz box (Figure 2.4g, h and i). The circulation through the cavity section makes up a large proportion of the total DSW transport: 43% of the exported DSW formed in the Adélie depression is going through the cavity (165 mSv) during the first period and 46% (127 mSv) during the last period. This implies that 28% of DSW formed in the Adélie depression during the first period and 35% during the last period exits the box through pathways other than beneath the cavity or through the sill. These other pathways are discussed further in section 2.4.2.

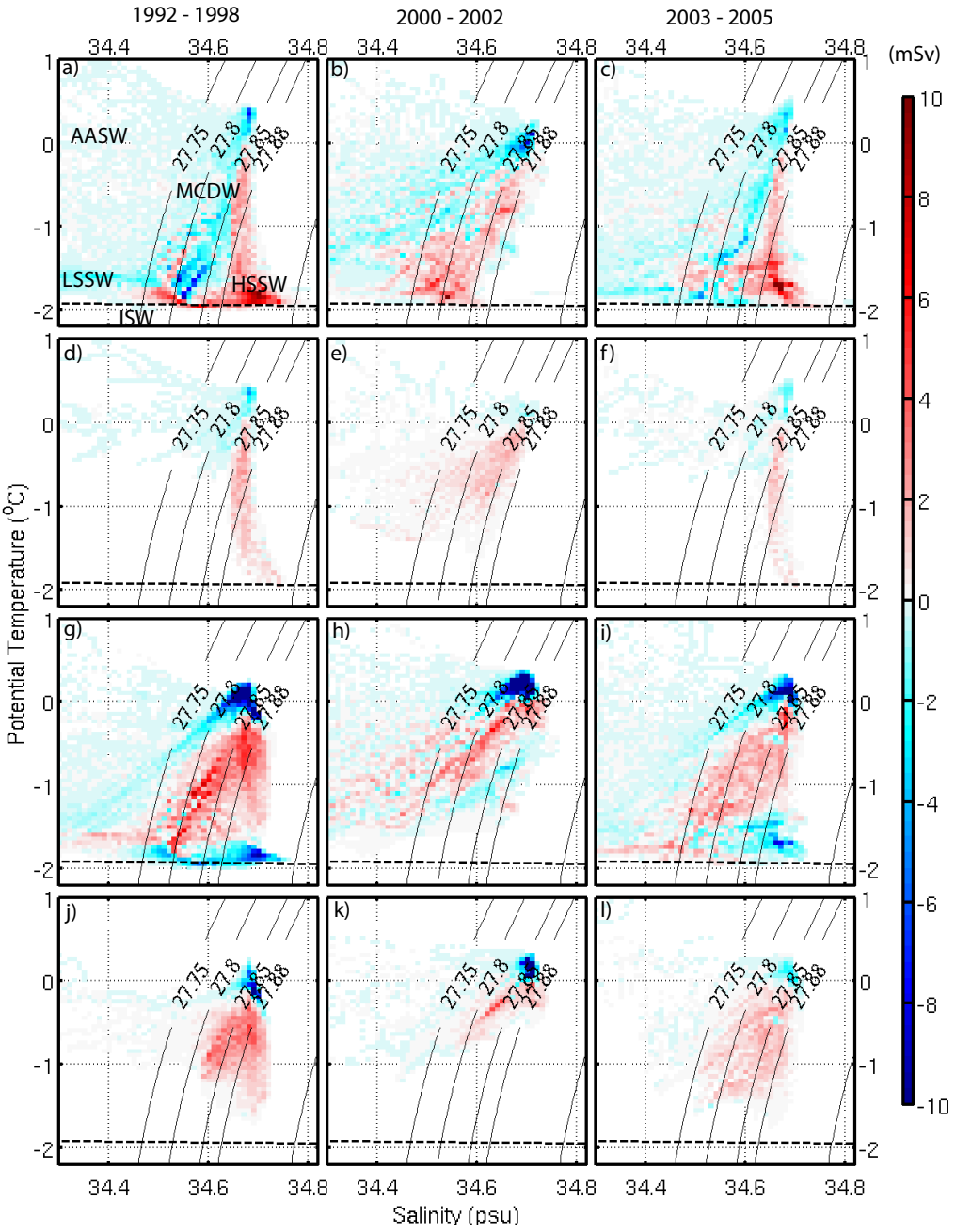

Figure 2.4: Potential Temperature-Salinity transport diagrams for the Adélie box (a, b, c) and sill (d, e, f), and Mertz box (g, h, i) and sill (j, k, l), split by period. Positive values (red) correspond to an export, and negative values (blue) correspond to an import (in milli Sv). Water masses are shown on the top-left panel. Some potential density contours are shown on each diagram, with a dashed line corresponding to the freezing temperature of sea water at 50 dbar, used to define ISW in this study.

Table 2.2: Net export for each period from the Adélie box and sill (a) and for the Mertz box and sill (b) for the different water masses (milli Sv) from Table 2.1. Positive values correspond to an export and negative values to an import. Values in squared brackets are averaged for the peak DSW export period from July to November inclusive.

a)

	Mean (1992-1998)	Weak (2000-2002)	Strong (2003-2005)
Adélie box			
AASW	-97 [-91]	-197 [-199]	-75 [-55]
MCDW	-310 [-394]	94 [63]	-154 [-296]
HSSW	212 [281]	108 [140]	159 [220]
LSSW	-12 [-15]	37 [40]	-43 [-58]
ISW	61 [91]	9 [12]	31 [47]
DSW	378 [490]	-15 [-15]	273 [440]
Adélie sill			
MCDW	2 [-4]	188 [76]	7 [-46]
HSSW	16 [23]	10 [14]	11 [18]
ISW	5 [9]	1 [0]	4 [7]
DSW	110 [138]	30 [20]	51 [74]

b)

	Mean (1992-1998)	Weak (2000-2002)	Strong (2003-2005)
Mertz box			
AASW	-66 [-62]	139 [99]	-60 [-84]
MCDW	-23 [-24]	-253 [-143]	84 [131]
HSSW	-127 [-182]	7 [0]	-70 [-94]
LSSW	-16 [-29]	-10 [-31]	8 [2]
ISW	-40 [-55]	1 [0]	-11 [-19]
DSW	120 [116]	48 [16]	-35 [-62]
Mertz sill			
MCDW	162 [194]	-60 [55]	225 [312]
HSSW	11 [13]	0 [0]	17 [28]
ISW	1 [1]	0 [0]	2 [3]
DSW	207 [286]	23 [44]	69 [114]

c)

	Mean (1992-1998)	Weak (2000-2002)	Strong (2003-2005)
Cavity			
MCDW	-26 [-42]	41 [150]	45 [39]
HSSW	151 [224]	-5 [3]	119 [181]
ISW	40 [56]	-1 [0]	18 [29]
DSW	165 [260]	22 [58]	127 [214]

DSW that circulates beneath the MGT from the Adélie depression appears as an import into the Mertz box and is the sole pathway of DSW into the Mertz box through lateral boundaries. The 120 mSv exported out of the Mertz box are formed

in the Mertz depression, primarily from the polynya in the lee of B9B, which is two third less than the DSW produced in the Adélie depression. The distribution of the water exported through the Mertz sill, in terms of density, shows a small import of MCDW (Figure 2.4j, k and l), coupled with an export of cooler MCDW. Also, 207 mSv of DSW is exported through the sill during the first period significantly more than the net depression export. During the last period 69 mSv of DSW goes out through the Mertz sill, while the global DSW transport over the entire Mertz box shows an import of 35 mSv. This highlights the importance of the Adélie depression as the primary source of DSW and of the circulation beneath the MGT. During the second period, associated with weak polynya forcing, there is only a weak export of DSW (< 50 mSv) from the whole Mertz box.

2.3.3 Transport and melting in the Mertz Glacier Tongue cavity

In this section we examine the transport through the cavity. DSW formed in the Adélie depression flows into the MGT cavity on its western side, interacting with the ice shelf and mixing with ISW, leading to an export of slightly fresher and lighter water into the Mertz depression from the eastern side of the MGT. The difference between the second (weak) and the first (mean) periods in θ and S along the section defined by the MGT box are shown in Figure 2.5a and 2.5b. The third period (strong) is similar to the first, so anomalies from this period are not shown. The second period is mostly fresher and warmer everywhere along the section, except at about 400 m along the northern part of the MGT where a warm and salty anomaly occurs (of about +1 °C and +0.04 psu). The perpendicular velocity across the MGT transects over both periods (Figure 2.5c and 2.5d) shows a corresponding change in the circulation and magnitude along the northern part of the MGT at about 400 m. Import into the cavity at depth increases on the western boundary of the MGT, and a current can also be seen crossing the northeasterly tip of the MGT, heading in a southeasterly direction between 400-600 m. This is indicative of an import of MCDW under the northern part of the MGT during the period of weak polynya activity.

The change in circulation impacts MGT melting (Figure 2.6). The area-averaged melt rate, integrated over the whole MGT for the entire period, is 1.9±1.4 m yr^{-1} (11.4±8.4 Gt yr^{-1}). For ice deeper than 900 m, melt rates are 4.5±2.3 m yr^{-1}

(3.0±1.5 Gt yr^{-1}, not shown). The standard deviations of these values indicate the large temporal variability due to tidal, seasonal and interannual forcing on the tongue. Observational estimates of melt rates, from flux gate calculations close to the grounding line vary from 11 m yr^{-1} [Berthier et al. 2003] to 18 m yr^{-1} [Rignot 2002]. Given that 14-18 Gt yr^{-1} of ice is estimated to flow into the MGT from the grounded ice sheet [Wendler et al. 1996; Frezzotti et al. 1998], our estimates of basal melting indicate that about 63 to 81% of the total ice flowing into the MGT is melting from the underside, underlining how important it is to understand the ice-ocean interactions.

Figure 2.6 shows that the period of greatest net melt (3.8±1.5 m yr^{-1}) occurs during the second (weak) period of polynya activity (2000 to 2002 inclusive) with the maximum melt rate ($<$ 8.5 m yr^{-1}) occurring during the summer of 2002/2003. Melting starts to decrease in 2003, corresponding to the beginning of the third (strong) period, when the export of dense water increases again. The area-averaged melt rate for the first and the third periods is 1.2±0.4 m yr^{-1}. Despite the enhanced melting only small amounts of ISW, defined here as having a potential temperature below the freezing temperature at 50 dbar, is exported from beneath the MGT during the second period. This suggests that the additional glacial meltwater is warmer than our defined freezing temperature, and so is not classified as ISW and therefore likely to have been produced by warm MCDW during melting.

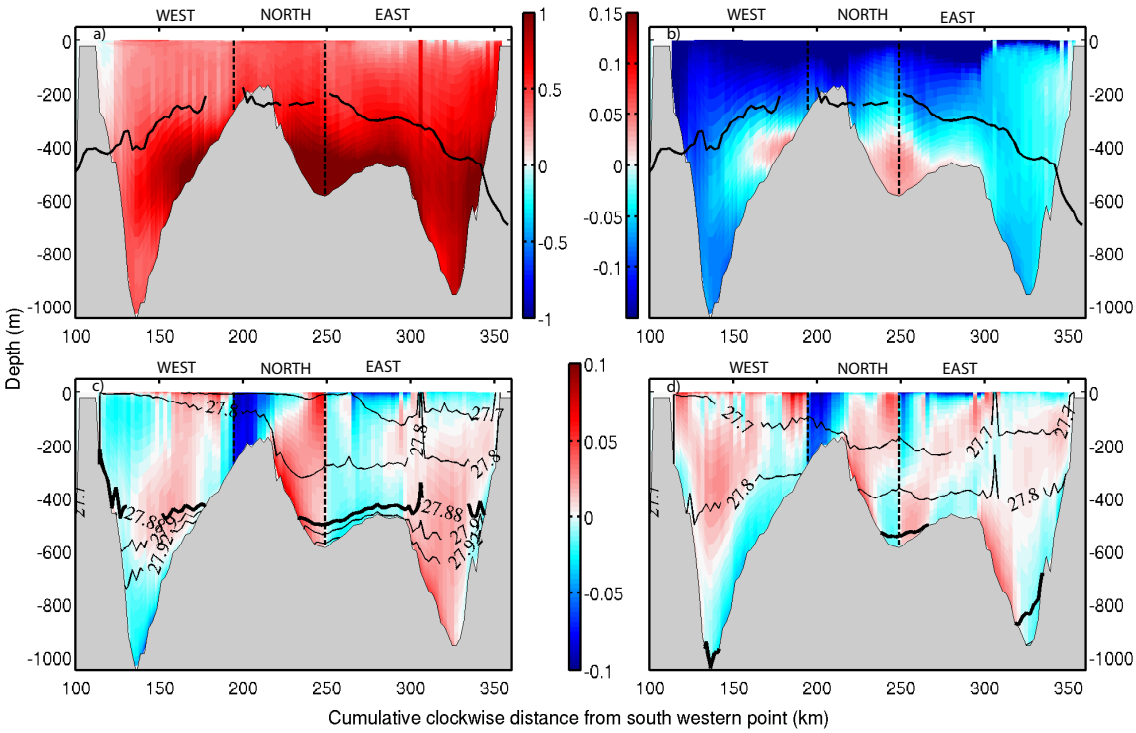

Figure 2.5: Differences in potential temperature a) and salinity b) for the MGT box between the second (2000-2002) minus the first (1992-1998) periods. The black line on a) and b) shows the MGT ice draft for each edge of the ice tongue. c) and d) show the perpendicular velocity through the MGT box sections for the first and second period respectively (m s^{-1}), with potential density contours. Positive values are out of the MGT box.

2.3.4 Sensitivity of Dense Shelf Water export to glacial meltwater

A recent study by Kusahara and Hasumi [2013] has shown the importance of including basal melting in modelling studies such as that one. To test the effect of having ice shelf thermodynamics in our model, a comparison between both the reference simulation and the simulation without ocean/ice shelf thermodynamics are presented in this section. Ocean/ice shelf thermodynamics in the model allows the formation of fresh and supercooled water due to ice shelf melting, which can mix with the surrounding dense water. Hellmer [2004] has shown that a decrease in ice shelf area with an associated reduction of basal melting significantly changes shelf water characteristics and enhances the formation of DSW.

Figure 2.7 shows monthly climatologies of both simulations along both sills and along the cavity section on the eastern edge of the MGT. The simulation without

ocean/ice shelf thermodynamics shows denser water in the cavity (∼0.06 kg m^{-3} denser) and at both sills (∼0.02 kg m^{-3} denser). Associated with this increased in density, a greater transport of DSW through these sections is also seen. Around 0.05 Sv more DSW flows from the Adélie to Mertz depression, but over 0.30 Sv extra is exported from the Mertz sill. Table 2.3 summarises the averaged transport through the studied sections.

The simulation without ocean/ice shelf thermodynamic overestimates DSW export by different magnitudes depending on the region. Compared to the reference simulation, DSW export is 100% greater for the Adélie sill and 50% larger for the entire Adélie box. However, for the Mertz box, omitting ocean/ice shelf thermodynamics induces an overestimation of DSW export of more than 500%. This very large increase in DSW export through the whole Mertz box is explained by the presence of more ice shelves in the Mertz box area (MGT, B9B, Ninnis icebergs and fast ice). This relatively larger ice area in the Mertz depression induces greater volume of fresh and supercooled water, which mixes with the dense water imported from the Adélie depression and produced locally, and results in lighter and cooler DSW.

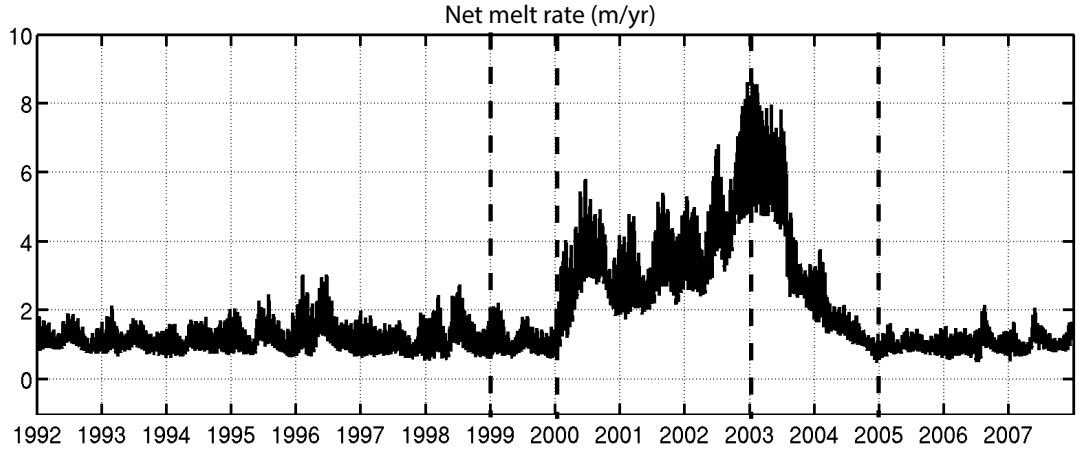

Figure 2.6: Net melt rate from the Mertz Glacier Tongue (in m yr^{-1}), combining the mass lost from the ice tongue and the accumulation of frazil ice. Vertical dashed lines show the same polynya transitions as in Figure 2.3.

2.4 Discussion

2.4.1 Links between polynya activity, ice shelf melting and DSW export

Our results show a delay between the timing of the strength of polynya activity and the corresponding change in dense water export, not seen in previous studies. The weaker export, from 2000 to 2002, is delayed by about a year after the weakest polynya activity occurs during 1999 to 2001. The strongest polynya state (2002-2004) induces an increased DSW export in volume and density steadily over all three years from 2003 to 2005. However, this export remains on average less dense than during the first period (1992-1998). This difference in density export between the two periods suggests that after a period of weak polynya activity leading to a decrease of DSW export, three or more years of strong polynya activity are needed to precondition the density of shelf water to support the export of very dense water again. It is interesting to note that during the 'mean' polynya state, there is a stronger export of the densest DSW than during the 'strong' polynya state. This is likely due to the spinup period of the model. For the 32-spinup years prior to 1992, the model uses the same forcing (1992-2007), so the water masses at 1992 for the 'mean' polynya state have been preconditioned by the last years of the atmospheric forcing, driving stronger net export.

The temporal interannual variability in the basal melt rate of the MGT follows the same pattern as the DSW export. Whilst the MGT is melting at a rapid rate between 2000 and 2002 (3.8 ± 1.5 m yr^{-1}), only small amounts of ISW are seen passing through the analysis boxes used in this study. During this time the glacial meltwater that is produced must mix with the warmer ambient water and form a watermass that contains glacial meltwater which is warmer than our definition of ISW.

During the weak polynya state, MCDW penetrates further on-shelf, although the actual volume entering the Adélie box does not change significantly from the strong or mean states (2.3 Sv for 1992-1998, 2.1 Sv for 2000-2002, and 2.0 Sv for 2003-2005). The mechanism driving MCDW onto the shelf may be due to a combination of factors. In some regions, the primary mechanism causing MCDW to move on-shelf is changes in winds [e.g. Steig et al. 2012; Dinniman et al. 2012]. Alternatively, St-Laurent et al. [2013] demonstrates that a warm slope front current may be also guided on-shelf via troughs in the slope bathymetry.

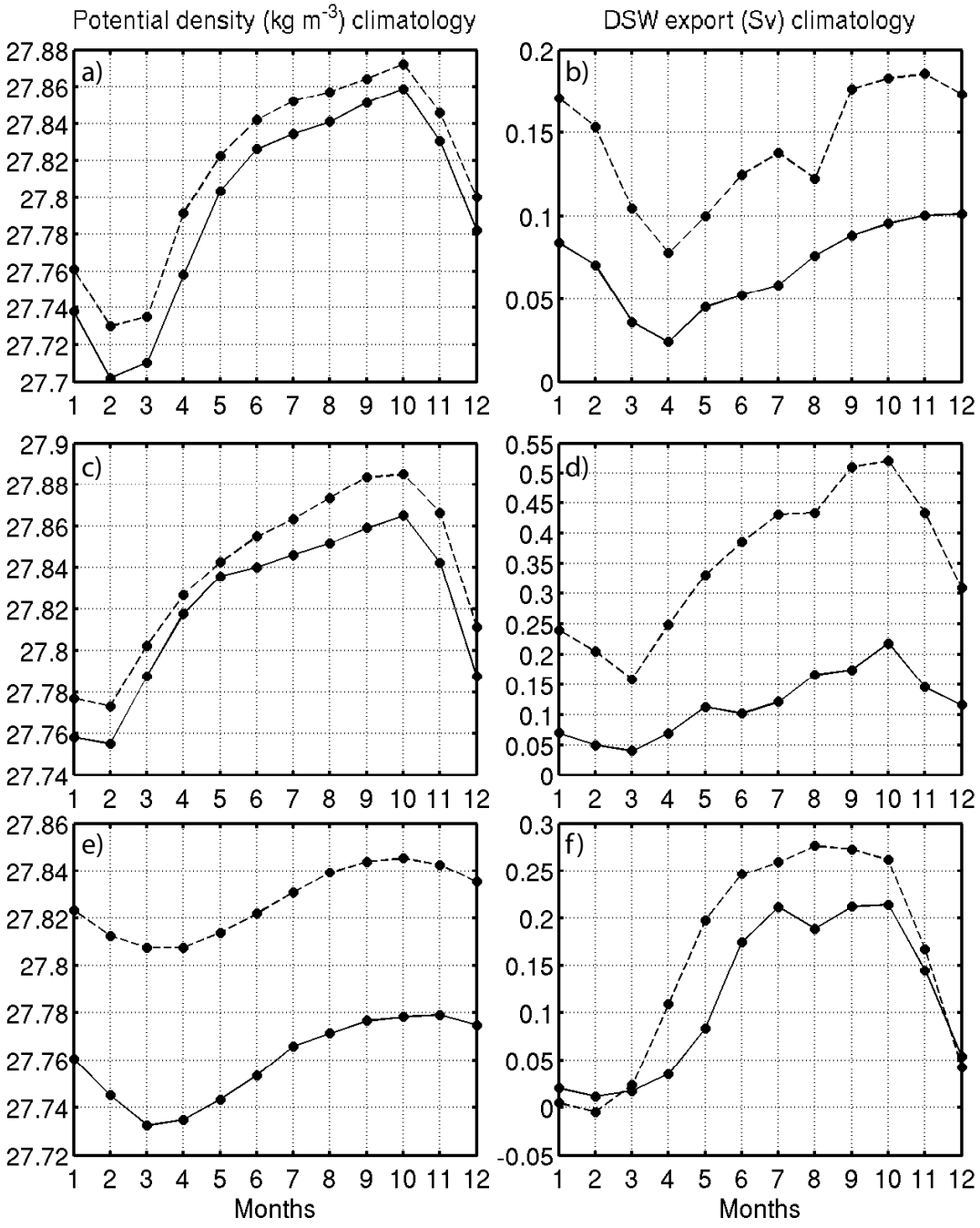

Figure 2.7: Monthly climatologies averaged over the entire period (1992-2007) for the potential density (left panels) and DSW transport (right panels) for the reference simulation (black line) and the simulation without ocean/ice shelf thermodynamics (dashed line) for the Adélie sill (a and b), the Mertz sill (c and d) and the cavity section (e and f).

A detailed dynamical examination of the factors driving MCDW circulation onto the

shelf is beyond the scope of the present study, although qualitatively the Mertz Bank does appear to be important in guiding intrusions towards the MGT (Figure 2.8). What we find, however, is that MCDW import is not correlated with changes in DSW export nor with changes in surface wind stress (not shown). This supports the findings of Marsland et al. [2004] who found that polynya buoyancy flux was the primary factor controlling DSW export and winds had little correlation with the DSW production. Of course polynya activity is not independent from the winds, ocean temperature or circulation and there exist complex feedbacks between these factors. However, polynya activity, as measured by heat flux, is representative of an integration of these atmospheric and oceanic terms for the purpose of this study, and we find that there exists a useful correlation with the strength of these polynyas driving DSW export.

The lack of correlation between polynya activity and MCDW import does not imply that inflow from off the shelf is unimportant to the circulation. During weak polynya states the intruding MCDW is not cooled as dramatically and may interact with the MGT and modify the ice shelf/ocean driven circulation [Klinck and Dinniman 2010] by intensifying the ice pump mechanism through cavity enhanced basal melting [Lewis and Perkin 1986]. MCDW driven basal melting makes the water fresher and more buoyant which causes it to rise along the bottom of the ice shelf. This buoyancy driven flow has the effect of pulling deeper water to the base of the ice shelf. This induces more ice shelf melting which may further decrease the formation and density of DSW in the region. This positive feedback between intruding warm MCDW and increased freshening is discussed further in the following section.

2.4.2 Regional circulation

The model allows the detailed examination of DSW export pathways from the region, and we find several more than have been previously assumed in observational studies. The time-averaged potential temperature and density at the model bottom layer, overlaid with the current direction during each period is shown in Figure 2.8. This figure shows that dense water spreads between both depressions through the MGT cavity and over the shelf break. Significant volumes of DSW are being exported from the Adélie box via the cavity under the MGT (120 mSv averaged over the entire period) as well as along the coast to the west (from the western edge of the Adélie box, 18 mSv averaged over the entire period). The heat flux forcing

[Tamura et al. 2011] includes many small but active polynyas along the coast to the west of the MGT, such as in Commonwealth Bay. The model produces HSSW from these regions during winter and transports some DSW westwards as part of the coastal current. However, observations do not find any circulation of DSW along the coast, likely because of their summertime bias. In the model during summer there is no HSSW production and DSW present in deep troughs and depressions does not easily escape the shelf region, except at the Adélie sill, as in observations [Williams et al. 2008]. Future wintertime observations should observe these water masses predicted by the model to establish the importance of export westwards via the coastal current and outflows of the western edge of the basin.

The off-shelf export is simulated to occur through both Adélie and Mertz sills, and is also identified through another region located to the east of the Mertz sill (see black circles on Figure 2.8a and b), which export about 32 mSv of DSW averaged over the entire period. A significant part of the export going through the sills is missing in our current sill section locations. About 51 mSv of DSW, averaged over the entire period, is going throughout the western corner of the Adélie box and about 34 mSv throughout the western corner of the Mertz box directly west of the Mertz sill. This highlights the limitations of observational studies that only capture narrow regions of transport.

The net export of DSW from the Mertz depression is greater at the sill than over the entire depression (Table 2.2 b) due to the import from the Adélie depression via the cavity beneath the MGT. However, the DSW exported through the Mertz sill (with potential temperature between -1.5 and -0.5 ^{o}C and a salinity below 34.5 psu) has different properties than the incoming DSW flow from the Adélie depression (colder than -1.5 ^{o}C and sometimes saltier than 34.5 psu). This suggests that mixing occurs in the Mertz depression between DSW coming from the Adélie depression, the DSW or HSSW formed locally due to the polynya in the lee of B9B iceberg, ISW and overlying MCDW to produce relatively less dense DSW.

The flow of DSW from the Adélie to the Mertz depression is strongly controlled by the activity of the MGT polynya. Figure 2.8 and Table 2.2 show clearly that during the first period there is significant formation of DSW, occurring mainly in the Adélie depression. The DSW created in the Adélie depression flows both into the cavity beneath the MGT and across the Adélie sill towards the abyssal ocean. In contrast, the second (weak) period has warmer bottom water, particularly over the Mertz

depression and the northern edge of the MGT, and the water is significantly fresher on the Adélie and Mertz banks. Not enough DSW of sufficient volume and density is formed in the Adélie depression to enable the circulation to escape the shelf at the Adélie sill. Some DSW continues to circulate through the cavity and into the Mertz depression and through the sill but at much reduced rate. DSW starts to form again during winter 2003, mainly in the Adélie depression, which then spreads over the shelf to again escape through the Adélie sill at lower rate than during the first period, indicating a phase lag between the initial formation and eventual export of DSW. More than a year of strong polynya state is needed to form a sufficient volume and density of DSW to recover from the weak forcing period and to flow into the deep ocean.

During the second period a reduced volume of ISW escapes the region, when we may have expected to see more due to the increased melt rates during this period. The extra melting is produced by enhanced MCDW penetration into the cavity. The warmer water mixes with the meltwater, resulting in a watermass warmer than the definition of ISW. Our results suggest that the commonly used definition of ISW that we have adopted for this study is inadequate for quantifying the amount of glacially sourced meltwater exported from the shelf.

The additional freshwater produced by the MCDW intrusion and glacial melting may provide one possible explanation for the lag between enhanced polynya strength and the recovery of DSW export following a period of weak polynya activity. Marsland et al. [2004] showed that the volume averaged salinity within the Adélie Depression prior to the onset of winter polynya activity was an important 'preconditioner' for DSW production and more saline pre-existing watermasses led to stronger exports of DSW and vice versa. The enhanced melting of the MGT during weak polynya states may lead to such preconditioning of the water column, from which DSW export subsequently takes several years to recover. These dynamics are beyond the present study, however, and further examination is required to establish the impact of the enhanced buoyancy during weak polynya years.

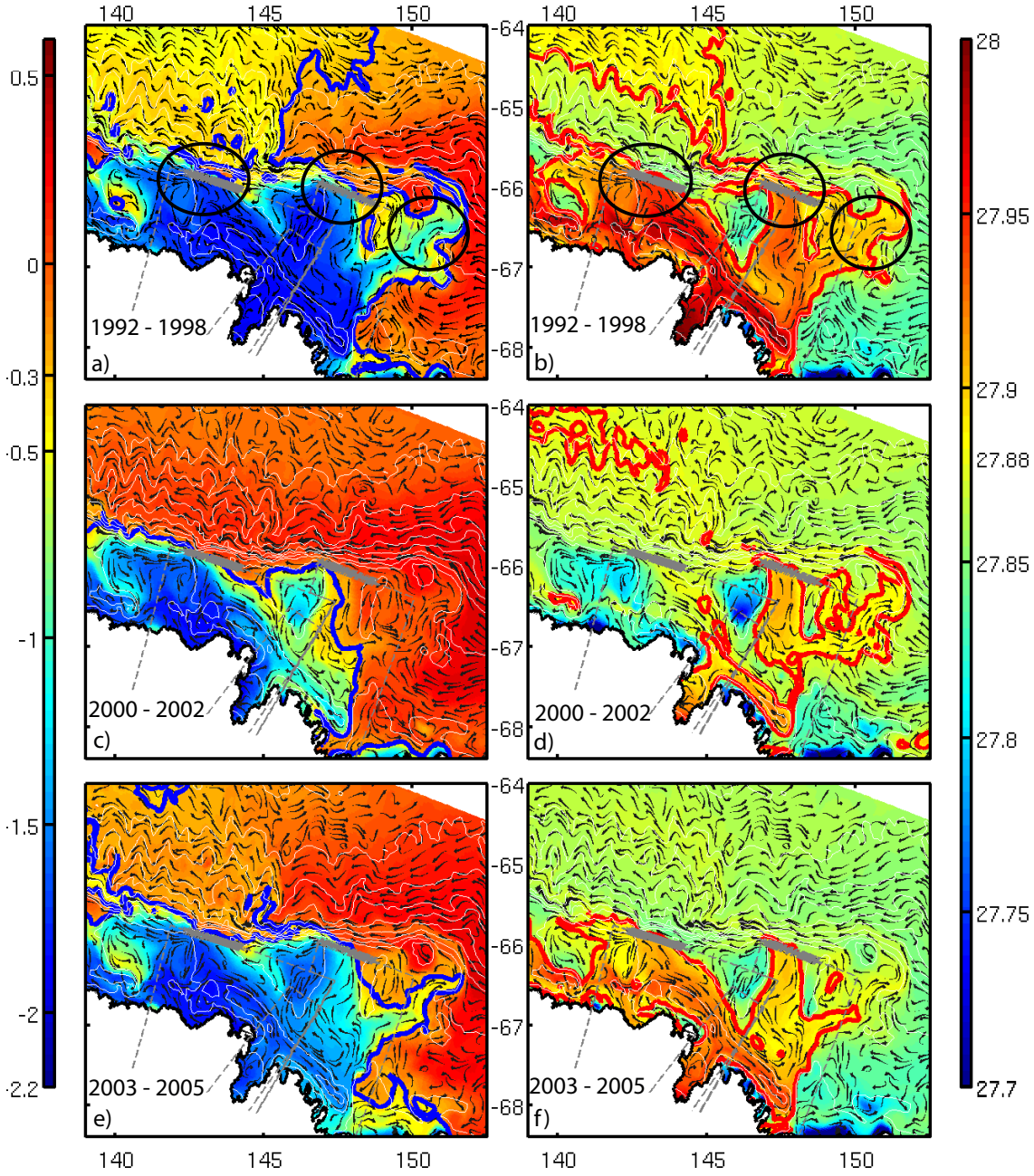

Figure 2.8: Potential temperature (left panels) and density (right panels), overlaid with velocity directions (arrows) averaged for each period at the bottom model layer. The velocity field is deduced from streamlines, but is indicative of direction only. The blue line on the potential temperature panels shows the -0.3 °C isotherm, and the red line on the potential density panels is the critical limit for DSW export and AABW formation (1027.88 kg m^{-3}). Dashed lines show box boundaries, black circles show the three main areas of export, and white lines depth contours.

2.4.3 Comparison with other studies

Two other modelling studies, [Marsland et al. 2004; Kusahara et al. 2011a], have examined this area using global domain ocean/sea-ice models, but neither include important ocean/ice shelf/fast-ice interaction processes or the circulation underneath ice-shelves. Marsland et al. [2004] used the years 1991-2000 to show an interannual variability in the wintertime heat flux, with weak (1991, 1992, 1999-2000) and strong (1993 through 1998 inclusive) states in the polynya activity corresponding to different states of circulation and magnitudes of DSW export from the region. Kusahara et al. [2011a] also examined DSW export from the same region. The model was shown to reproduce key water masses of the region and a seasonal variability in the export of DSW through the Adélie sill linked to the seasonal sea-ice production in coastal polynyas area, but did not include ISW formation.

The export of 100-500 mSv of DSW through the Adélie Sill observed in 1998 using ADCP moorings [Williams et al. 2008] is substantially higher than the modelled value of 70 mSv with the current sill section. This difference may be explained, however, by the assumption made by Williams et al. [2008] that the measured current magnitude was directed entirely through the Adélie sill. This assumption was necessary due to the absence of compass heading measurements on the moorings, so the true current direction could not be determined. Subsequent observations using current meters with compasses measure substantially less transport directed through the sill (73±83 mSv), which is in much closer agreement with the results from our study [Meijers et al. prep].

We show a net DSW export of 240 mSv from the Adélie depression compared to Marsland et al. [2004] who found 150 mSv. Kusahara et al. [2011a] found a stronger export through the Adélie sill (210 mSv) than through the Mertz sill (120 mSv), which is the opposite of our pattern with 70 mSv for the Adélie sill and 120 mSv for the Mertz sill. This difference in sill export is likely due to the circulation under the MGT connecting the two depressions, which is not included in either of the previous studies. Both earlier models consider the MGT as a land barrier separating the two depressions. As the polynyas are stronger in the Adélie depression area than in the Mertz depression area, Kusahara et al. [2011a] therefore shows more DSW exported from the Adélie sill than from the Mertz sill. In our model, the connection between the basins via the MGT cavity enables both the melting of the MGT and the transport of DSW from the Adélie depression to influence the Mertz depression,

and thus changes the ratio of DSW that is exported from each sill. In addition, both Kusahara et al. [2011a] and Marsland et al. [2004] cannot produce ISW, which means they may overestimate both the amount and density of the DSW, as demonstrated here by the experiment where we shut off ocean/ice shelf thermodynamics, which showed that DSW export is up to 100% stronger.

Table 2.3: Comparison of dense water export for observations and modelling studies (Sv)

Region	**Export (Sv)**	
This study (1992-2007)		
	Reference Simulation	Without Ice Shelf Thermodynamics
Adélie box	0.24±0.18	0.36±0.11
Mertz box	0.05±0.13	0.32±0.26
Adélie sill	0.07±0.06	0.14±0.07
Mertz sill	0.12±0.12	0.35±0.22
Cavity	0.12±0.07	0.16±0.08
Marsland et al. [2004] (1991-2000)		
Adélie depression	0.15	
Kusahara et al. [2011a] (1979-2008)		
Adélie sill	0.21±0.05	
Mertz sill	0.12±0.07	
Observations [Meijers et al. prep] (2008)		
Adélie sill	0.073±0.083	

2.5 Summary

The region near the Mertz Glacier Tongue (MGT) is known to be a source of Dense Shelf Water (DSW) that contributes to the formation of Antarctic Bottom Water (AABW) [Rintoul 1998; Marsland et al. 2004; Williams et al. 2008; Kusahara et al. 2011a] and is associated with intense polynya activity. Here we have used a regional ice shelf/ocean model to investigate the shelf sea processes controlling the export of DSW from the continental shelf in the vicinity of the MGT. The model is improved over previous studies in that it includes ice shelf/ocean interaction processes, and a cavity beneath the MGT linking the two major regional shelf depressions. Modelled DSW export is in good agreement with available, although sparse, observations.

Here we show that there is a delay of about a year between the change of polynya activity and the DSW export response. A single year of significantly weaker polynya

activity can limit DSW export. A prolonged strong or mean polynya state (> 1 year) is, however, needed for the volume of DSW on the continental shelf and depression to become large enough to escape the sill and move down slope to the abyssal ocean. We note, as previous studies have already done [Williams et al. 2010], that using a fixed critical density to define DSW is limiting and does not always capture the true export of DSW to the abyssal ocean. The critical value required for DSW to flow off-shelf should instead depend on the relative difference in the on-shelf DSW and the ambient off-shore water densities for greater accuracy.

The connection between basins under the MGT allows dense water (mainly High Salinity Shelf Water – HSSW) from the Adélie depression to enter the Mertz depression as well as contributing to ice shelf basal melt. The glacial meltwater produced further decreases the density of DSW, and limits the net export of DSW. We highlight that models without ocean/ice shelf interaction processes will significantly overestimate rates of DSW and AABW export. We also show that in addition to the Adélie and Mertz sills DSW can also flow out of the continental shelf through the north eastern edge of the Mertz depression, and along the coast to the west of the Adélie depression, although whether or not these pathways contribute to AABW formation is unknown.

Our study shows that DSW formed from active polynyas plays an important role in insulating ice shelves from melting by intrusions of relatively warm Modified Circumpolar Deep Water (MCDW). Here, our results suggest that during a sustained decrease in DSW formation, due to a reduction in the strength of the polynya activity (reduction in the strength of brine rejection), warm and salty MCDW will flow further on-shelf and drive higher ice shelf basal melting. The strong coupling between the polynya activity, DSW export and the basal melting of the MGT highlights the importance of understanding atmosphere-ocean-ice shelf interaction processes over the continental shelf seas, as well as exchange of water across the shelf break.

We show that high interannual sub glacial melting and the coupling between the polynya activity, the variability of the volume and the density of DSW and glacial meltwater is likely to be an important control on AABW variability. Unfortunately, the lack of long-term bottom water observations does not presently allow the evaluation of the interannual variability study in terms of DSW export and in terms of quantifying the AABW freshening due to atmospheric forcing.

Chapter 3

Sensitivity of ice shelf basal melting and dense shelf water formation to varying idealised winter surface conditions

3.1 Chapter outline

In this chapter, the sensitivity of ice shelf basal melting and Dense Shelf Water (DSW) formation to air/sea forcing is investigated. In Chapter 2, interannual variability in the air/sea forcing is identified as an important driver of interannual variability in both DSW export and ice shelf basal melting. Here, a simple set of numerical simulations of the two-dimensional overturning circulation (without Coriolis) are used to investigate the close relationship between air/sea forcing, DSW production and ice shelf basal melting. In this chapter, different relaxation times for the imposed temperature and salinity at the surface are used to simulate different sea ice growth rates (strong *versus* weak) and to evaluate the impact of different surface forcing on the vertical convection and modes of sub-ice shelf melting described by Jacobs et al. [1992]. The ocean circulation resulting from this type of forcing is buoyancy driven. The set of experiments used in this chapter are arranged to test different intensities of sea ice formation in winter, by changing the amount of salt injected into the ocean to drive convection (buoyancy driven).

The chapter is structured as follows:

- The description of the idealised model and the set of simulations used in this chapter are given in Section 3.2

- The sensitivity of the overturning circulation to the changes in surface forcing are described in Section 3.3.1
- The sensitivity of the overturning circulation to the changes in ice shelf basal melting are described in Section 3.3.2
- The relation between air/sea fluxes, basal ice shelf melt rate, warm water import and DSW outflow is discussed in Section 3.4

3.2 Model set up and experiments

The model used for this series of simulations is based on the Regional Ocean Modeling System (ROMS) [Shchepetkin and McWilliams 2005] and modified to include ocean/ice shelf thermodynamics [Galton-Fenzi et al. 2012]. The ocean/ice shelf thermodynamics are parameterised with the three equations from Holland and Jenkins [1999] that allow the estimation of the ice shelf basal melting and freezing. For simplification, the model set up used here does not include frazil ice thermodynamics within the water column and there is no tidal forcing. In addition, the Coriolis parameter is not used in these simulations as they are restricted to two dimensional overturning. The model has a free surface and uses terrain following vertical s-coordinate, which has been adapted to allow the coordinates to follow the ice shelf draft [Dinniman et al. 2003] and to increase the resolution in the upper and lower cells of the water column.

Model domain and spatial resolution:

Choices of the model domain were made to be similar to the Ice Shelf Ocean Model Intercomparison Project (ISOMIP) geometry 2 [Hunter 2006], also used in Gwyther et al. [2016] with ROMS. However, the model set up here is different from the ISOMIP experiments as ISOMIP is three-dimensional. Also, the model domain extends to 500 km on a north-south section (instead of 10° in latitude for ISOMIP – about 1,111km) and 50 km on an east-west section to keep the domain as close as possible to two-dimensional study using free-slip side walls. The bathymetry is set at a uniform depth of 600 m, and the ice shelf draft follows a linear southward downslope from 100 m depth to 500 m at the southern boundary along 100 km (Figure 3.1). For these simulations, the vertical grid use 11 levels that correspond to approximately 3 to 17 m vertical resolution at the southern boundary under the ice shelf, 13 to 84 m under the ice shelf front and 15 to 100 m vertical resolution for the open ocean. The horizontal resolution is 5 km.

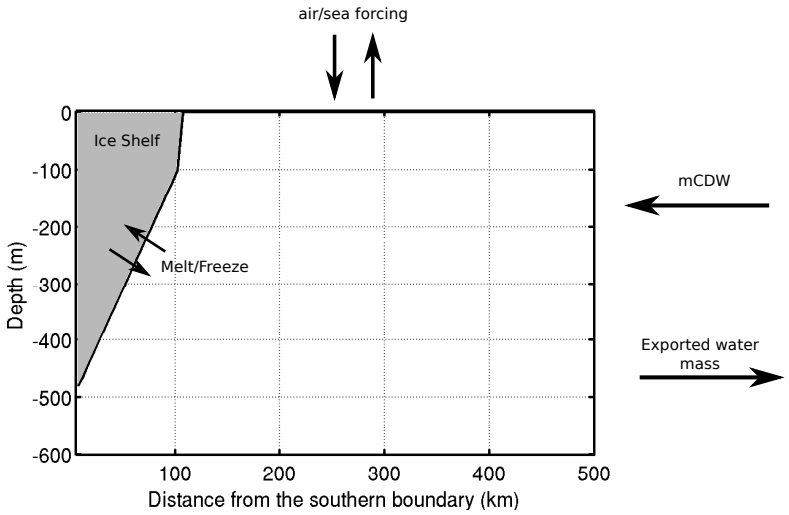

Figure 3.1: Schematic of the model domain (cross section) with the fluxes studied in this chapter.

Boundary conditions:

The southern, eastern and western boundaries are closed walls, so external forcing arise from the northern boundary or the surface forcing applied for each simulation. Also, water masses can be modified due to the ocean/ice shelf thermodynamics enabled in the model. The northern boundary is open using the radiation condition in ROMS, ensuring that any water leaving the domain is replaced by incoming water with the potential temperature of -1 °C and salinity of 34.6, that can form a water

mass with a potential density of 1027.83 kg m^{-3}. These water mass properties are similar to modified Circumpolar Deep Water (mCDW) that is present off the continental shelf of the Adélie and George V Land (AGVL) region. For simplicity, the potential density discussed in this chapter will be the anomaly of the computed potential density (- 1000 kg m^{-3}). In this case the potential density will be noted 27.83 kg m^{-3}. Salinity values used here are on the Practical Salinity Scale (PSS78) and are dimensionless.

In ROMS, the radiation condition determines whether an open boundary is active (inflow) or passive (outflow). When the boundary is active, dynamical equations require external information and the solution can be strongly nudged towards external values without causing an over-specification problem. In the active-boundary case, the radiation extrapolation is applied and allows the information from the interior solution to pass through the boundary without strong reflection [Marchesiello et al. 2001]. Here, the radiation condition is used at the northern boundary with a relaxation time (nudging) of 1 day on the inflow, while no relaxation scheme is set on the outflow. This way, the inflowing water mass is driven by the amount and location of the outflowing water mass (top or bottom half of the water column).

Initial conditions and air/sea forcing:

The model is initialised with an homogeneous potential temperature of -1.6 °C and salinity of 34.4 over the whole domain. At the surface of the ocean, the temperature is relaxed to surface freezing conditions of -1.90 °C and a salinity of 34.6 using relaxation times of 0.5 - 1.5 days. Here, 'winter conditions', or constant surface freezing conditions, are used to represent the latent heat polynya conditions in the lee of an ice shelf. Surface temperature and salinity relaxation was preferred instead of relaxing to a known surface heat and salt fluxes to allow the model to produce water masses with known temperature and salinity (therefore density). This set up has previously been used in ISOMIP experiments, such as in Gwyther et al. [2016]; Hunter [2006] and similarly to [Olbers and Hellmer 2010] box model circulation and melting within an ice shelf cavity.

In these idealised simulations, the salt flux resulting from the freezing of the ocean surface is only applied when the surface of the ocean is at freezing temperature. Restoring the surface of the ocean to a temperature close to the surface freezing temperature induce a negative heat flux (cooling) until the surface of the ocean

reaches the *in-situ* surface freezing temperature and then the surface salinity is restored to the prescribed salinity resulting in a positive salt flux (input of salt) to represent the sea ice formation. The sea ice is then assumed to be transported outside of the domain, so it does not melt within the domain (no fresh water input at the surface). The constant cooling and salt input when the surface is at freezing temperature aims to drive convection (and HSSW formation) at different intensities relative to the relaxation times used in each simulation, resulting in the formation of water masses with different densities for each simulation.

Experiments:

A set of four 'winter condition' simulations are analysed in this chapter, therefore no annual cycle is parameterised in the simulations. To represent freezing conditions, different relaxation time for the surface salinity and its corresponding freezing temperature are used (Table 3.1). These experiments are buoyancy driven due to the density induced at the surface by the prescribed potential temperature and salinity, and the density of the water mass prescribed at the northern boundary. The main difference between the simulations is the relaxation time used for the salinity and potential temperature at the air/sea interface. The salinity prescribed at the surface is the same as prescribed at the northern boundary. Using different relaxation time drives changes in the salt input into the ocean and consequently changes the density of the water mass formed via the air/sea forcing for each simulation.

A reference simulation ('ref') is analysed using a surface salt and potential temperature relaxation time of 1 day. To evaluate the impact of the glacial meltwater within the water column of the entire model domain, the same simulation was run with no ocean/ice shelf thermodynamics ('no melt'). A shorter relaxation time of 0.5 day is used to simulate stronger air/sea forcing ('strong') and represent a more intense sea ice formation (higher rate of brine rejection). As opposed to the 'strong' simulation, a 'low' forcing condition is also applied using a surface relaxation time of 1.5 days to simulate weaker rate of sea ice formation. The model ran for 15 years and reached equilibrium after about 11 years of runtime. Only the average of the final year is used for further analyses in this chapter.

Table 3.1: Surface forcing conditions (prescribed surface temperature, salinity and relaxation time) for each experiment. The surface temperature corresponds to the surface freezing point for a water mass with a prescribed surface salinity.

Simulations	Potential Temperature (°C)	Salinity	Time relaxation (days)
ref	-1.90°C	34.6	1
no melt	-1.90°C	34.6	1
strong	-1.90°C	34.6	0.5
low	-1.90°C	34.6	1.5

3.3 Results

3.3.1 Ocean circulation

By examination of the meridional overturning circulation and meridional water mass properties, the 'ref' simulation shows an expected overturning circulation beneath the ice shelf (Figure 3.2a and b). The prescribed surface temperature and salinity drive dense (> 27.84 kg m^{-3} – Figure 3.2a) and cold (Figure 3.2b) water to sink in the ocean domain between about 130 km to 250 km away from the southern boundary. Heat and salt fluxes at the ocean/ice shelf and ocean/air interfaces are shown in Figure 3.3 for each simulation and illustrate where the salt is injected into the domain. The brine rejection drives a clockwise overturning circulation underneath the ice shelf with a fresh glacial melt water plume rising along the ice shelf to the surface of the ocean, typical the first mode of sub-ice shelf melting described by Jacobs et al. [1992] and also associated to an 'estuary' mode as the ice shelf melting acts like a river. The rest of the domain is driven by an anti-clockwise circulation that is divided from the ice shelf circulation by a 'separation' streamline at approximately 130 km from the southern boundary, that acts as a dynamical barrier (Figure 3.2b). It is interesting to note that the model does not manage to relax to the exact prescribed surface temperature and salinity, but instead produces a water mass with a salinity of about 34.58. However, this water mass is sufficiently dense to sink to the sea floor. This cold and dense water mass (HSSW-type) circulates towards the ice shelf cavity and interacts with the base of the ice shelf.

The water mass that reaches the cavity is warmer than the local freezing temperature and is able to drive melting of the base of the ice shelf. Also, the clockwise circulation within the cavity and just outside the cavity is almost thermodynami-

cally independent of the circulation in the rest of the domain due to the dynamical barrier. Heat from the northern part of the domain can only flow across the streamline via diffusion. From the ice shelf melting, a fresh and cold plume, that will always be lighter than the water mass driving the melt rate, rises along the ice shelf and reaches the surface of the open ocean at the front of the ice shelf (Figure 3.2a and b). The Potential Temperature - Salinity (θ-S) diagram at different locations along the model domain (Figure 3.2c) illustrates the cooling of the surface water, in the middle of the domain (red dots), towards the surface freezing temperature. The water mass below the surface freezing point is called Ice Shelf Water (ISW) and is a mixture of glacial meltwater and water masses driving the ice shelf basal melting. This ISW plume is at or below the surface freezing temperature when reaching the surface of the ocean at the ice shelf front (orange dots in Figure 3.2c).

Surface heat flux at the air/sea interface in the model represents the effective heat flux (Figure 3.3a). The surface forcing are set to cool the surface of the ocean until the surface freezing temperature, before to input salt into the ocean (Figure 3.3b). In other words, the heat flux from the model output is the effective strength of the model trying to cool the surface water, while the surface salt flux illustrates the polynya activity by adding salt into the domain where the surface temperature is at or below surface *in-situ* freezing temperature (condition to form sea ice). If the surface temperature is below the prescribed freezing temperature (in front of the ice shelf front) the model restores to the prescribed temperature and add salt to simulate sea ice growth. In the case where the surface temperature is above the prescribed surface freezing temperature, the model relaxes towards the prescribed temperature without adding salt until it reaches the *in-situ* surface freezing temperature.

The ISW plume explains the positive heat flux (Figure 3.3a) just in front of the ice shelf as the potential temperature is below the prescribed potential temperature (-1.90 °C). However, this is where the salt flux into the ocean is at maximum (Figure 3.3b), illustrating that the water mass near the ice shelf front is fresher compared to the prescribed surface salinity and can only be produced by the ice shelf basal melting. In the rest of the domain, from 150 km away from the southern boundary to the northern boundary, the heat flux is negative (cooling), while the salt flux is at zero, illustrating that no salt is injected into the ocean as the surface temperature is not at the surface freezing temperature. This situation represents open water conditions (no sea ice production).

The northern boundary prescribes a relatively warm water (mCDW-type) flowing across the boundary and towards the ice shelf in the upper half of the water column. At the surface, this water mass is quickly eroded (cooled) due to the surface forcing that tries to bring the surface layer to the surface freezing temperature. This is shown with the surface heat flux (Figure 3.3a), that is strongly negative near the northern boundary (about -300 W m^{-2}). On the other hand, the salt flux near the northern boundary is equal to zero as the surface temperature is not at the surface freezing temperature. Fast cooling at the surface of the model domain occurs, and the convection of the HSSW-type closer to the ice shelf front pulls the incoming mCDW-type downward between 150 and 250 km away from the southern boundary. Similarly, the outflowing water mass is warmer than the prescribed surface temperature, due to mixing with the warmer inflowing water mass.

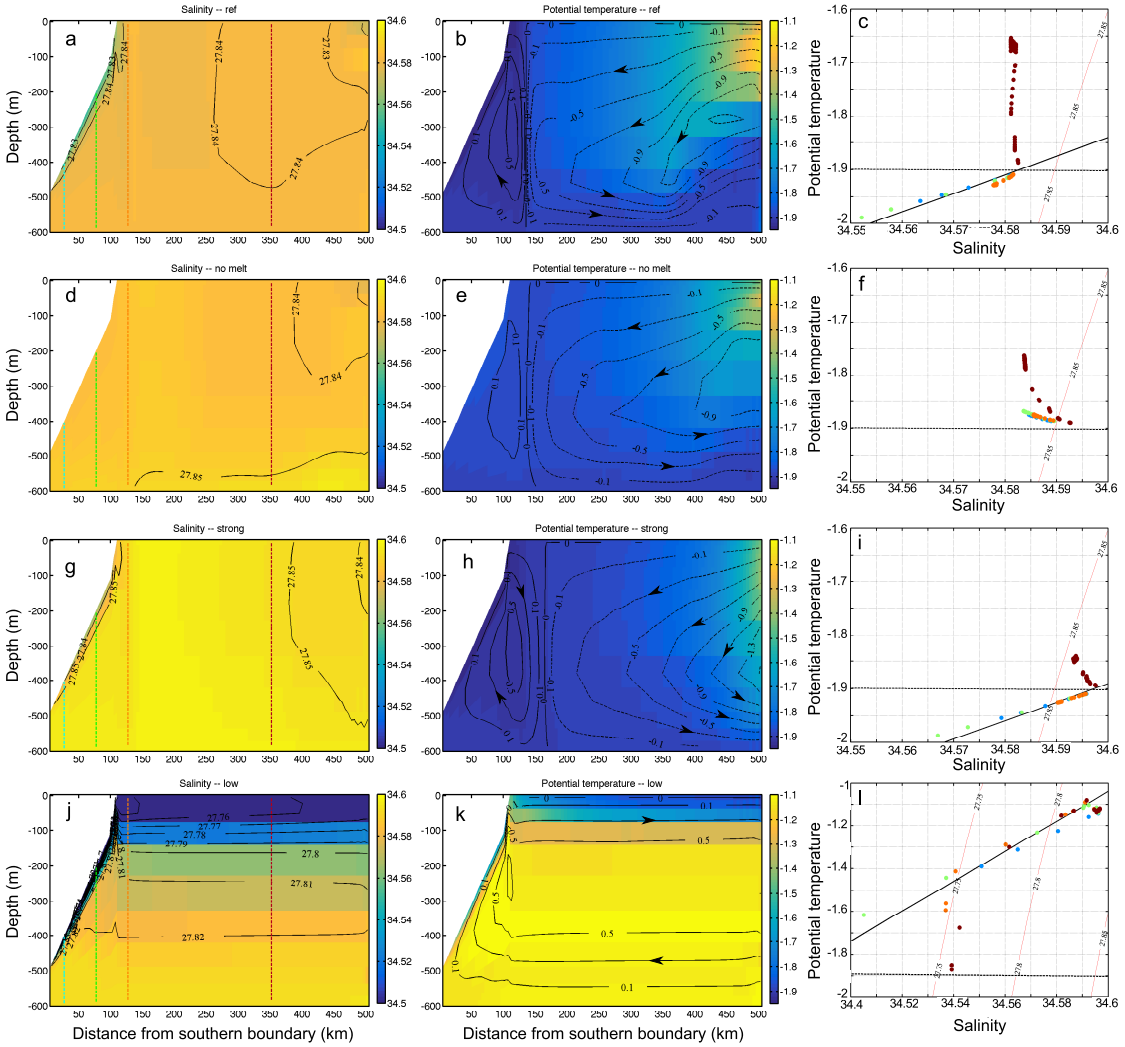

Figure 3.2: Section along the model domain for each simulation, 'ref' (a, b and c), 'no melt' (d, e and f), 'strong' (g, h and i) and 'low' (j, k and l) forcing simulation. Salinity, overlaid with potential density contours (kg m^{-3}) are in the left column panels, potential temperature (°C) overlaid with the overturning streamfunction contours (Sv, positive is a clockwise overturn) are in the middle column panels. Potential Temperature - Salinity (θ-S) diagrams for 4 vertical profiles of each simulation are in the right column panels. Each colour on the θ-S diagrams correspond to a vertical profile shown on each salinity panels. The inclined straight lines are the Gade Lines [Gade 1979] described in the text and the dashed lines correspond to the surface freezing temperature.

To investigate the impact of the ISW, the 'no melt' simulation is forced with the same air/sea forcing as the 'ref' simulation but with no ocean/ice shelf thermodynamics; heat and salt fluxes beneath the ice shelf are set to zero. The water column is cooled by the air/sea forcing and forms a bottom layer denser than in the 'ref'

simulation with a potential density of 27.85 kg m^{-3} (Figure 3.2d and e). Similarly to the 'ref' simulation, two overturning cells are present in the 'no melt' simulation with a 'separation' streamline at about the same location as the 'ref' simulation. However, the overturning cells are weaker, in particular the clockwise cell beneath the ice shelf. The weaker vertical convection in the 'no melt' simulation is due to weaker heat and salt fluxes near the ice shelf front.

As expected, no ISW-type with low salinity and potential temperature below the surface freezing point is present in the domain (Figure 3.2f). In the 'ref' simulation the fresh ISW plume drives stronger salt input just at the ice front edge (Figure 3.3b). In the 'no melt' simulation, the surface salt flux is positive (salt input into the ocean) near the ice shelf but weaker than in the 'ref' simulation. However, the salt flux is positive on a wider area in the 'no melt' simulation, from the ice shelf front to ∼250 km away from the southern boundary. The fact that salt is input over a wider area of the open water of the 'no melt' simulation, drives denser water to sink to the sea floor. Also, the 'no melt' simulation is saltier over the entire model domain by 0.006 compared to the 'ref' simulation. As for the 'ref' simulation, the surface heat flux is strongly negative near the northern boundary due to the inflowing mCDW-type, but less intense than in the 'ref' simulation as the mCDW at the northern boundary is cooler (Table 3.2). Within the area of the ice shelf cavity overturning cell, the 'no melt' simulation is warmer by 0.04 °C compared to the 'ref' due to no cooling from the ice shelf.

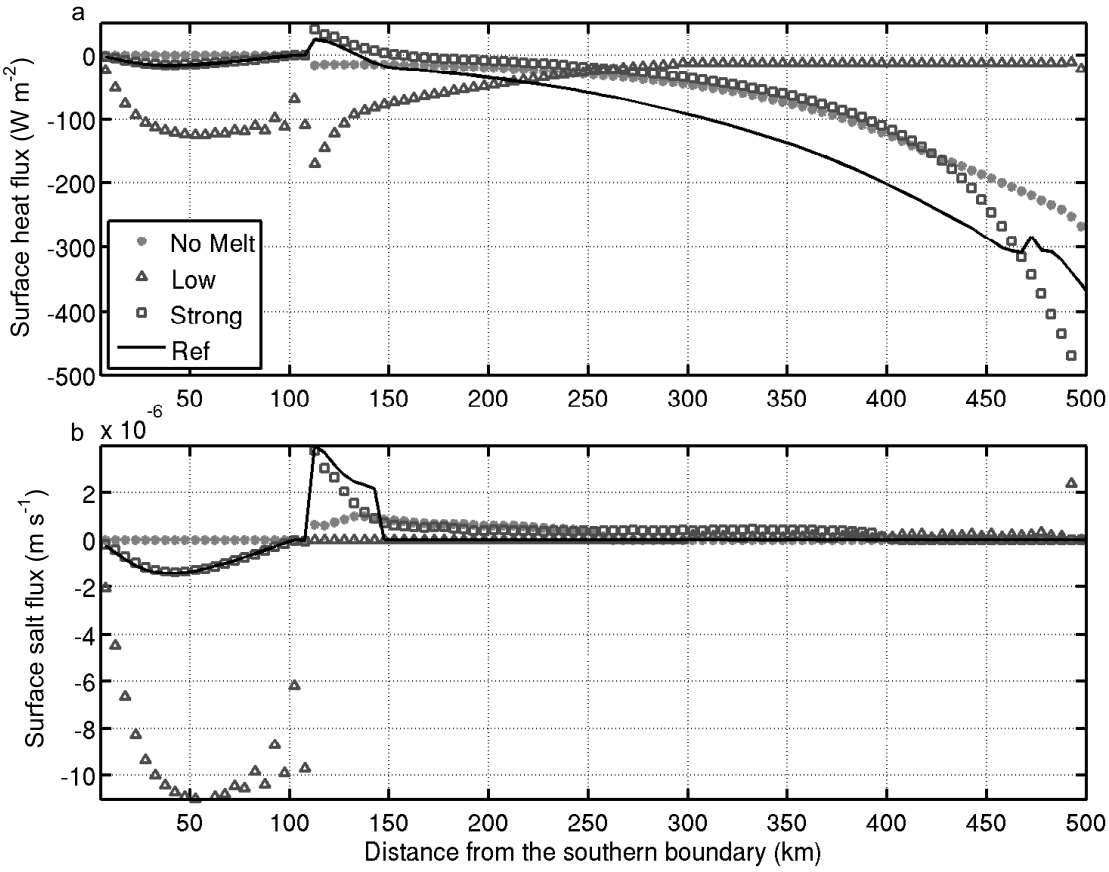

Figure 3.3: Surface heat (a) and salt (b) fluxes along the north-south view of the domain. The ice shelf extend from the southern point (0 km) to 100 km. The solid line represent the 'ref' simulation, the grey filled-circles the 'no melt', the open squares the 'strong' and the open triangles the 'low' forcing simulation. A negative heat flux illustrate a cooling of the ocean surface.

The 'strong' forcing simulation (Figure 3.2g, h and i) is very similar to the 'ref' simulation, forming a denser water mass (HSSW-type, > 27.85 kg m^{-3}) than in the 'ref' simulation (> 27.84 kg m^{-3}). The overturning circulation underneath the ice shelf is about the same intensity as in the 'ref' simulation but covers a wider area, driving the 'separation' streamline further north compared to the 'ref' simulation (at approximately 170 km away from the southern boundary instead of 130 km for the 'ref'), resulting in the mCDW not penetrating as far south as in the 'ref' simulation. Near the ice shelf front, the surface heat flux is higher and positive (adding heat into the ocean) in the 'strong' compared to the 'ref' simulation, due to the cooler ISW plume rising from beneath the ice shelf to the surface of the ocean. However, the negative surface heat flux further north, in the 'strong' simulation, has a weaker cooling effect than in the 'ref' simulation because the surface water is closer to the

surface freezing temperature than in the 'ref' simulation.

The salt flux is positive from the ice shelf front until 400 km away from the southern boundary, driving a wider convection which explains the change of location of the 'separation' streamline. The steep curvature of the surface heat flux from the 'strong' simulation towards the northern boundary illustrates the intense cooling effect, eroding very quickly the warm water flowing from the northern boundary. However, the average heat flux for the 'strong' simulation is -100 ± 30 W m^{-2} is similar to the 'ref' simulation (-131 ± 2 W m^{-2}). It is important to note that the high variability of the 'strong' forcing simulation heat flux illustrates a highly variable surface temperature due to highly variable transport of warm water into the domain (Figure 3.2g and h) from the northern boundary of 1.3 ± 0.3 Sv for the inflow, while the 'ref' simulation as a more constant transport across the northern boundary of 0.99 ± 0.02 Sv (Table 3.2).

The 'low' forcing simulation induces a change in the ocean circulation within the model domain and a clear threshold is passed between the 'ref' and the 'low' simulations (Figure 3.2j, k and l). The surface relaxation time of 1.5 day produces a lighter water mass that is not able to sink and convect to the sea floor. Instead, the inflowing mCDW enters the model domain across the lower half of the water column to drive a single clockwise overturning cell within the entire domain, this is the second mode of sub-ice shelf melting described by Jacobs et al. [1992]. Warm deep water (about -1.11 °C – Table 3.2) enters the domain and directly interacts with the ice shelf, driving a buoyant meltwater plume to the surface that flows northward and stratifies the water column with cooler potential temperature (-1.60 °C) and a lower salinity (34.51 – Table 3.2), which is very different from the three other simulations where the 'separation' streamline insulates the ice shelf cavity from warm water intrusions.

At the surface and near the ice front, strong cooling (negative heat flux) and near zero salt flux illustrate that the fresh water plume is not at the surface freezing temperature, meaning that the melting driven by the warm inflowing mCDW forms an ISW that is fresh and above the surface freezing temperature in this simulation. The surface heat flux averaged over the entire area of open water is weak (-32.59 ± 0.08 W m^{-2}) due to the buoyant plume of ISW formed due to the melting that has a potential temperature close to the surface freezing temperature. As a result, the exported water mass is mainly cooled by the melting of the ice shelf, and

insulates the warm mCDW flowing into the domain at depth from the prescribed surface freezing conditions. Thus, the warm inflowing water mass reaches the ice shelf cavity after undergoing minimal modifications.

Table 3.2: Northern boundary water properties (potential temperature – θ – and salinity – S) for inflowing ($_{in}$) and outflowing ($_{out}$) water masses, associated with the transport (Sv) across the boundary (trp_{in} and trp_{out}).

Simulations	$\bar{\theta}_{in}$	$\bar{\theta}_{out}$	$\bar{S}_{in}$	$\bar{S}_{out}$	$\bar{trp}_{in}$	$\bar{trp}_{out}$
ref	-1.229	-1.835	34.580	34.583	0.99 ± 0.02	1.02 ± 0.02
no melt	-1.429	-1.841	34.583	34.590	0.91 ± 0.07	0.93 ± 0.07
strong	-1.457	-1.764	34.591	34.595	1.3 ± 0.3	1.3 ± 0.3
low	-1.115	-1.598	34.587	34.510	0.6736 ± 0.0002	0.6035 ± 0.0006

3.3.2 Ocean/ice shelf interface

The melt rate in the model is governed by two factors, the thermal driving and the friction velocity that are used in the parameterisation of turbulent heat and fresh water transfer at the ocean/ice shelf interface, described by Holland and Jenkins [1999]. The thermal driving is defined by Holland and Jenkins [1999] as:

$$T_* = T_M - T_B, \tag{3.1}$$

where T_M is the *in situ* temperature at the top layer of the model beneath the ice shelf and T_B is the *in situ* freezing temperature within the ocean/ice boundary layer (pressure dependent). In this study, T_B is calculated assuming that the pressure and the salinity at the top layer of the model are the same as within the ocean/ice boundary, which is similar to other studies such as Gwyther et al. [2016] and Dansereau et al. [2013]. The friction velocity is directly linked with the current velocity beneath the ice shelf and is calculated as follows:

$$u_* = \sqrt{Cd}\, U_M, \tag{3.2}$$

where $Cd = 0.005$ is the dimensionless drag coefficient, spatially constant over the entire ice shelf and U_M is the model top layer velocity (m s^{-1}) directly underneath the ice shelf, which is known to be an important driver of the basal melting [Gwyther et al. 2016; Dansereau et al. 2013].

The pattern of the ice shelf basal melting for the 'ref' simulation (Figure 3.4a – solid line) shows near zero melting at the grounding line, maximum melting at the lower half of the ice shelf (about 40 km north of the grounding line) and refreezing at the ice shelf front. The minimum melt rate (Figure 3.4a) is correlated with the maximum thermal driving (Figure 3.4b) and the minimum value of the friction velocity (Figure 3.4c). The low friction velocity near the southern point of the domain explains the near zero melting while the thermal driving is high. The friction velocity increases along the ice shelf as the ISW plume rises and the thermal driving decreases as glacial meltwater is released into the ocean. The melt rate reaches the maximum value when both thermal driving and friction velocity reach an equilibrium (Figure 3.4d).

It is interesting to note that for the 'no melt' simulation the thermal driving is linear along the ice shelf base. For this simulation, no heat and salt fluxes (no melt) are prescribed beneath the ice shelf, so there is no cooling or freshening of the ocean by the ice shelf. However, thermal driving and friction velocity can be calculated. The thermal driving is linear following the change in local freezing temperature due to the change in pressure (Figure 3.4b). However, the friction velocity along the ice shelf draft does not increase linearly (Figure 3.4c), in particular for the upper half of the ice shelf, where $T_* u_*$ is maximum at about 60 km (Figure 3.4d). In parallel, T_* almost doubles in the 'no melt' simulation within the ice shelf cavity compared to the 'ref' simulation, as no glacial meltwater is released from the melting of the ice shelf to cool the water column within the ice shelf cavity.

The 'strong' simulation is similar to the 'ref' simulation and the averages of melt rate, T_* and u_* are about the same, 0.76 m yr^{-1} and 0.78 m yr^{-1} respectively for the melt rate (Table 3.3). However, the 'low' forcing experiment is very different with an area-averaged melt rate reaching 8.45 m yr^{-1} (990% higher than the 'ref' simulation). The maximum melt rate is at mid ice shelf (about 50 km from the grounding line) and then plateaus until the ice shelf front, while the thermal driving is maximum at the grounding line and the friction velocity is at its minimum (corresponding to the minimum area averaged melt rate). The 50 km mark corresponds to an ice draft of about 400 m depth, which is also the depth of the warmest layer from the inflowing mCDW that interacts with the ice shelf (Figure 3.2l).

The 'low' forcing experiment is more sensitive to thermal driving than to the friction velocity. The averaged friction velocity in the 'low' simulation is only doubled

compared to the 'ref', while the thermal driving is almost 300% higher and the area-averaged melt rate is about 11 times higher (990%, Table 3.3). Gwyther et al. [2016] use the same model, but with a different set up (e.g. wider domain, closed boundary, Coriolis parameter) to perform similar studies focused on the ice shelf melting and its driver for different ocean conditions. They also found that the melt rate distribution in a hot cavity environment (comparable to the 'low' forcing simulation here) is more correlated with thermal driving, while in a cold cavity environment (comparable to the 'ref' and 'strong' forcing simulations here) the melt rate distribution is mostly driven by the ocean circulation.

Table 3.3: Area-averaged melt rate (m), averaged friction velocity (u_*) and averaged thermal driving (T_*) along the base of the ice shelf for each experiment. The percentage of change for each simulation compared to the 'ref' simulation is given in square brackets.

Simulation	m (m yr^{-1})	u_* (m s^{-1})	T_* (°C)
Ref	0.78	3.6 e^{-3}	0.15
No melt	0.00 [-]	1.3 e^{-3} [-60%]	0.25 [+67%]
Strong	0.76 [-3%]	3.5 e^{-3} [-3%]	0.15 [0%]
Low	8.45 [990%]	7.5 e^{-3} [+108%]	0.59 [293%]

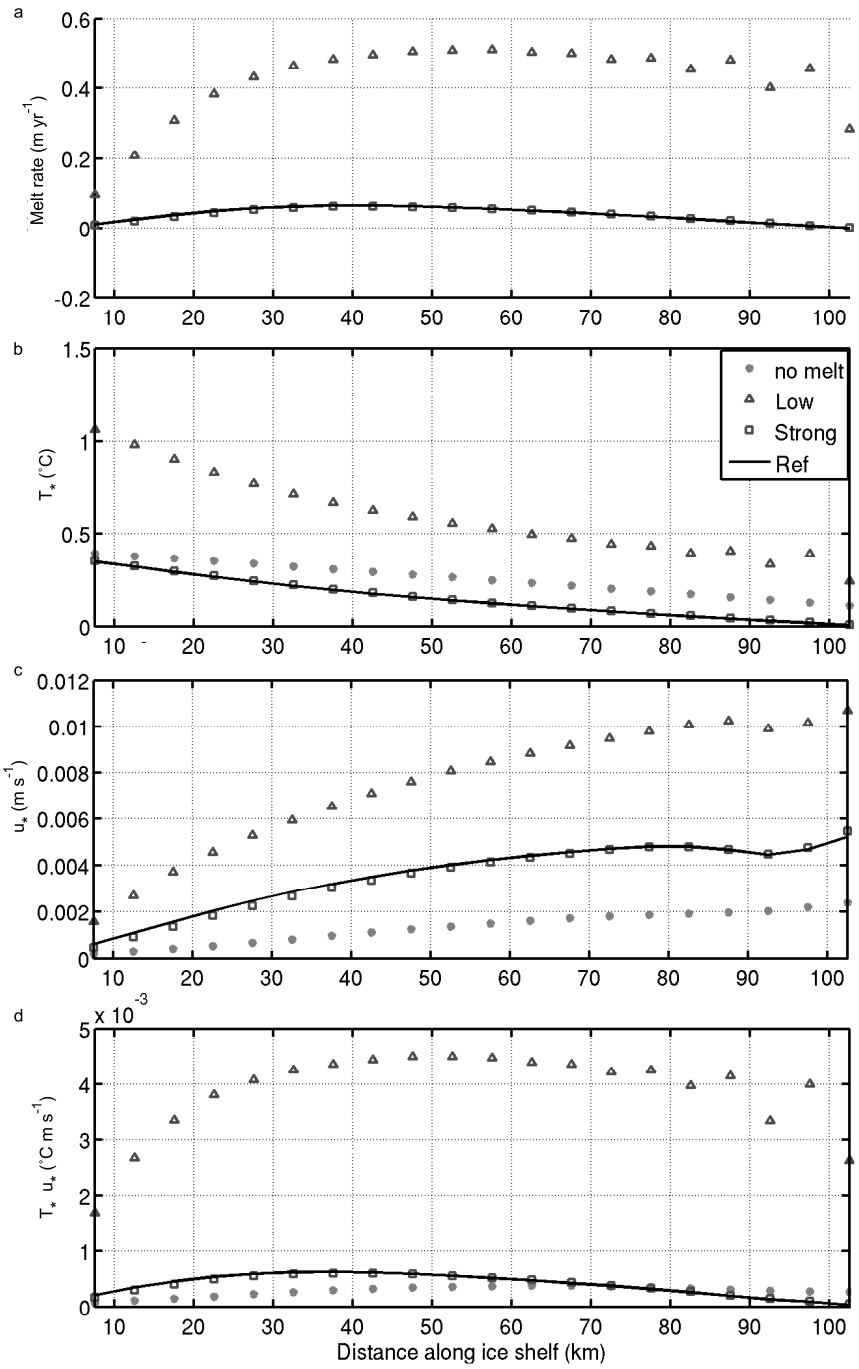

Figure 3.4: Ice shelf basal melt rate (a), thermal driving (T_*: b), friction velocity (u_*: c) and $T_* u_*$ (d) along the ice shelf base for each experiment. As for Figure 3.3 the 'ref' simulation is represented with the solid line, 'no melt' with grey dots, 'strong' with squares and 'low' simulation with triangles.

3.4 Discussion

The change in ocean circulation and ice shelf basal melting for the 'low' forcing simulation is significant. From a relatively homogeneous water column in front of the ice shelf front for the 'ref' and 'strong' forcing scenarios, the 'low' forcing switches to a stratified water column for the whole domain. The 'ref' and 'strong' simulations could be compared to the Mertz Glacier Polynya (MGP) region, with the latent heat polynya forming intense brine rejection that convects to the sea floor along the coast and the local ice shelf. On the other hand, the 'low' forcing simulation could be compared to the Pine Island Glacier (PIG) region. PIG in West Antarctica undergoes strong melting due to warm mCDW entering the ice shelf cavity at depth and interacting with the base of the ice shelf, measuring water mass near the grounding line with an *in-situ* temperature of about +4 °C above the local freezing temperature [Jacobs et al. 2011].

The impact of the ice shelf meltwater on water mass transformation is seen on the Potential Temperature - Salinity diagram (θ-S diagram, Figure 3.2c, f and l). For the 'ref' and 'strong' forcing simulations, interactions with the ice shelf forms a fresher and cooler (below surface freezing temperature) water mass, following a linear profile (solid black line on the figure). This solid line on Figure 3.2c, f and l show the trajectory of a water parcel in θ-S scape when interacting with the base of an ice shelf and is called a Gade Line [Gade 1979]. The water mass driving the ice shelf melting in the 'ref' and 'strong' simulations, is the saltiest water within the domain (about 34.58 and 34.60 respectively) with a potential temperature near the surface freezing temperature. This is mode 1 of sub-ice shelf melting described by Jacobs et al. [1992], where HSSW driven by the brine rejection due to sea ice formation interacts with the deepest part of the base of the ice shelf. On the other hand, the 'low' simulation has an ice shelf melting driven by the warmest (and saltiest) water mass in the model domain. This corresponds to mode 2 of sub-ice shelf melting [Jacobs et al. 1992], where an inflow of relatively warm mCDW interacts with the ice shelf.

The basal ice shelf melt rate pattern (Figure 3.4a) along the ice shelf shows the differences between the two regimes ('strong' and 'ref' *versus* 'low' forcing). For the 'strong' and 'ref' simulations with an ice shelf melting driven by HSSW (HSSW regime) the maximum melt rate occurs when $T_* u_*$ is maximum (about 40 km away from the southern boundary) and not when the thermal driving is maximum. It is

similar for the 'low' forcing simulation where the ice shelf basal melt rate is driven by mCDW (mCDW regime). However, the maximum melt rate is further north (about 50 km away from the southern boundary), and plateaus until the ice shelf. Both regimes follow a linear profile when comparing the melt rate to $T_* u_*$ (Figure 3.5) with a y-intercept at almost zero and a high coefficient of determination (R^2) of almost 1; T_* and u_* control the melt rate. However, for the deep ice of the 'low' simulation, the melt rate values depart from the linear fit. As discussed earlier, the thermal driving here is calculated using the *in-situ* freezing temperature at the top layer of the model and not directly at the ocean/ice boundary, that could explain that the deep ice melt rate is not aligned on the linear fit in Figure 3.5 due to strong ocean heat flux interacting directly with the ice shelf.

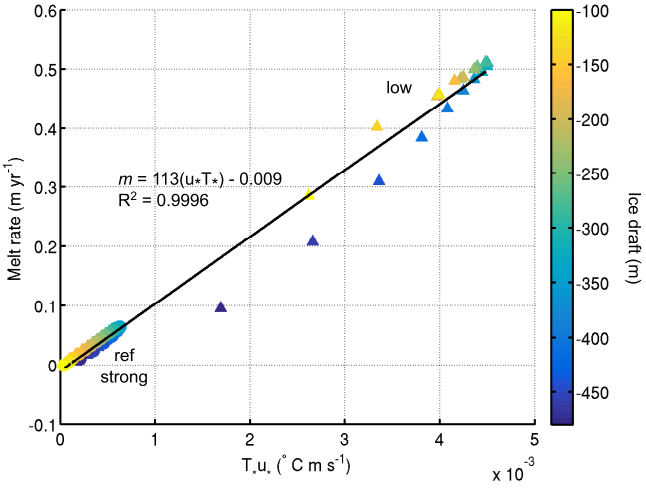

Figure 3.5: Melt rate (m yr^{-1}) in function of the thermal driving times friction velocity ($T_* u_*$: °C m s^{-1}). The colour scale is the corresponding depth of the ice draft (m). Circle and square symbols are for the 'ref' and the 'strong' simulations respectively and the triangles for the 'low' simulation.

To link the impact of the air/sea fluxes on the water masses at the northern boundary, Figure 3.6 summarises the water properties across the northern boundary for the inflowing and outflowing water masses (Table 3.2) in potential temperature - salinity space relatively to the averaged surface heat flux for the open water. It is interesting to note that the inflowing water mass for each simulation have different properties (potential temperature and salinity). Salinity is similar between each inflowing water mass and ranges only between 34.58 and 34.59, while the potential temperature of the inflowing water mass ranges between -1.1 to -1.45 °C.

In the 'ref', 'no melt' and 'strong' simulations the outflowing water mass is colder and saltier than the inflowing water mass due to cooling and addition of salt by the surface forcing. The 'strong' forcing simulation exports the densest water mass (> 27.85 kg m^{-3}) compared to the other simulations, however similar to the 'ref' and the 'no melt' simulations. The area averaged surface heat flux for the 'ref' simulation is -131 $\pm$ 2 W m^{-2}, -98 $\pm$ 12 W m^{-2} for the 'no melt', and -100 $\pm$ 30 W m^{-2} for the strong simulation, which is fairly similar according to the high variability of the 'strong' simulation. However, the 'low' forcing simulation (mCDW regimes, triangle on Figure 3.6) is very different. The exported water mass is colder (-0.48 °C) but also fresher (-0.077) than the inflowing water mass across the northern boundary. Also, the surface heat flux at the air/sea boundary is much lower than the other simulations with -32.59 $\pm$ 0.08 W m^{-2}.

The main difference between the 'ref'/'no melt'/'strong' and the 'low' simulations is the presence or not of the 'separation' streamline. In the HSSW regime ('ref', 'no melt' and 'strong') this front acts as a dynamic barrier that blocks the mCDW to interact directly with the ice shelf. The surface heat and salt fluxes between the ice shelf front and the 'separation' streamline can impact on the ice shelf basal melting and change the ocean conditions within the ice shelf cavity. The only way that heat flux from the northern boundary could impact the ice shelf is by horizontal diffusion. On the other hand, the 'low' simulation has a single cell overturning circulation. There is no dynamic barrier that protects the ice shelf from the warm mCDW intrusion. Instead, the ocean heat circulates directly to the ice shelf cavity driving high melting and forming a buoyant water mass that stratifies the water column.

The change of location of the 'separation' streamline between the 'ref' and the 'strong' simulations, illustrates that if the freezing conditions are intense (highly negative heat flux and high salt flux), like in an intense latent heat polynya region (MGP for instance), dense HSSW is formed and the dynamical barrier moves away from the ice shelf front. Warm mCDW intrusions do not penetrate as far towards the ice shelf and the 'separation' streamline insulates the ice shelf cavity from the mCDW heat flux. Eventual the 'separation' streamline can move as far as the model domain extend, or at the shelf break in a more realistic scenario. On the other hand, when the freezing conditions are less intense, the water mass formed via the surface fluxes drives a water mass with a density closer to the mCDW and the 'separation' streamline moves closer to the ice shelf front. The mCDW intrusions flow closer to

the ice shelf cavity, until it reaches a threshold where the water mass formed via the surface fluxes drives a water mass lighter than the mCDW and the dynamical barrier disappear as no dense water mass is formed, leading the mCDW to interact directly with the ice shelf.

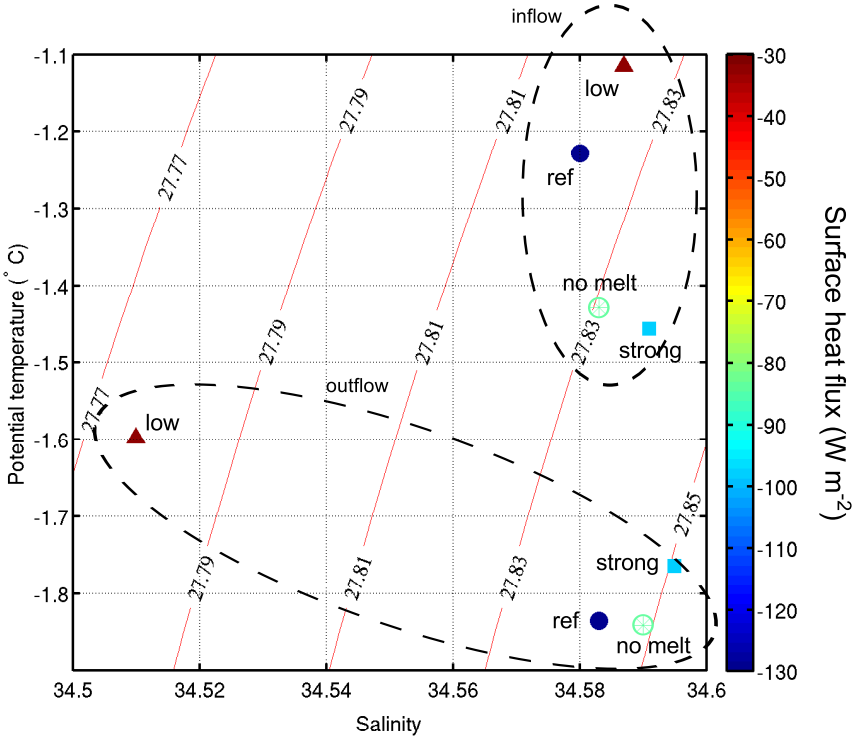

Figure 3.6: Potential temperature and salinity for each simulation for the inflowing (above -1.5 °C) and outflowing (below -1. 5°C) water masses at the northern boundary, coloured by the open water surface heat flux. Triangles represent the 'low' forcing simulation, squares the 'strong' and the circles (circled stars) the 'ref' ('no melt').

3.5 Summary

In this chapter, a set of four two-dimensional simulations, based on the Regional Ocean Modelling System (ROMS) [Shchepetkin and McWilliams 2005] model, were used to test idealised winter conditions applied at the surface of the ocean. Two regimes of ocean circulation are found and described in this study. The first regime is called 'HSSW regime' and is driven by the vertical convection of the densest water mass formed via air/sea fluxes. This regime is similar to the conditions in the region of the Mertz Glacier Polynya and corresponds to the mode 1 of sub-ice shelf

melting described by Jacobs et al. [1992]. On the other hand, the second regime ('mCDW regime') is driven by an inflow of warm mCDW that reaches the ice shelf cavity at depth. This is typical of the Pine Island Glacier in West Antarctica and corresponds to the mode 2 of sub-ice shelf melting described by Jacobs et al. [1992].

The major conclusions of this chapter are as follow:

- The HSSW regime with air/sea fluxes strong enough to drive convection of denser water masses, that results in forming an homogeneous water column in front of the ice shelf front. The dynamical barrier insulates the ice shelf cavity from mCDW intrusion.
- The HSSW regime, north of the homogeneous water column, modifies the inflowing mCDW by cooling and adding salt to drive dense and cold water to be exported through the northern boundary.
- The mCDW regime with weak air/sea fluxes that are not able to drive dense water to the sea floor, results in a relatively warm and salty water mass (mCDW) flowing towards the ice shelf at depth, driving high ice shelf basal melting that contribute to the formation of a buoyant cold and fresh water mass at the surface that stratifies the water column and insulate the mCDW from the surface fluxes.
- The ice shelf basal melting in a mCDW regime is more sensitive to thermal driving than friction velocity compared to the HSSW regime.
- The location of the dynamical barrier in the HSSW regime is dependent on the strength of the surface heat and salt fluxes and acts as a thermodynamical barrier against warm mCDW intrusions.

Future work is necessary to evaluate the threshold between the two regimes and to understand how the HSSW regime can switch to the mCDW regime. Understanding this threshold is strongly related with recent studies that aim to understand how the heat from warm Circumpolar Deep Water north of the shelf break can flow onto the continental shelf and ultimately interact with the ice shelf. Klinck and Dinniman [2010] give a good review of the different physical processes responsible for the transport of CDW across the shelf break. More recently, other studies have shown the importance of eddies within the Antarctic Slope Current in transporting

heat across the shelf break [e.g. Nøst et al. 2011; St-Laurent et al. 2013; Hattermann et al. 2014; Stewart and Thompson 2015].

Chapter 4

Modelling ice shelf basal melting of the Mertz Glacier before and after a major calving event

4.1 Overview and chapter outlines

This chapter focuses on the Mertz region and the impact of the Mertz Glacier Tongue (MGT) calving event, that occurred in 2010, on the area-averaged basal melt rates from major ice shelves in the region. Ocean conditions underneath the ice shelves are examined with two numerical simulations being run, one for before the calving event (PRE) and the second after the calving event (POST). The simulations used a modified version of the Regional Ocean Modeling System (ROMS) [Shchepetkin and McWilliams 2005], similar to the version used in Chapter 2. This modelling study primarily focuses on the impact of the calving event on the meltwater production from the MGT, as well from the other major ice shelves included in the model domain. The regional ocean model used here includes ocean/ice shelf and frazil thermodynamics, tidal forcing and sub-ice shelf thermal and salinity exchange velocity coefficients which are determined by the local thermodynamics.

Before it calved, the MGT extended 150 km northward from the grounded ice sheet. After the calving event in 2010, the floating ice tongue was reduced to 80 km. The ice mask used in the simulations shows that the calving event led to a 40% decrease in the basal area of the glacier. Despite this decrease in available basal area, the simulations show an increase in basal melt rate (see Table 4.1), indicating that this major calving event changed the ocean conditions and the input of oceanic heat into

the ice shelf cavity. As described in Chapter 1, the Mertz region is a key source of Dense Shelf Water (DSW) that contributes to the formation of Antarctic Bottom Water (AABW) in the Australian-Antarctic basin [e.g. Rintoul 1998; Williams and Bindoff 2003; Williams et al. 2008; 2010]. Understanding the changes in ice shelf melting in the region is key to understanding changes in DSW production. This last point will be the main focus of the following chapter.

This chapter is structured as follows:

- Section 4.2 provides details of the two numerical simulations, the grid (bathymetry and ice geometry) and the changes relative to the model used in Chapter 2. In particular, the improved implementation of air/sea fluxes are described.
- Section 4.3 presents estimates of the area-averaged ice shelf basal melting of the major ice shelves in the region, as well as other ice masses (icebergs and fast ice) included in the domain between the PRE and POST MGT calving simulations.
- Section 4.4 discusses the association between the basal melt rate estimates and the ocean characteristics beneath the ice shelves.

4.2 Model development and forcing

The model setup used here is similar to the one described by Cougnon et al. [2013], and in Chapter 2, using the same horizontal and vertical grid. In this version, some modifications have been made to improve the vertical mixing scheme (B. Galton-Fenzi personal communication). Previously, the strong mixing induced by the intense latent heat polynya in winter, convected the entire water column in one time step. In this version of the model, the maximum convection depth of the surface oceanic boundary layer is kept to a minimum value in order to avoid mixing the entire water column in one time step, and is done using a maximum vertical mixing coefficient of 0.4 m^2 s^{-1}. In addition, one year in the model is equal to 364 days, this is to allow tidal forcing to be periodic in a year. Whereas previously in Chapter 2 realistic tidal predictions were used, following the same methods as in [Galton-Fenzi et al. 2012]. The tidal forcing used in the current chapter is detailed later in this section.

The bathymetry (Figure 4.1a) and ice draft (see Figure B.1 for more details) used in the pre-calving simulation (PRE) are the same as described in Chapter 2 [Cougnon et al. 2013], with the exception that the ice drafts of the Ninnis icebergs have been updated. The smaller Ninnis iceberg locked in the fast ice south of the B9B iceberg now has an ice draft of 500 m depth, and the larger Ninnis iceberg east of the MGT has an ice draft of 450 m (B. Legrésy personal communication). Previously a 200 m ice draft was used without changing the bathymetry underneath. The B9B iceberg has an ice draft of 300 m and is located between two relatively shallow banks, the Ninnis bank (∼200 m) and a shallow area southeast of the iceberg (∼200 m). The ice drafts of the three main ice shelves in the domain are shown in Figure 4.1, for the MGT (panel b), the Ninnis Ice Shelf (panel c) and the Cook Ice Shelf (panel d). Also, a minimum water column thickness of 20 m is kept beneath each ice shelf (and iceberg) to allow basal melt rate, so the iceberg in the model are not physically grounded but act as they were.

The bathymetry and ice draft used in the post-calving simulation (POST) also now have an improved iceberg configuration relative to Chapter 2. The position of the B9B and Ninnis icebergs have been determined using satellite imagery (mainly AQUA MODIS images provided by NASA) from the austral summer 2012-2013 [Lieser et al. 2013]. The images show that the B9B iceberg moved from east of the MGT to settle north of Commonwealth Bay (west of the MGT, see Figure

4.1a), during the austral summer of 2011 [Lacarra et al. 2014]. The smaller Ninnis iceberg, previously located in the fast ice north of the Ninnis Ice Shelf, has been located near the new Mertz Glacier front since the calving event occurred. The larger Ninnis iceberg broke apart and a smaller piece is now grounded near the Adélie sill.

A climatology of 'permanent' fast ice (between 2010 and 2012) updated from Fraser et al. [2012], is also included in the model. The fast ice in the model is set to have an ice draft of 10 m, except for the fast ice southeast of the MGT, which is set with an ice draft of 35 m. However, the icebergs and fast ice in the region have changed location since the simulations were run, and their current spatial distribution diverges from the geometry used in the POST simulation presented in this chapter. In December 2014, the small Ninnis iceberg moved from the Mertz ice front to the west of the Adélie depression, south of the other Ninnis iceberg and north of the B9B iceberg. This movement formed a barrier to the westward advection of sea-ice. Also, some fast ice southeast of the MGT broke apart and moved out of the domain. Subsequently in spring 2015, the B9B showed further signs of break-up.

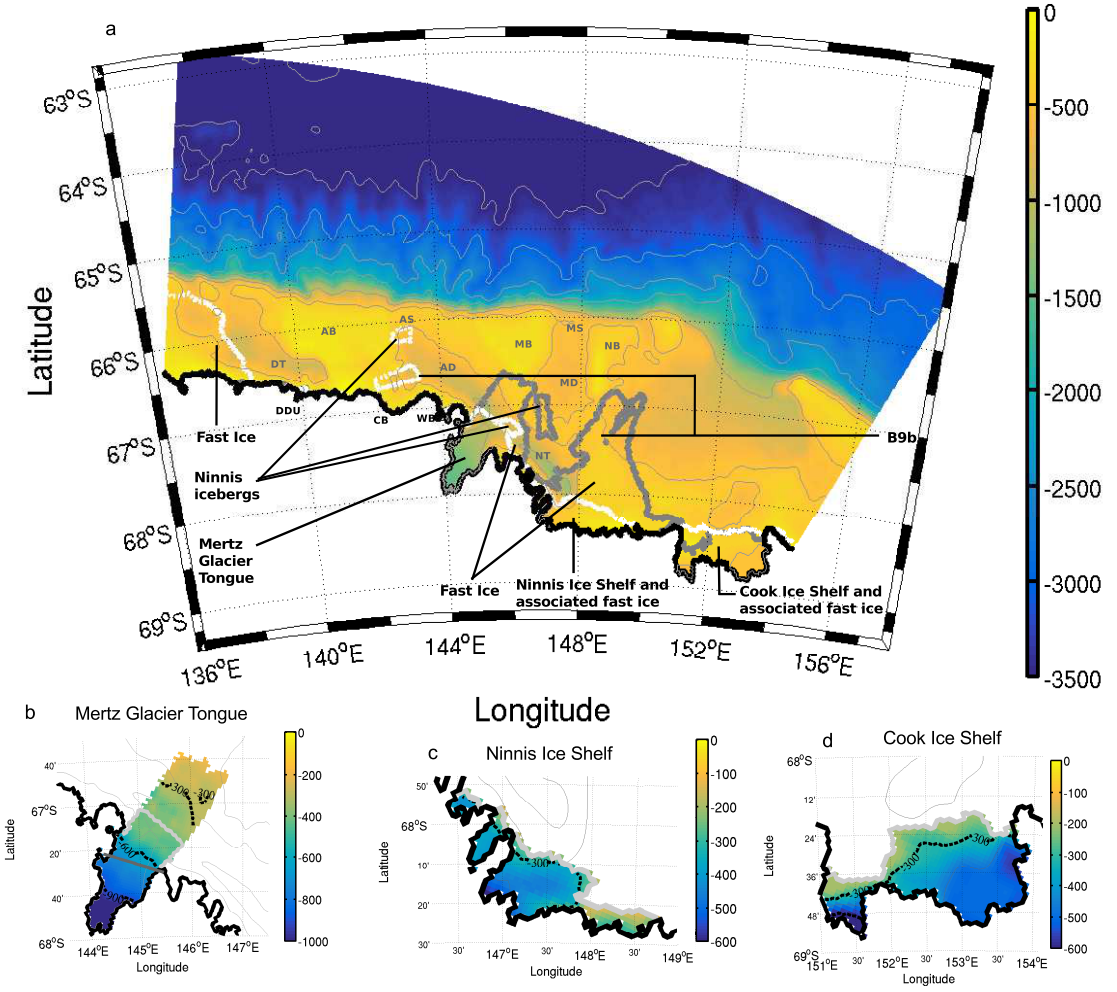

Figure 4.1: Bathymetry (in m) of the model (a) overlaid with the model ice mask contour (grey contours). Solid grey outline corresponds to the ice mask for the PRE simulation and the solid white outline corresponds to the ice mask for the POST simulation. The light grey contours are the bathymetry contours every 500 m on the continental shelf (until 1500 m) and every 1000 m for the deeper part of the model domain. Notable features are indicated on the bathymetry. In the ocean: AB: Adélie Bank; AD: Adélie Depression; AS: Adélie Sill; MB: Mertz Bank; MD: Mertz Depression; MS: Mertz Sill; NT: Ninnis Trough; DT: D'Urville Trough. Along the continent: Watt Bay (WB), Commonwealth Bay (CB), and Dumont D'Urville base (DDU). Bottom panels are the ice draft (in m) for the 3 main ice shelves in the domain, Mertz Ice Tongue (b), Ninnis (c) and Cook (d). Dashed line contours on b, c and d show the 300 m, 600 m and 900 m ice draft contours, the light grey outline is the ice mask post-calving. The dark grey line across the MGT cavity on panel b, shows the transect described in Section 4.4.

The model is forced at the surface with monthly data (adjusted for a 364 day-year)

using the year 2009 for the PRE simulation and 2012 for the POST simulation. Without a dynamic sea ice model, the fine-scale polynya activity is resolved by forcing the surface of the model with monthly heat and salt fluxes. These fluxes are based on sea ice concentration from a climatology derived model using Special Sensor Microwave Imager data (SSM/I – Tamura et al. [2011; 2016]) that is adjusted to a 364 day-year. Some modifications were needed to apply these air/sea forcing. In the previous simulation [Cougnon et al. 2013], at the onset of freezing conditions, the surface of the ocean was set to cool down and instantly become saltier at the same time (see Appendix A for more details). In addition, during summer the surface of the ocean was warming at temperatures higher than expected (up to approximately +8 °C). For the current simulations, the surface of the ocean is cooled to approximately the surface freezing temperature before to apply the salt flux at the surface of the ocean to simulate the brine rejection from the sea ice formation. During summer, the surface temperature is maintained to 0 °C maximum, which is a reasonable limit on the continental shelf according to the summer observations available in this region [Lacarra et al. 2011]. More details about these issues and the modifications are given in Appendix A.

The choice of the year 2009 for the PRE simulation forcing was made after analysing the monthly heat and salt fluxes that were averaged over the Mertz Glacier Polynya (MGP) area for the period 1992 to 2013 (see Figure B.3 for more details). The period from 2007 to 2009 was identified as a sustained period of relatively strong polynya activity with a winter average (May to September inclusive) of $\sim$ -164 W m^{-2}, while the average over the pre-calving period (1992-2009) was -159 $\pm$ 17 W m^{-2}. Similarly, the salt flux average for 2007 to 2009 was $\sim$ 0.82 kg m^{-2}, while the average for 1992 to 2009 was 0.82 $\pm$ 0.1 kg m^{-2}. As a result, 2007 to 2009 is considered as being a representative period for the pre-calving MGP region. Ultimately 2009, the year prior to the calving event, was chosen and a single year forcing was preferable to a pre-calving climatology, when compared to a single year forcing for the post-calving simulation restricted to one year forcing due to forcing availability. In the post-calving scenario, the year 2012 was chosen because of clear visibility of the permanent features situated in the region between 2010 and 2012 (A. Fraser personal communication). In summary, the results from these simulations are not restricted to the year chosen for the forcing, they can be compared with other years of similar salt and heat flux intensity.

Surface kinematic wind stress in the model is calculated using the 10 m surface

monthly wind record from ERA-interim product [Dee et al. 2011], that is adjusted to a 364 day-year for 2009 and 2012. The same lateral boundary forcing is used in both PRE and POST simulations. Lateral boundary fields, including potential temperature, salinity and horizontal velocities are relaxed to a climatology that is calculated from monthly fields from ECCO2 for the period 1992-2013 [Menemenlis et al. 2008; Wunsch et al. 2009] and are adjusted to 364 day-year. The model includes analytic tidal forcing at the lateral boundaries. The frequencies of the four main tidal constituents are adjusted to be periodic in 14 days, following the same design as Pingree and Griffiths [1981a;b]. A periodic tidal signal of 26 cycles for a 364 day-year in the model is implemented to facilitate the analyses. It is important to note that salinity values used in the model are on the Practical Salinity Scale (PSS78) and are dimensionless. The total run time of the model simulation was 33 years for each simulation. This 33 years run includes a spinup phase of 30 years to reach equilibrium, using a repeating loop of the climatology forcing. The last three years of the run are used for the analyses.

4.3 Basal melt rate

To simplify the analyses, the results shown in this chapter are averaged to obtain a 6-hourly climatology. As the model is forced by a constant and periodic tidal forcing of 26 cycles of 14 days per year, each time step of the three final years of high temporal resolution output (6-hourly data) can be averaged together. The area-averaged basal melt rate of each of the ice shelves (and other variables) are presented with a one year 6-hourly climatology.

4.3.1 Area-averaged melt rate

The total area of ice shelf available for melting in the model (including ice area from icebergs and fast ice) decreased by 19% between the PRE and the POST simulations (Table 4.2) with an increase in area-averaged melt rate by ∼7% (Table 4.1). Figure 4.2 shows the 6-hourly climatology for each simulation, with a filtered climatology where the tidal signal has been removed. The area-averaged melt rate seasonal cycle from all the ice in the model (including each ice shelves, icebergs and fast ice) nearly doubles during late summer (from day 25 to 75 which corresponds to mid-January till mid-March), and the melt rate variability increases due to the influence of tides (high variability) when the melt rate is high (Figure 4.2a).

Each major ice shelf in the model domain experiences changes in both basal melt rates and seasonal pattern of melt. For the MGT, the PRE simulation indicates a basal melting of 0.9 ± 0.2 m yr^{-1} (5.6 ± 1 Gt yr^{-1}) and the POST simulation indicates a basal melting of 1.7 ± 0.1 m yr^{-1} (6.0 ± 0.4 Gt yr^{-1}). The Mertz ice shelf basal area decreased by 42%, coinciding with an increase of 89% in the area-averaged melt rate (and a mass loss increase of 7%). Furthermore, the maximum melting during the POST simulation correlates with the minimum melting during the PRE simulation that occurs in winter (around day 150 and 230 – Figure 4.2b).

In Table 4.1 the standard deviation is calculated for the 6-hourly climatology, as well as for the filtered climatology (value in squared-brackets). Both standard deviations show how the seasonal pattern of melt is important compared to the tidal signal on the melt rate. For the Mertz Glacier case, the standard deviation for the PRE simulation with the non-filtered climatology is greater (0.2 m yr^{-1}) than for the filtered climatology (0.1 m yr^{-1}), illustrating that the tidal signal has more influence than the seasonal signal on the Mertz Glacier basal melt rate. On the other hand,

for the POST simulation, both standard deviations for the Mertz Glacier average basal melt rate are equal, illustrating that the seasonal signal has a similar impact than the tidal signal on the ice shelf basal melt rate. The root-mean-square (RMS) of the depth averaged velocity calculated beneath the MGT, illustrates that the tidal velocities are more important in the PRE simulation (8.6×10^{-4} m s^{-1}) than the POST simulation (8.4×10^{-5} m s^{-1}).

Similar changes in the melt rate and seasonal pattern of melt (Figure 4.2c) are observed for the Ninnis Ice Shelf (directly east of the Mertz Glacier). The proximity of the Ninnis Ice Shelf with the Mertz Glacier may explain the similarities in melt rate between them. The area-averaged melt rate of the Ninnis Ice Shelf doubled, from 0.4 ± 0.2 m yr^{-1} to 0.8 ± 0.3 m yr^{-1} with no change in the area of the ice shelf. In contrast, the area-averaged basal melt of the Cook Ice Shelf in the eastern side of the domain decreased by about a third between the PRE and the POST simulation, from 1.9 ± 0.3 m yr^{-1} to 1.2 ± 0.3 m yr^{-1}. However, the seasonal signal pattern did not change, even when the melt rate decreased (Figure 4.2d).

The standard deviation of the filtered and non-filtered data for both the Ninnis and the Cook ice shelves are the same, illustrating that the seasonal cycle and the tidal signal have a similar impact on the basal melt rate. Also, the RMS of the depth averaged velocity calculated beneath the Ninnis, 4.5×10^{-5} m s^{-1} for the PRE and 5.3×10^{-5} m s^{-1} for the POST simulation, illustrate a negligible influence of the tides within the Ninnis embayment. On the other hand, beneath the Cook ice shelf, the RMS is greater than beneath the Ninnis (1.8×10^{-4} m s^{-1} for both simulation) but lower than beneath the MGT pre-calving, likely because the Cook ice shelf is located within an embayment, while the MGT pre-calving has most of its ice shelf outside the embayment.

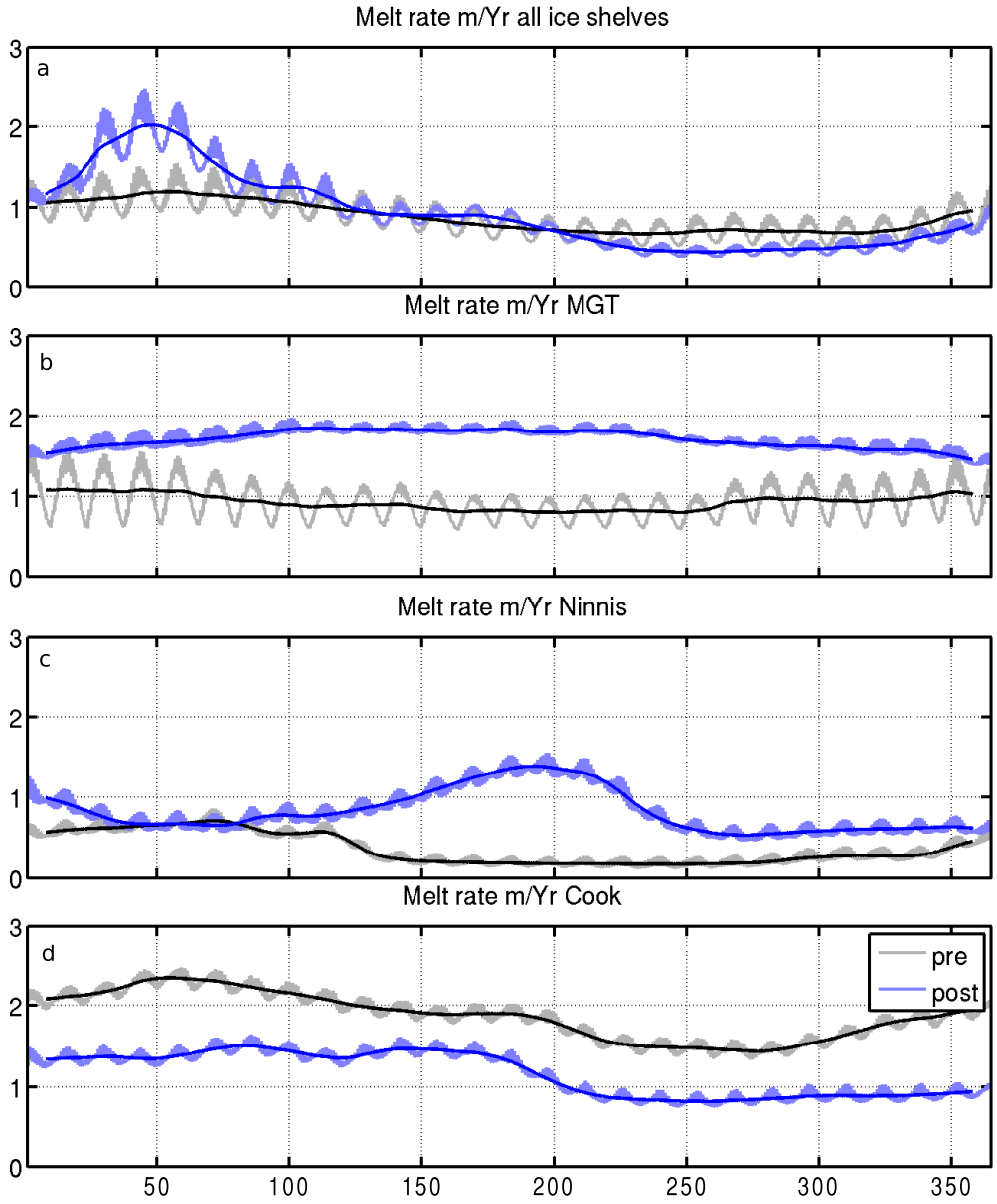

Figure 4.2: Area-averaged melt rate (m yr^{-1}) for the 6-hourly one year climatology of the three final years of each simulation (grey for the PRE simulation and light blue for the POST). A low pass filter, with a window span of 14 days is applied to remove the tidal signal and is represented by the black line for the PRE simulation and blue line for the POST simulation. The x-axis is in day of the year from day 1 to day 364. Results are shown for a) the entire ice area in the model, b) the Mertz Glacier, c) the Ninnis Ice Shelf, and d) the Cook Ice Shelf.

Table 4.1: Area-averaged basal melt rate (m yr^{-1}) from the non-filtered climatology. The values in squared-brackets are the standard deviations applied to the filtered climatology.
* *All ice in the model including ice shelves, icebergs and fast ice.*
** *Other ice refers to icebergs and minor ice shelves in the domain.*

Ice Shelf	PRE (m y^{-1})	POST (m y^{-1})	% melt change
Total *	0.88 ± 0.23 [0.18]	0.94 ± 0.48 [0.47]	+7
Mertz	0.9 ± 0.2 [0.1]	1.7 ± 0.1 [0.1]	+89
Ninnis	0.4 ± 0.2 [0.2]	0.8 ± 0.3 [0.3]	+100
Cook	1.9 ± 0.3 [0.3]	1.2 ± 0.3 [0.3]	-37
Fast ice (10m)	0.3 ± 0.2 [0.2]	0.6 ± 0.9 [0.9]	+133
Fast ice (35m)	0.2 ± 0.3 [0.3]	0.5 ± 0.7 [0.7]	+67
Other ice**	1.5 ± 0.5 [0.3]	0.8 ± 0.3 [0.1]	-47
Mertz:			
M < -900m	3.24 ± 0.04 [0.03]	5.1 ± 0.1 [0.4]	+57
-900 < M < -600m	0.56 ± 0.04 [0.03]	1.09 ± 0.09 [0.08]	+95
-600 < M < -300m	0.47 ± 0.2 [0.05]	0.70 ± 0.1 [0.08]	+49
M > -300m	1.1 ± 0.7 [0.5]	0.6 ± 0.3 [0.2]	-42

4.3.2 Spatial melting distribution

The difference in averaged spatial melting (POST minus PRE simulation) for the ice present in both simulations is shown in Figure 4.3. The three main ice shelves show different patterns in melting over their ice shelf area. The scatter grid cell scale noise effect on the melt rate near the grounding line (Figure 4.3) results in some numerical artefacts in the horizontal velocity field, due to a thin water column thickness (20 m minimum). As described by Adcroft et al. [1999] and Losch [2008], the horizontal velocity field on a C-grid model [Arakawa and Lamb 1977] such as the one used by ROMS, that does not resolve the Rossby radius, can allow a standing grid-scale noise near topography (beneath an ice shelf for instance). However, this noise is not important for the results presented in this study, as the focus is on the melt rate average for each ice shelf (wider spatial scale).

The Mertz Glacier is different from the Ninnis and the Cook ice shelves because of its geometry. Most of the Mertz Glacier is confined within a narrow embayment. The glacier has a thick ice draft (1600 m thick near the grounding line) and water

Table 4.2: Rate of mass loss (Gt yr^{-1}) from the non-filtered climatology. The values in squared-brackets are the standard deviations applied to the filtered climatology.
* *All ice shelves in the model including icebergs and fast ice.*
** *Other ice refers to icebergs and minor ice shelves in the domain.*

Ice Shelf	PRE (Gt y^{-1})	POST (Gt y^{-1})	% mass loss change	% area change
Total *	23.7 ± 6.1 [4.8]	20.8 ± 10.5 [10.3]	-14	-19
Mertz	5.6 ± 1 [0.6]	6.0 ± 0.4 [0.4]	+7	-42
Ninnis	0.6 ± 0.3 [0.3]	1.3 ± 0.4 [0.4]	+117	0
Cook	7.3 ± 1.1 [1.1]	4.5 ± 1.0 [1.0]	-38	0
Fast ice (10m)	3.4 ± 2.1 [2.1]	6.6 ± 9.2 [9.1]	+94	+3
Fast ice (35m)	0.3 ± 0.4 [0.3]	0.2 ± 0.3 [0.2]	-33	-65
Other ice**	6.5 ± 2.2 [1.2]	1.8 ± 0.6 [0.3]	-72	-49
Mertz:				
M < -900m	2.16 ± 0.03 [0.02]	3.4 ± 0.2 [0.2]	+57	0
-900 < M < -600m	0.86 ± 0.06 [0.05]	1.7 ± 0.1 [0.1]	+98	0
-600 < M < -300m	1.2 ± 0.5 [0.1]	0.89 ± 0.2 [0.08]	-26	-50
M > -300m	1.4 ± 0.9 [0.6]	0.009 ± 0.005 [0.003]	-99	-99

column thickness is of 400 to 500 m for most of the ice shelf and 20 m near the grounding line (see Figure B.2 for more details). In comparison to this, the Ninnis and the Cook ice shelves have wider embayments, with shallower ice draft (600 m maximum at the grounding lines) and shallower water column thicknesses (20 m over most of the ice shelf areas). The basal melt rate of the Ninnis Ice Shelf increases homogeneously over the ice shelf basal area for the POST simulation. The Cook Ice Shelf basal melting decreases over the entire ice shelf, except near the eastern grounding line area, where there is almost no melting.

The Mertz Glacier is the key ice shelf in the model domain and shows an irregular spatial melt pattern over the area common to both simulations. A strong increase in melting does not occur at the grounding line, but rather near the narrowest point of the embayment, north of the grounding line, while a decrease in melting is seen at the north west corner of the embayment. A closer look at the Mertz Glacier is given in Figure 4.4, which show the area-averaged melt rate for four specific areas of the glacier, following the ice draft contours (Figure 4.1b). Two areas are chosen for the embayed ice shelf, focusing on ice with a draft of 600 m to 900 m and ice

with a draft thicker than 900 m (i.e. ice near the grounding line). Two other areas are chosen outside of the embayment, one with an ice draft of 300 m to 600 m and the other with an ice draft shallower than 300 m. Most of the Mertz basal melting occurs near the grounding line with nearly 40% of the PRE melting occurring below 900 m, increasing to 54% for the POST simulation.

The different selected areas of the Mertz Glacier show different temporal patterns of basal melting. The areas of the Mertz Glacier located outside of the embayment show a stronger variability in the melt rate pattern due to tides (Figure 4.4b and c). The seasonal signal is mainly seen for the ice shallower than 300 m for the PRE simulation, and the RMS of the depth averaged velocity calculated beneath the ice of the same order of magnitude (6.3×10^{-4} m s^{-1}) than the RMS calculated over the entire pre-calving MGT (8.6×10^{-4} m s^{-1}). Note that there is almost no ice draft shallower than 300 m depth for the POST simulation (only a few cells in the model), which explains the negligible mass loss in Table 4.2 and in Figure 4.4c.

The embayed ice shelf shows less melt rate variability due to tidal or seasonal forcing. For the PRE simulation, the ice in the cavity is isolated from significant external seasonal and tidal variability (Figure 4.4d and e). The melt rate pattern is fairly constant with an area-averaged melt rate of 3.24 ± 0.04 m yr^{-1} for the ice deeper than 900 m. The weak standard deviation in the non-filtered data ($\pm$ 0.04 m yr^{-1}) associated with a RMS of 4.3×10^{-6} m s^{-1}, indicate a negligible tidal and seasonal variability in the cavity (embayed area) for the PRE simulation. These results illustrate that the ice shelf in the embayment is isolated from the variability (tidal and seasonal) of the far field ocean.

In contrast, the melt rate of the Mertz Glacier in the cavity during the POST simulation shows a stronger seasonal variability, with an area-averaged melt rate of 5.1 ± 0.1 m yr^{-1} and a maximum melt rate in late autumn (at approximately day 100 to 170). It is also important to note that for the deeper ice, the standard deviation from the filtered climatology is greater than the standard deviation from the climatoliogy for the POST simulation, indicating that the seasonal variability is more important than the tidal signal to the ice shelf basal melt rate after the calving event. Also, the RMS for the ice deeper than 900 m is weak (5.3×10^{-6} m s^{-1}) illustrating a negligible impact from the tides.

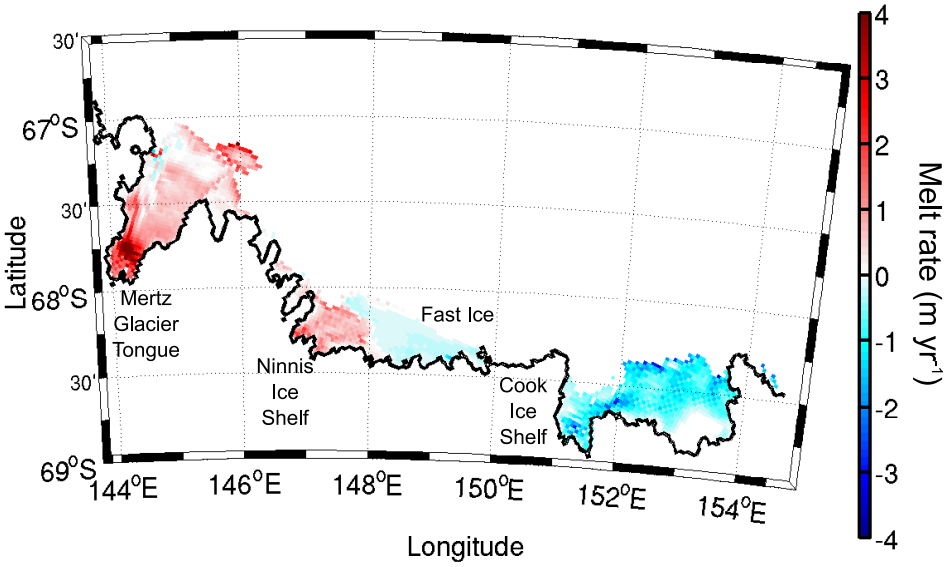

Figure 4.3: Time averaged spatial melt rate difference in m yr^{-1} between the POST and the PRE simulations for the 3 main ice shelves and the fast ice common to both simulations in the domain.

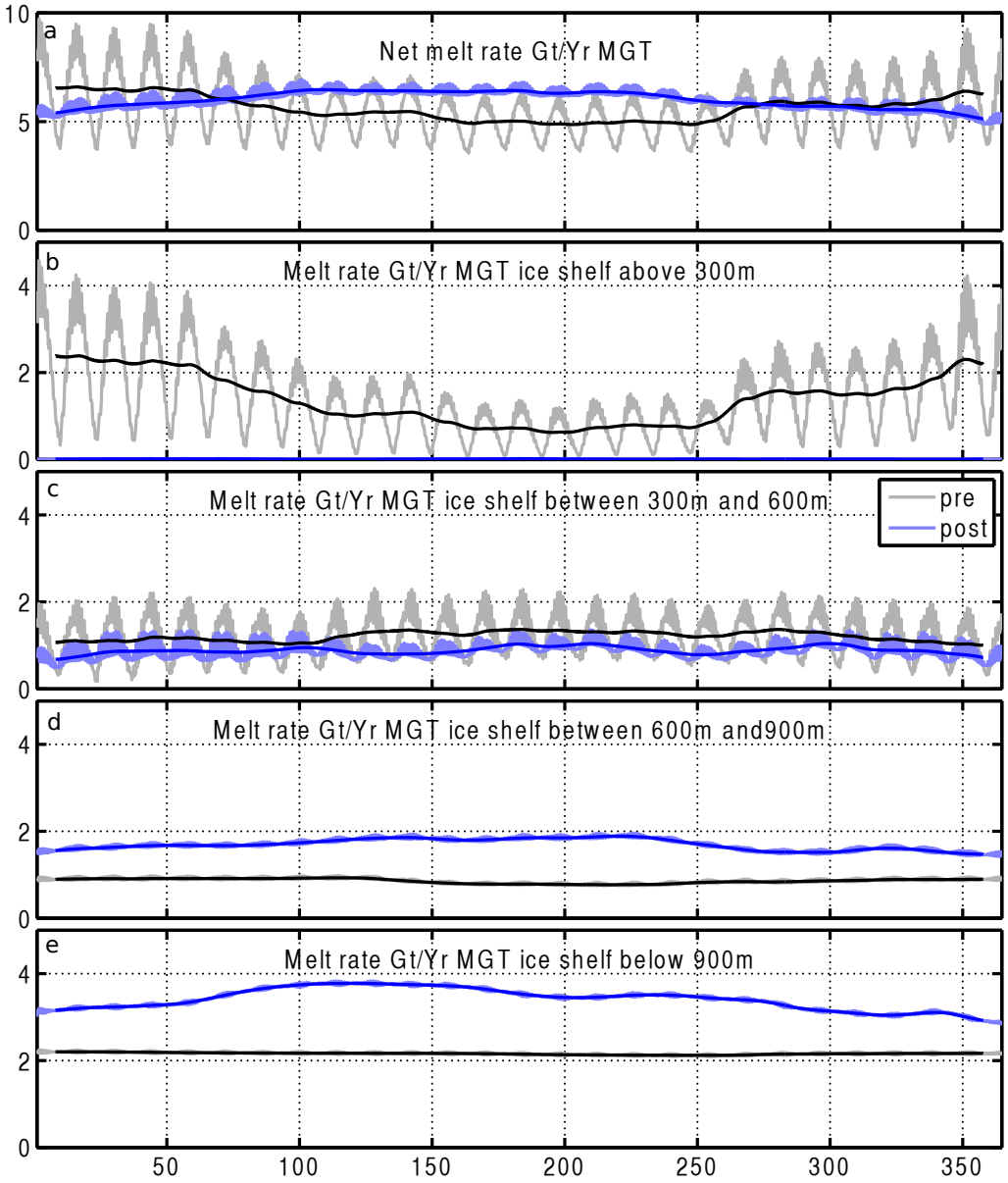

Figure 4.4: Rate of mass loss (Gt yr^{-1}) for the 6-hourly climatology overlaid with the filtered data for each simulation. The x-axis is in days of the year from day 1 to day 364. Results are shown for a) the entire Mertz Glacier, b) for the ice located above 300 m depth, c) located between 300 and 600 m depth, d) located between 600 and 900 m depth and e) below 900 m depth. For the PRE simulation (grey and black lines) and the POST simulation (blue).

4.3.3 Comparison with other studies

In the earlier simulation presented in Chapter 2 [Cougnon et al. 2013], an area-averaged melt rate of 1.9 ± 1.4 m yr^{-1} produced a mass loss of 11.4 ± 8.4 Gt yr^{-1}

for the entire Mertz ice tongue. This earlier simulation ran for a period of 16 years (1992-2007), including inter-annual variability within the external forcing. This inter-annual variability is also observed in the melt rate estimates, that includes a 3 to 4 year period of more intense melting (2000-2003). The intense melting from this earlier study is related to the interannual variability of the air/sea forcing.

The value of mass loss estimated in Cougnon et al. [2013] for deep ice (below 900 m) during a sustained period of weak polynya activity ($\sim$ 4.9 Gt yr^{-1}) is comparable with the POST simulation here. Similarly, mass loss estimated for deep ice during a period of mean to strong polynya activity ($\sim$ 2.4 Gt yr^{-1}) is comparable to the PRE simulation here. Observational estimates of melt rates, from flux gate calculations close to the Mertz Glacier grounding line, vary from 11 m yr^{-1} [Berthier et al. 2003] to 18 m yr^{-1}[Rignot 2002] at the grounding line. These observed estimations are much greater than what is estimated by the model, which is $\sim$ 3.24 m yr^{-1} pre-calving and $\sim$ 5.1 m yr^{-1} post-calving, suggesting that the model is under-estimating the basal melting near the grounding line.

More recent studies, focused on the global Antarctic mass loss, have estimated melt rate for the Cook, Ninnis and Mertz ice shelves. Rignot et al. [2013] use a comparison between the volume flux divergence of Antarctic ice shelves, the surface accumulation and the thinning of the ice shelves to estimate an area-averaged melt rate of 1.4 $\pm$ 0.6 m yr^{-1} for the Mertz Glacier (pre-calving), 1.2 $\pm$ 2 m yr^{-1} for the Ninnis Ice Shelf and 1.3 $\pm$ 1 m yr^{-1} for the Cook Ice Shelf. Depoorter et al. [2013] use a different method that includes a calving flux to estimate the basal mass balance. They estimate a melt rate of 0.87 $\pm$ 0.79 m yr^{-1} for the Mertz Glacier (pre-calving), 0.16 $\pm$ 2.28 m yr^{-1} for the Ninnis Ice Shelf and 0.92 $\pm$ 2.08 m yr^{-1} for the Cook Ice Shelf. These values are closer to the melt rates estimated here.

Other studies estimate thickness changes around the Antarctic continent using satellite data (e.g. Pritchard et al. [2012]; Paolo et al. [2015]). However, these studies are too recent to estimate major changes of the Mertz Glacier as a result of the calving event. Also, the Cook and Ninnis ice shelves are poorly resolved by satellite imagery. In Paolo et al. [2015] only 55% of the area of the post-calving Mertz Glacier total area is surveyed, and only 35% of the Cook Ice Shelf is surveyed. Also, Paolo et al. [2015] estimate a nil rate of thickness-change from 1994 to 2012 for both the Mertz and the Cook ice shelves. Pritchard et al. [2012] estimate a light gain in thickness-change for the shorter period 2003 to 2008, of about 1.1 m yr^{-1} for the

Cook Ice Shelf and about 0.3 m yr^{-1} for the Mertz Glacier (pre-calving). Future satellite studies looking at thickness-change on a longer time-scale after the calving event should show a decrease in the Mertz Glacier melt rate if the model trend is correct. The strong increase in mass loss seen in the model (+57% for the deeper ice and +98% for the ice with an ice draft between 600 m and 900 m) should result in a notable decrease in the surface height of the Mertz Glacier.

Many studies have shown that tides have an important impact on melting and freezing (eg: Makinson et al. [2011]; Mueller et al. [2012]; Gwyther et al. [2016]). In this study, the impact of the tides is seen in the variability of the basal melt rate signal, mainly impacting the shallower region of the ice shelf that extends beyond the coastal embayments. Also, there is greater variability in basal melting when there is higher melt rates, due to tidal forcing, as seen in Figure 4.2a in summer (at around day 50).

4.4 Ocean state beneath the ice shelves

4.4.1 Ocean circulation within the Mertz Glacier cavity

An examination of the vertically integrated horizontal velocity field beneath the Mertz Glacier for the PRE and POST simulations (Figure 4.5a and b) is used to understand the interactions between the ocean and the base of the Mertz Glacier. The ocean circulation in both simulations within the Mertz cavity is very similar, with a clockwise flow exiting along the western edge of the cavity. This clockwise circulation does not reach the grounding line at about 67.9 °S but instead is recirculated at about 67.6 °S. In addition, the magnitude of the depth averaged velocity is weak (in the order of 1 cm s^{-1}) in both simulations, with a slightly stronger magnitude for the POST simulation (red arrows in Figure 4.5a and b). The increase in melt rate drives a stronger outflow along the western edge of the cavity, strengthening the buoyancy-driven circulation and driving a stronger inflow along the eastern edge of the cavity.

The section across the Mertz cavity (shown in Figure 4.5a and b, yellow dashed line) illustrates that the POST simulation is warmer by 0.19 ± 0.02 °C along the section (Figure 4.6a and b, and Table 4.3). A maximum warming of +0.37 °C is seen within the outflowing water mass along the western edge of the cavity. Along the same section, the POST simulation is fresher by 0.105 ± 0.005 with a maximum freshening

of 0.22 seen at the sea floor (Figure 4.6c and d, and Table 4.3). The warming and freshening of the section result in a decrease in potential density (contour lines on Figure 4.6c and d) by 0.091 ± 0.004 kg m^{-3}. During the POST simulation, the potential density is more homogeneous in the interior of the cavity than during the PRE simulation.

The velocity field across the section (contour lines on Figure 4.6a and b) illustrates the intensity of the clockwise circulation observed with the vertically integrated horizontal velocity field (Figure 4.5a and b). The outward flow (flowing out of the cavity – solid contours on Figure 4.6a and b) is associated with a water mass that is fresh and below the surface freezing temperature, which originates from the melting of the ice shelf (Ice Shelf Water – ISW) for both simulations. On the other hand, the inward flow (flowing into the cavity – dashed line contours on Figure 4.6a and b) is associated with relatively warm water, in particular for the POST simulation. During the PRE simulation the main water mass flowing into the Mertz cavity originates from the Adélie depression, predominantly during winter (Figure 4.5a). In the POST simulation the main flow going into the Mertz cavity originates from different sources, the Adélie depression and the area north of the Ninnis trough. During the POST simulation, a "hotspot" of warming is located near the bottom of the cavity, on the eastern side of the section where warmer water from the Ninnis trough flows into the cavity.

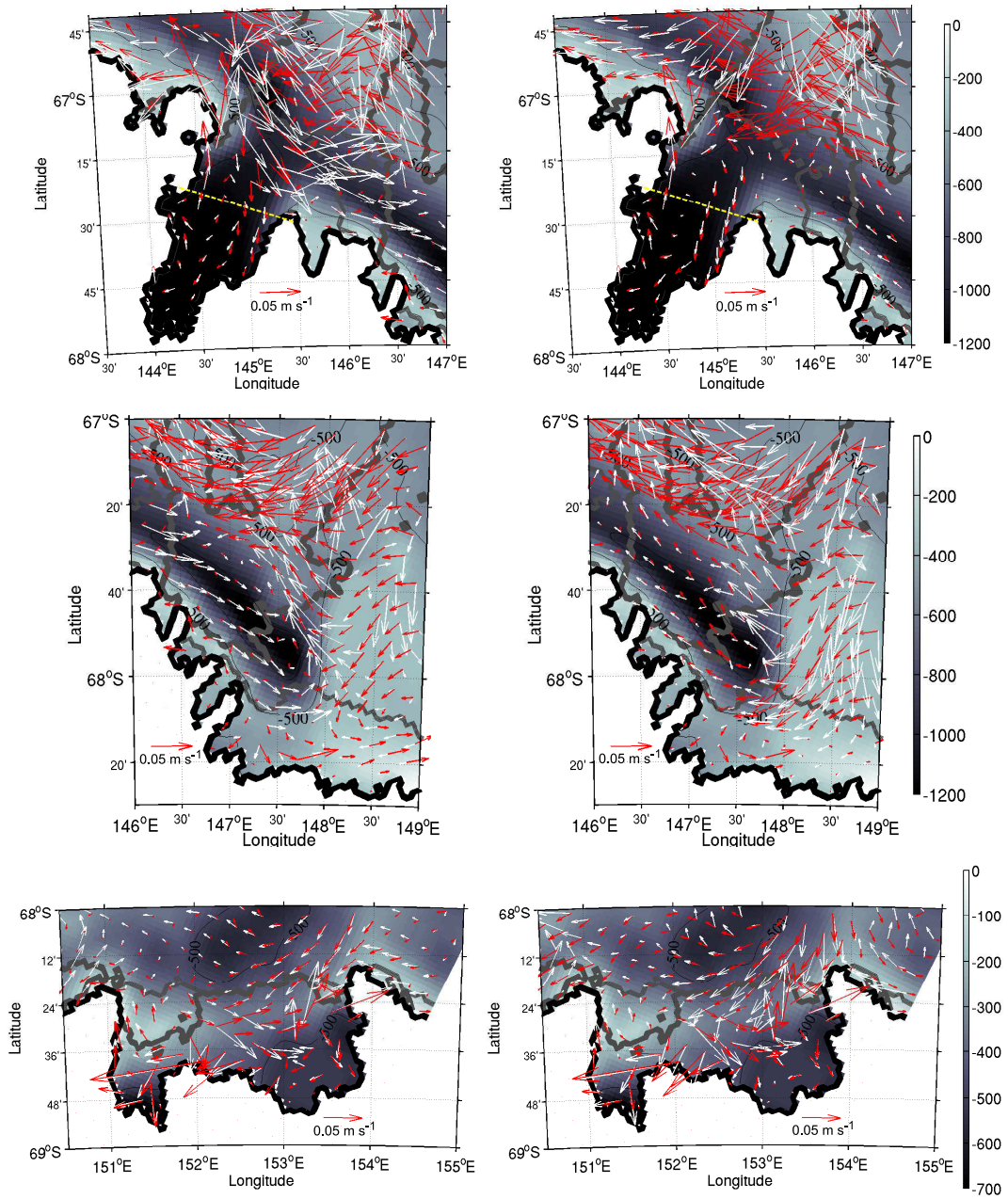

Figure 4.5: Vertically integrated horizontal velocity field (m s^{-1}) for the Mertz Glacier area (a and b), the Ninnis Ice Shelf (c and d) and the Cook Ice Shelf (e and f). Averaged over winter (a, c and e – July-August-September) and averaged over summer (b, d and f – December-January-February) in m s^{-1} for PRE (white arrows) and POST (red arrows) simulations. The grey bold lines are the ice mask outline for the PRE and POST ice mask and the background is the bathymetry (in m) with few contours outline on each panel. The yellow dashed line on panel a and b is the section across the cavity discussed in the text. The unit vector at the bottom of each panel corresponds to 0.05 m s^{-1}

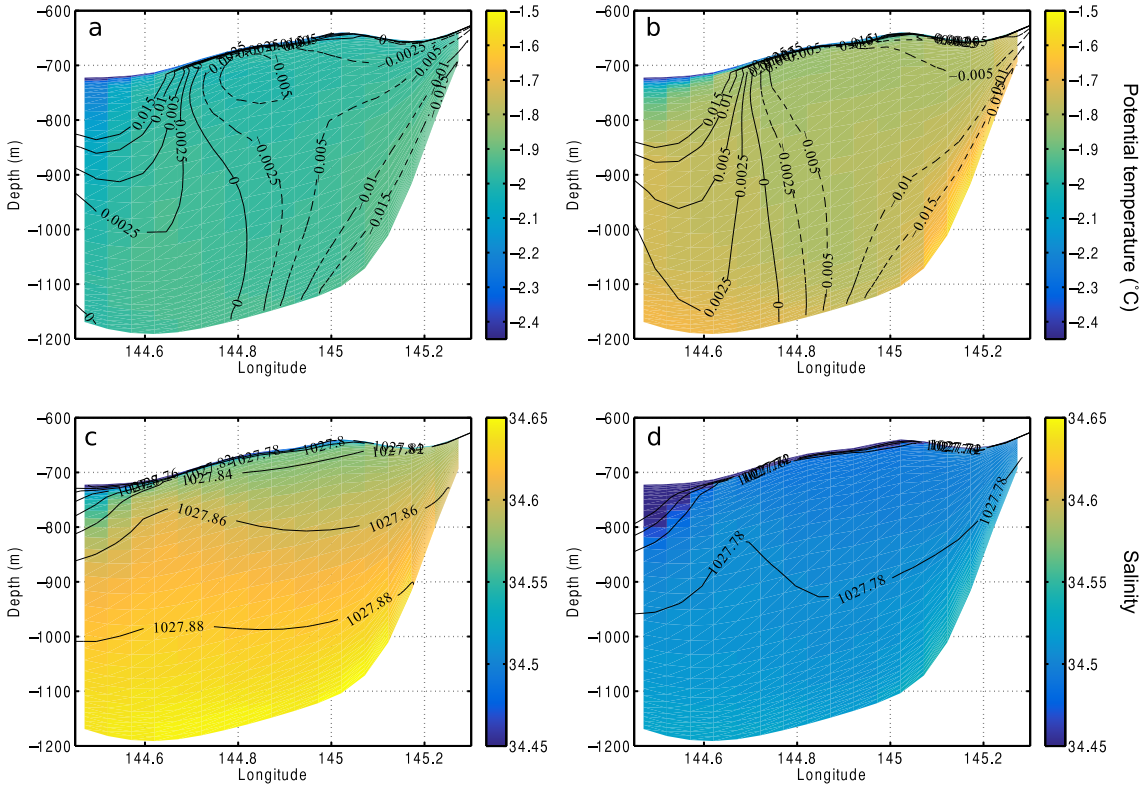

Figure 4.6: Time averaged potential temperature (°C) overlaid with contours of the velocity (m s^{-1}) perpendicular to the section (a and b) and time averaged salinity overlaid with the potential density (kg m^{-3}) contours (c and d) for the PRE (a and c) and POST (b and d) simulations along the section shown on Figure 4.1b.

Potential Temperature - Salinity ($\Theta - S$) diagrams (Figure 4.7) illustrate the shift in potential temperature and salinity discussed previously along the transect across the Mertz cavity. The exported water flowing out of the cavity (in red) is colder and fresher (less dense) than the incoming water flowing into the cavity (in blue), illustrating the impact of additional glacial meltwater on the water masses flowing within the cavity. The inclined dashed line on each panel of Figure 4.7 illustrates the changes in potential temperature and salinity due to the ice shelf melting. Given the expected potential temperature and salinity of the water mass responsible for the melting of an ice shelf, a linear profile can be defined using under ice thermodynamics following Gade [1979], as used in Chapter 3.

In the PRE simulation, ISW fills the entire cavity (Figure 4.7a). Only the upper part of the water column (top layers directly underneath the ice shelf) is considered as ISW in the POST simulation, with a thicker ISW layer on the western side of the

Table 4.3: Time averaged potential temperature (°C), salinity, potential density (kg m^{-3}), velocity (m s^{-1}) transport (Sv : $\times 10^6$ m^3 s^{-1}) and area (km^2) on the inflow and the outflow across the transect (shown on Figure 4.1b), for the PRE and POST simulations, as well as their differences.

	PRE	POST	POST - PRE
$\bar{\theta}$	-1.99 ± 0.04	-1.79 ± 0.05	+0.19 ± 0.02
θ_{max}	-1.92	-1.56	+0.36
θ_{min}	-2.46	-2.43	+0.03
$\bar{S}$	34.60 ± 0.01	34.49 ± 0.02	-0.105 ± 0.005
S_{max}	34.65	34.54	-0.11
S_{min}	34.42	34.23	-0.19
$\bar{\rho}$	1027.86 ± 0.01	1027.77 ± 0.02	-0.091 ± 0.004
ρ_{max}	1027.90	1027.80	-0.1
ρ_{min}	1027.72	1027.57	-0.15
$\bar{V}_{in}$	-0.006 ± 0.003	-0.007 ± 0.003	+17%
$\mid V_{in(max)} \mid$	0.028	0.028	0%
$\bar{V}_{out}$	0.007 ± 0.008	0.01 ± 0.01	+25%
$\mid V_{out(max)} \mid$	0.077	0.11	+43%
Transport_{in}	-0.06 ± 0.03	-0.08 ± 0.04	+33%
Transport_{out}	0.06 ± 0.02	0.08 ± 0.03	+33%
Area of inflow	9.37×10^3	9.78×10^3	+4.4%
Area of outflow	6.89×10^3	6.49×10^3	-5.9%

cavity associated with the greater outward velocity (Figure 4.6d and Figure 4.7b). The transport through the section (colour map on Figure 4.7) also illustrates the intensification of the ocean circulation in the POST simulation. The transport inflow and outflow are of ∼0.06 Sv for the PRE simulation across the section, with both increasing by about 33% in the POST simulation (Table 4.3). The increase in the inflow can be explained by velocity increases of only 17% and increases of 4.4% in the area of the inflow. Alternatively, the area of the outflow decreased during the POST simulation by 5.9%, with an increase of the outflow velocity by $\sim$ 25%. These differences can explain the increase of the outflow transport. During the POST simulation, a warmer water mass (+0.19 °C) is responsible for the basal melting of the ice shelf (inclined dashed line on Figure 4.7b) associated with a stronger ocean circulation and transport within the cavity (Table 4.3).

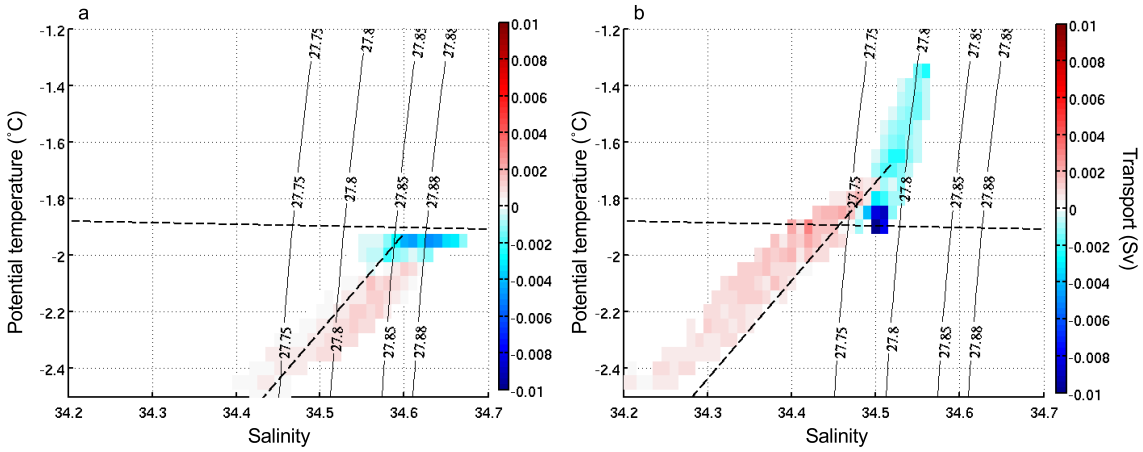

Figure 4.7: Potential Temperature (°C) - Salinity (θ-S) diagrams averaged for the section (red dashed line on Figure 4.5a and b) for PRE (a) and POST (b) simulations. The colour bar is the transport in Sv (10^6 m^3 s^{-1}). Negative (blue) is a flow going into the cavity and positive (red) is a flow going out of the cavity. The horizontal dashed line corresponds to the surface freezing point and the inclined dashed lines on the data correspond to an example of a Gade Line [Gade 1979]. Some reference potential density (-1000 kg m^{-3}) contours have been added to the figure.

4.4.2 Velocity within the Ninnis and Cook Ice Shelf cavities

Further analyses of the vertically integrated horizontal velocity field (Figure 4.5c and d) near the Ninnis Ice Shelf indicates that a change in the ocean circulation north of the Ninnis Ice Shelf drives stronger currents beneath the ice shelf. This change in velocity between the simulations is likely due to the major differences in the icescape between the two simulations. Most of the fast ice that is attached to the Ninnis Ice Shelf in the PRE simulation is not present in the POST simulations. Similarly, the icebergs north of the Ninnis Ice Shelf (B9B and Ninnis icebergs) are not present in the POST simulation changing the ocean circulation in the area.

For the PRE simulation (white arrows on Figure 4.5c and d), the main flow reaching the area of the Ninnis Ice Shelf in winter (Figure 4.5c) comes from the MGT/Adélie depression area and flows northward without strong interactions with the ice shelf. This lack of interaction may explain the low melt rates estimated in the previous section. In summer (Figure 4.5d), the main flow reaching the area comes from north of the Ninnis Ice Shelf in the PRE simulation and circulates westward within and north of the Ninnis trough. During the POST simulation, the winter and summer velocity fields are very similar to the summer velocity field of the PRE simulation.

A southward flow coming from north of the Ninnis Ice Shelf flows beneath the ice shelf to drive a uniform increase in melt rate over the ice shelf (Figure 4.3).

The Cook Ice Shelf is different from the Mertz Glacier and the Ninnis Ice Shelf, due to its location at the eastern boundary of the domain. However, the lateral boundary forcing is the same in both simulations, so any changes observed near the Cook Ice Shelf are the result of changes in the air/sea forcing and changes in the icescape further west of the Cook Ice Shelf. The velocity fields around the Cook Ice Shelf (Figure 4.5e and f) do not indicate any major changes in velocity magnitude or direction. The vertically integrated horizontal velocity field indicates a small decrease in the magnitude of the current at the eastern side of the ice shelf in winter (Figure 4.5e) with a slight change of direction (more southwestward) for the POST simulation (red arrows on Figure 4.5f).

The greatest changes in velocity are located beneath the northern part of the ice shelf. During the POST simulation, near the front of the ice shelf, there is a shift in the POST simulation vectors in winter (Figure 4.5e). The southward flow recirculates northward further north in the POST simulation than for the PRE simulation. As a result, less water circulates within the cavity, which may explain the decrease in melt rate described in the previous section (Figure 4.3). As for the Ninnis cavity, it is important to note that most of the water column thickness within the Cook cavity is only 20 m thick (Figure B.2 for more details).

4.4.3 Thermal forcing

Another way to estimate the impact of a change in ocean properties on the ice shelf and its melting is to investigate variability of the two major components of the model melt rate parametrisation, the friction velocity and the thermal forcing at the base of each ice shelf. It is known that friction velocity plays an important role in the spatial distribution of the ice shelf basal melt rate [e.g. Mueller et al. 2012; Gwyther et al. 2015]. Here, the friction velocity is calculated using the dimensionless drag coefficient ($Cd = 0.005$), that is spatially constant over the entire ice shelf and the modelled velocity (m s^{-1}) of the top layer that is beneath the ice shelf (U_{top}): $u_* = \sqrt{Cd} \times U_{top}$.

Different definitions of thermal forcing have been used within the literature, depending whether observations or numerical simulations are used for analysis. In

general, observations will use the closest measurement from the ice shelf depending on the observations available. For instance, Rignot and Jacobs [2002] use the closest observed *in-situ* ocean temperature from each ice shelf and compare it with the freezing temperature at the depth of $0.88H_{GL}$ (H_{GL} is the grounding line depth). Dansereau et al. [2013] and Gwyther et al. [2016] use the difference between the *in-situ* temperature beneath the ice shelf and the *in-situ* freezing temperature that varies with pressure in their numerical models. These are examples of models that estimate the impact of the thermal forcing on ice shelf melting.

In this study, the 'thermal forcing' (ΔT) is calculated in two different ways to investigate the potential of the top layer of the model beneath the ice shelf to drive melting, as well as the potential of the water column underneath the ice shelf to contribute to the melting. 'Thermal forcing' due to the ocean layer immediately beneath the ice shelf is investigated and is defined as follows: $\Delta T_N = T_{N(in-situ)} - T_{f(IS_{base})}$, where $T_{N(in-situ)}$ is the *in-situ* ocean temperature averaged along the top layer of the water column below the ice shelf, and $T_{f(IS_{base})}$ the averaged *in-situ* freezing temperature at the base of the ice shelf averaged for the same area as $T_{N(in-situ)}$.

Similarly, 'thermal forcing' due to the ability of the ocean within the ice shelf cavity to contribute to the basal melting is investigated and is defined as follow: $\Delta T_V = T_{V(in-situ)} - T_{f(IS_{base})}$, where ΔT_V is the difference between the volume averaged *in-situ* ocean temperature underneath the ice shelf ($T_{V(in-situ)}$), and $T_{f(IS_{base})}$. For the Mertz Glacier case, $T_{N(in-situ)}$, $T_{V(in-situ)}$ and $\mathrm{T}_{f(IS_{base})}$ are averaged for the area south of the section described in Figure 4.1b with a corresponding melt rate of $\sim$1.6 m yr^{-1} (2.7 m yr^{-1}) for the PRE (POST) simulation (Table 4.4). For the Ninnis and the Cook ice shelves $T_{N(in-situ)}$, $T_{V(in-situ)}$ and $\mathrm{T}_{f(IS_{base})}$ are averaged for the entire ice shelf area shown on Figure 4.1c and d.

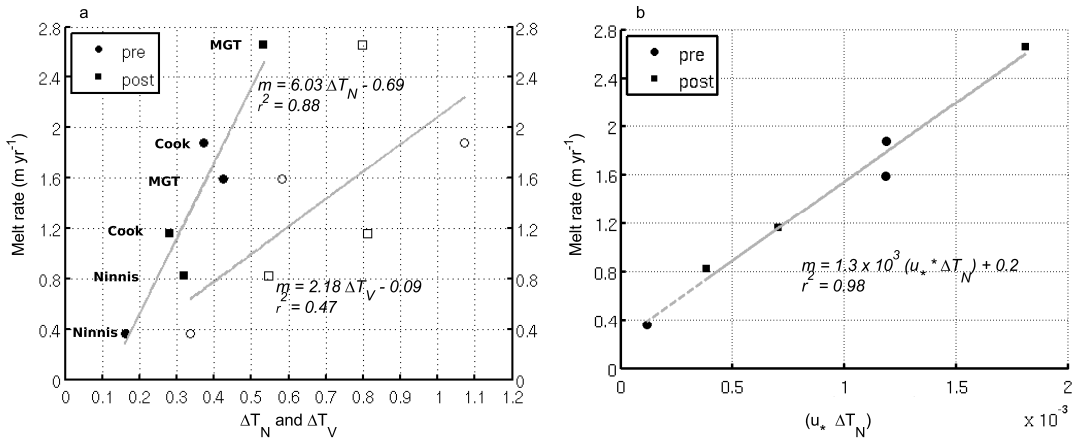

Figure 4.8: Melt rate (m yr^{-1}) function of ΔT_N (filled symbols) and ΔT_V (open symbols), described in the text, for the 3 main ice shelves in the domain for PRE (circles) and POST (squares) simulations (in °C) is shown in panel a. For the Mertz Glacier, the area south of the section across the cavity is considered. Melt rate (m yr^{-1}) function of the friction velocity times ΔT_N for each ice shelf and for PRE and POST simulation is shown in panel b. In both panels, the linear fit is shown with the grey line. The equation and the coefficient of determination (r^2) are given beside each linear fit.

As expected, there is a linear relationship between the melt rate and the 'thermal forcing' calculated here (Figure 4.8a). The coefficient of determination (r^2) for ΔT_N linear fit is 0.88. However, for ΔT_V the $r^2 = 0.47$, illustrating that not all the heat within the ice shelf cavity is used to melt the ice shelf and is highly dependent on each ice shelf. The linear fit for ΔT_N indicates that a 1 °C increase at the top layer of the ocean beneath one of these ice shelf will increase the melt rate by 5.3 m yr^{-1} ($MR = 6.03\Delta T_N - 0.69$).

The non-zero y-intercept (0.69) with the ΔT_N value can result from using only six data points. The result of a non-linearity in melting at low thermal forcing as suggested in previous studies [e.g. Holland et al. 2008; Little et al. 2009] can also be responsible for the non-zero y-intercept. These regressions need to be carefully interpreted as they do not include the impact of friction velocity on the melt rate calculation. Figure 4.8b illustrates that using the friction velocity along with the thermal forcing result in a coefficient of determination closer to 1 ($r^2 = 0.98$) and a y-intercept is closer to zero (0.2) compared to using T_N only.

Collecting data from underneath an ice shelf is a very difficult and expensive task. Several studies have investigated hydrographic data measured underneath an ice shelf via a borehole drilled through the ice shelf. For instance, ocean data un-

Table 4.4: Area averaged melt rate for each ice shelf in the domain with their corresponding friction velocity (u_*: m s^{-1}) and thermal forcing (ΔT_N and ΔT_V detailed in the text: °C) is summarised in this table. The percentage change of each variable between the PRE and the POST simulation is given.

Ice shelf	Melt rate (m yr^{-1})	u_* (m s^{-1})	ΔT_N (°C)	ΔT_V (°C)
Mertz_{pre}	1.4	25×10^{-4}	0.42	0.58
Mertz_{post}	2.3	30×10^{-4}	0.53	0.80
% change	+64	+20	+26	+34
Ninnis_{pre}	0.4	7.2×10^{-4}	0.16	0.34
Ninnis_{post}	0.8	12×10^{-4}	0.32	0.55
% change	+100	+67	+100	+62
Cook_{pre}	1.9	32×10^{-4}	0.37	1.07
Cook_{post}	1.2	25×10^{-4}	0.28	0.81
% change	-37	-22	-24	-24

derneath the Filchner-Ronne ice shelf [Nicholls et al. 2001] or the Amery ice shelf [Herraiz-Borreguero et al. 2015; 2013; Galton-Fenzi et al. 2012] have been used to describe the ocean circulation and the water masses underneath the ice shelf, or to validate ocean model circulation underneath an ice shelf.

Autonomous Underwater Vehicles (AUV) have also been used to measure water properties underneath an ice shelf, for instance underneath the Filchner-Ronne ice shelf [e.g. Nicholls et al. 2006], or underneath the Pine Island Glacier (PIG) in West Antarctica [e.g. Dutrieux et al. 2014]. The PIG is known to have the highest 'thermal forcing' around Antarctica, estimated to be nearly +4 °C [Jacobs et al. 2011; Rignot and Jacobs 2002].

These observations illustrate the water column properties underneath the ice shelf, that could be compared with the linear fit calculated here for ΔT_V. When comparing with observation based studies, ΔT_V is preferred rather that ΔT_N as it uses the volume averaged *in-situ* temperature beneath the ice shelf, which is then closer to the ocean temperature used in these studies. If a 'thermal forcing' of +4 °C is considered, the PIG melt rate would be estimated to be ∼9 m yr^{-1} using the method described in this chapter, while the observations estimate the PIG melt rate is ∼16 m yr^{-1} [Rignot et al. 2013; Depoorter et al. 2013]. It is important to note that the calculations here do not include the velocity beneath the ice shelf, known to be important underneath the PIG due to the cavity geometry [Dutrieux

et al. 2014].

More recently, Autonomous Phase-sensitive Radio Echo Sounders are being used to monitor ice shelf and ice sheet thinning. This new instrumentation allows the collection of time series of the basal melt rates of the monitored ice shelf [Nicholls et al. 2015], and could be applied to the investigation of the seasonal and tidal impact the ocean has on the ice shelf basal melt rate.

4.5 Summary

This chapter investigates the impact the Mertz Glacier Tongue (MGT) calving event had on the basal melt rate, as well as changes to ocean state within the Mertz cavity and the two other major ice shelves in the domain, Ninnis and Cook. This study used an adapted version of the Regional Ocean Modeling System (ROMS) [Shchepetkin and McWilliams 2005]. The simulations are forced with the same lateral boundary forcing, while the air/sea flux forcing is adapted for the pre- and the post-calving ice geometry. This set of experiments allows comparison and quantification of the impact of the calving, and the related ocean state changes, on the area-averaged basal melt rate and ocean heat availability for melting.

The major conclusions of this chapter are as follow:

- An increase in the area-averaged Mertz Glacier basal melting of 89% leads to a 7% increase in the glacial meltwater added into the ocean between the pre- (PRE) and the post- (POST) calving simulation, after a near 50% reduction in the area of the MGT. Higher melt rates in the POST simulation are related to a decrease in salinity of about 0.1 and an increase of about 0.2 °C in potential temperature within the Mertz cavity (Table 4.3 and Figure 4.6).

- Warmer water (by about 0.2 °C) is flowing into the cavity during the POST simulation leading to an increase in basal melting. This relatively warmer (above the surface freezing temperature) water accesses the bottom of the cavity via the Ninnis trough, and reaches the deep ice near the grounding line. The warmer water that reaches the eastern side of the Mertz cavity also contributes to an increased area-averaged basal melt rate at the Ninnis Ice Shelf. The Ninnis basal melt rate is low for the PRE simulation, 0.4 ± 0.2 m yr^{-1}, with a corresponding mass loss of 0.6 ± 0.3 Gt yr^{-1}. This doubles

to 0.8 ± 0.3 m yr^{-1} for the POST simulation, which is still less than half of the area-averaged basal melt rate of the Mertz Glacier and is about 4.6 times lower than the Mertz Glacier mass loss (Tables 4.1 and 4.2).

- Ocean circulation underneath the Mertz Glacier is intensified by the increased of ocean temperature driving a stronger buoyancy circulation, resulting in an increase of about 33% in the magnitude of the transport in the Mertz cavity (Figure 4.7 and Table 4.3).

- Ice shelf basal melt rate in the model domain is strongly related to changes in ocean heat and ocean velocity beneath the ice shelf. The difference between the two definitions of 'thermal forcing' calculated in this chapter illustrates that not all the heat averaged over the water column within an ice shelf cavity is used for melting the ice shelf.

- More analyses are needed to better understand the impact of the changes in air/sea fluxes, as well as the impact of the calving event had on the ocean further north from the cavities and along the continental shelf. The following chapter will focus on the ocean state changes between the PRE and the POST simulation to investigate this last point.

Chapter 5

Impact of calving of the Mertz Glacier Tongue on formation of Dense Shelf Water

5.1 Overview and chapter outlines

This chapter focuses on the changes in the general oceanography of the continental shelf after the Mertz Glacier calving event. It uses the same simulations (PRE and POST) detailed in the previous chapter. Whereas Chapter 4 detailed the changes in ocean/ice shelf interaction, this chapter examines the impact of the calving on Dense Shelf Water (DSW) across the Adélie and George V Land region (AGVL).

The study area for this chapter is centred on the Adélie and Mertz depressions, key regions of DSW formation and export as reported by observational [e.g. Williams and Bindoff 2003; Williams et al. 2008; 2010] and modelling studies [e.g. Marsland et al. 2004; Kusahara et al. 2010; Cougnon et al. 2013]. Also, the impact of the calving has been observed as driving an abrupt decrease of the DSW salinity and density [Shadwick et al. 2013] that correlates with a decrease by 14-20% of the sea ice production in the region [Tamura et al. 2012]. The 2010 calving has also been modelled, simulating a decrease in DSW production of 23% [Kusahara et al. 2011a] (using a critical density limit to defined DSW) and a change of the currents near the Mertz Glacier Tongue (MGT) [Mayet et al. 2013]. However, none of these two modelled based papers include ocean/ice shelf or frazil thermodynamics.

In this chapter, a regional and temporal definition of DSW is used to estimate the change in DSW export between the two simulations. The second half of the chapter explores the impact of the calving event on the downstream production of Antarctic Bottom Water (AABW) from the DSW exported from the AGVL region. The

chapter concludes with an investigation into the downslope pathways and properties of the overflows of newly-forming AABW from the AGVL region, before and after the calving.

This chapter is structured as follows:

- Ocean circulation and water mass properties at the bottom layer of the model on the continental shelf are analysed in Section 5.2 in order to estimate the changes in DSW formation and properties within the Adélie and Mertz depressions due to the drop in sea ice production after the Mertz Glacier calving [Tamura et al. 2012].
- Section 5.3 examines changes of DSW properties and export before and after the calving, downstream of the Adélie and Mertz depressions.
- In order to follow the path of DSW downstream, the bottom layer of the model is analysed and a quantification of the downslope flow is given in Section 5.4.

5.2 Ocean circulation and water mass properties on the Adélie Land continental shelf

The bathymetry and key features of the model domain are shown in Figure 5.1, as well as the oceanographic sections used hereafter for the analyses of the continental shelf. Following Chapter 2, these sections surround the Adélie and Mertz depressions (Adélie and Mertz box) sharing the same edge along the western side of the MGT. Specific ocean sections through the Adélie and Mertz sill are used following Chapter 2 to capture the main DSW export pathways. In the case of the Adélie sill, the transect has been extended further west to capture all DSW export through the sill because the previous transect missed part of the DSW outflow that is deflected westward under the Coriolis force.

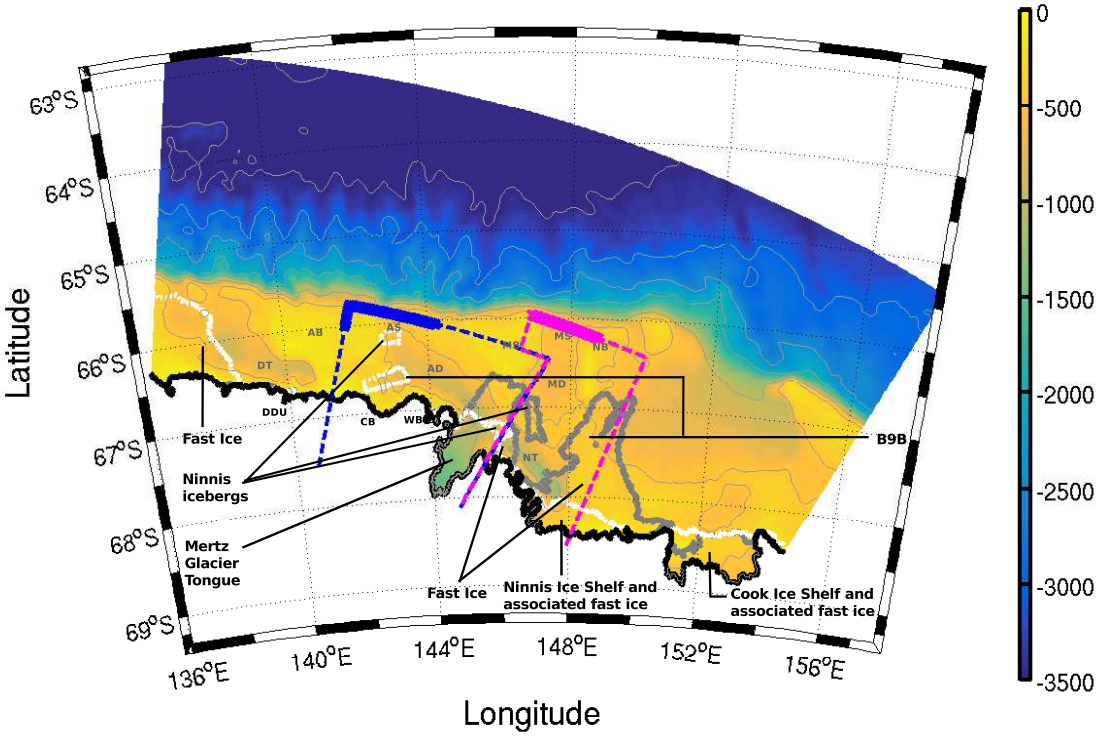

Figure 5.1: Bathymetry of the model domain (m). Blue box (dashed line): Adélie box; bold blue line: Adélie sill; magenta box (dashed line): Mertz box; bold magenta line: Mertz sill as used in Cougnon et al 2013. Grey (white) contours are the ice mask for the PRE (POST) simulations. Grey thin contours are bathymetry contours every 500 m and bold black line the land mask contour. Notable features are indicated on the bathymetry. In the ocean: DT: D' Urville Trough; AB: Adélie Bank; AD: Adélie Depression; AS: Adélie Sill; MB: Mertz Bank; MD: Mertz Depression; MS: Mertz Sill; NB: Ninnis Bank; NT: Ninnis Trough. Along the continent: Watt Bay (WB), Commonwealth Bay (CB), and Dumont D'Urville base (DDU).

5.2.1 Ocean circulation before and after the Mertz calving

The ocean circulation on the continental shelf over the Adélie and Mertz depression for the PRE and POST simulations is investigated in this section. In both simulations the circulation is presented using the vertically integrated horizontal velocity and the bottom velocity of the model, for the PRE (Figure 5.2) and POST (Figure 5.3) simulations, averaged for summer (December, January and February – model days from 1 to 61 and 334 to 364) and winter (June, July and August – model days from 152 to 243).

Oceanographic observations have shown that warm modified Circumpolar Deep Water (mCDW) intrudes onto the shelf over the Mertz Bank [Williams et al. 2008]. In both PRE and POST simulations, water flows onto the continental shelf along the western edge of the Ninnis bank as well as over the Mertz bank. In the PRE simulation, during summer (Figure 5.2a), the Mertz bank inflow (mCDW) interacts with the northern tip of the Mertz Glacier Tongue (MGT). Then the main flow goes westward along the coast and northwestward to join the Adélie sill. Summer bottom velocity (Figure 5.2c) within the Adélie depression shows a different circulation pattern, suggesting a denser water mass (DSW) fills the deepest part of the Adélie depression. A clockwise circulation within the deepest part of the Adélie depression drives DSW to flow towards the MGT and to reach the Ninnis trough and the Mertz cavity along its eastern side wall. Along the western edge of the Mertz cavity, a westward flow is observed along the coast and the southern part of the Adélie depression towards Commonwealth Bay.

The ocean circulation in the PRE simulation averaged for winter (Figure 5.2b) is relatively similar to the general clockwise circulation observed in the region during the Mertz Polynya Experiment in winter 1999 [Williams and Bindoff 2003]. The vertically integrated horizontal velocity vectors (Figure 5.2b) correlate with the bottom velocity vectors (Figure 5.2d), illustrating the clockwise circulation covers the entire water column. Brine rejection and DSW formation within the depression and near Commonwealth Bay sinks to the bottom of the depression, one part of DSW flows westward along the coast and then northward towards the Adélie sill. The other part flows underneath the MGT, into the Mertz cavity and the Ninnis trough, before eventually flowing northwards into the Mertz Depression. On the other hand, mCDW flows southward onto the continental shelf on the Mertz Bank. One part interacts with the Mertz Glacier, while the other part flows back northwestward along the southern flank of the Mertz bank (400-500 m isobath).

Major changes to the ocean circulation were found in the POST simulation (Figure 5.3). While the water masses north of the shelf break follow the same pathways onto the continental shelf, there is a westward flow forming on the continental shelf from south of the Ninnis bank to the Adélie depression (Figure 5.3a and b), with a potential of increasing the input of warm waters into the region and the oceanic heat input to the ice shelves. Pre-calving the ice geometry prevented water masses originating from the east to flow towards the Mertz depression due to the presence of the B9B iceberg grounded along the Ninnis bank. Within the Adélie depres-

sion in winter, a weak clockwise circulation similar to the PRE simulation is seen. Velocity vectors in the bottom layer of the model (Figure 5.3c and d) show an intensification of the clockwise circulation compared to the vertically integrated velocity (Figure 5.3a and b) within the Adélie depression; however weaker than in the PRE simulation, suggesting a decrease in DSW formation. No major seasonal changes are simulated during the POST simulation.

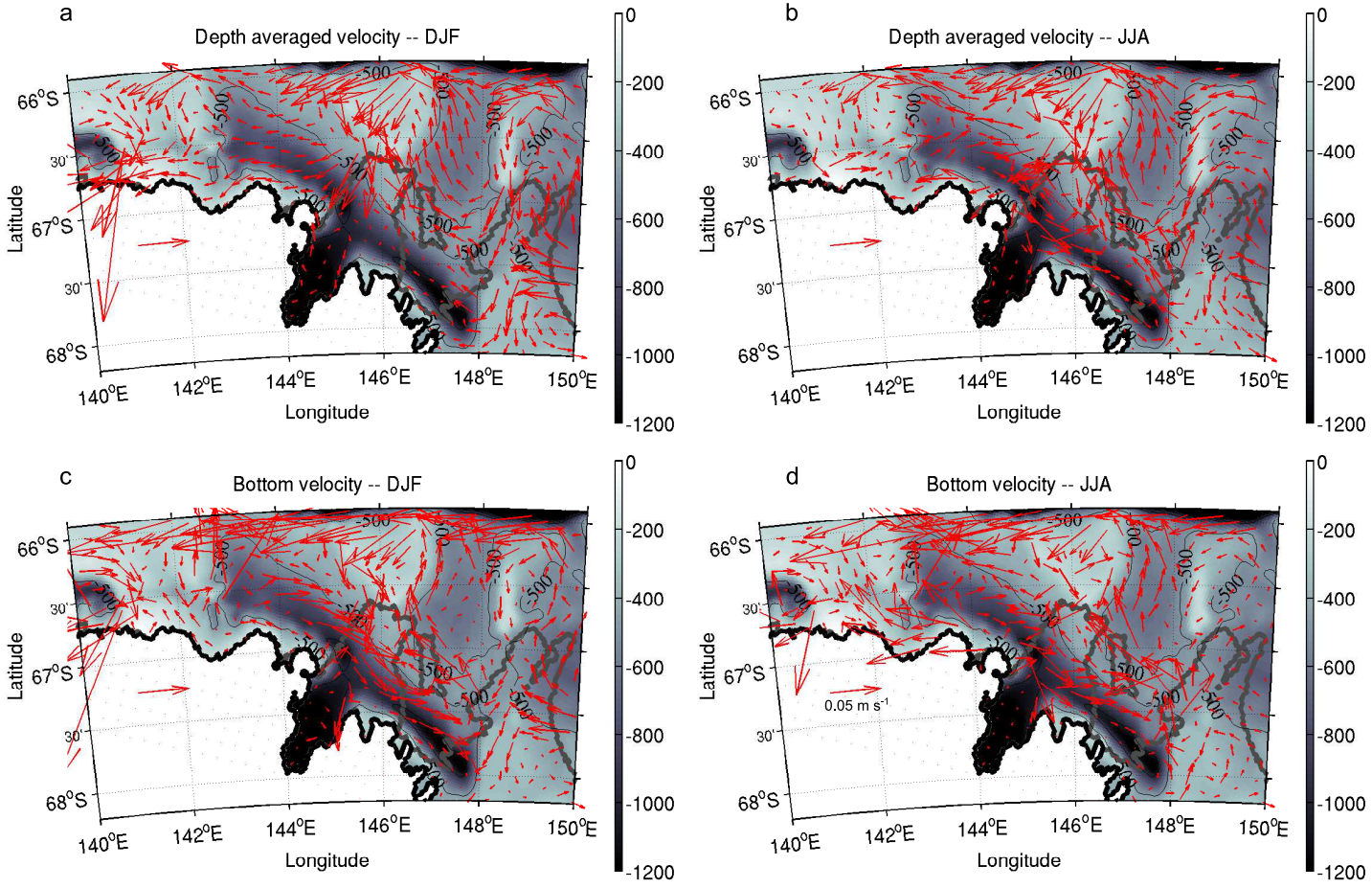

Figure 5.2: Vertically integrated (over the entire water column) horizontal velocity (a and b) and velocity at the bottom layer (c and d) of the model on the continental shelf (Adélie and Mertz depressions) for summer (a and c) and winter (b and d), for the PRE simulation. Unit vector represents 0.05 m s^{-1}. Bathymetry (m) is shown at the background.

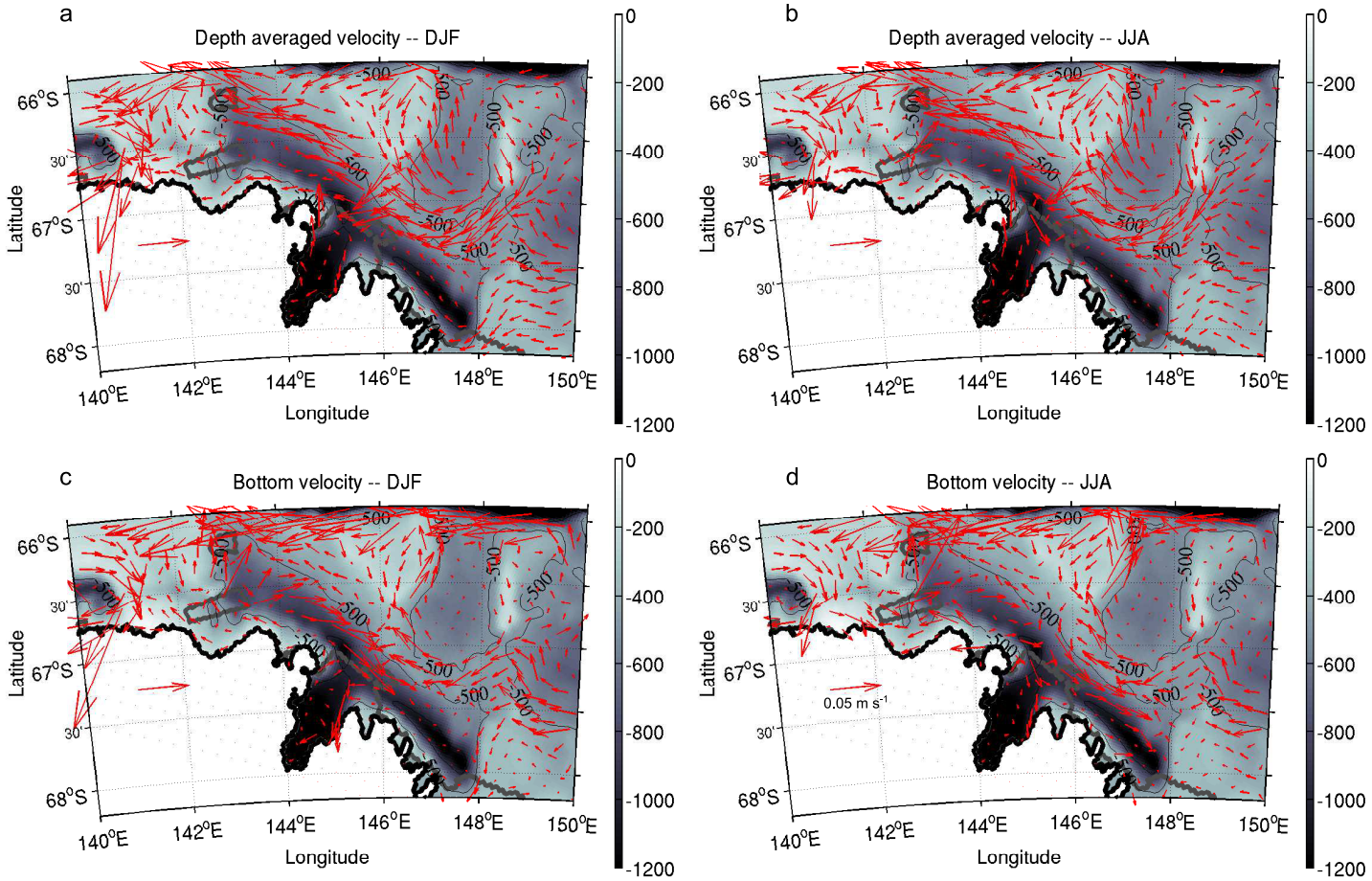

Figure 5.3: Vertically integrated (over the entire water column) horizontal velocity (a and b) and velocity at the bottom layer (c and d) of the model on the continental shelf (Adélie and Mertz depressions) for summer (a and c) and winter (b and d), for the POST simulation. Unit vector represents 0.05 m s^{-1}. Bathymetry (m) is shown at the background.

5.2.2 Water properties of the continental shelf bottom layer before and after the Mertz calving

Water masses formed on the continental shelf are controlled by the variability of the air/sea forcing (see Chapter 2) as well as by the glacial meltwater released from the local ice shelves. Different air/sea forcing are used for both simulations (see Section 4.2). Within the Mertz Glacier Polynya (MGP), north of Watt Bay (averaged over 5 × 5 grid points), the surface heat flux is -220 ± 10 W m^{-2} for the PRE scenario, and decreased by 36% in the same area (-140 ± 30 W m^{-2}) for the POST scenario. Similarly, the fresh water flux present in the air/sea model forcing shows a corresponding increase of 60%, with a fresh water flux for the same area within the MGP PRE (POST) of -3.7 ± 0.3 cm day^{-1} (-1.5 ± 0.6 cm day^{-1}). The cumulative sea ice production for the PRE and the POST simulations is shown in Appendix B (Figure B.4) to illustrates the changes in sea ice location and production for the region.

Water mass properties along the continental shelf near the Adélie and Mertz depressions have changed dramatically between the PRE and POST simulations (see Figures 5.4, 5.5 and Table 5.1). The seasonal (summer and winter) changes in potential temperature and salinity at the bottom layer of the model are seen in Figure 5.4 and 5.5 respectively for the Adélie and Mertz depressions. Water mass properties for specific areas in the bottom layer of the model are summarised in Table 5.1 to quantify the regional changes. The potential temperature at the base of the Adélie depression, the main reservoir of DSW in the PRE simulation, is essentially unchanged in POST and is close to the surface freezing temperature (Figure 5.4). This is confirmed in Watt Bay, shown in Table 5.1, where the potential temperature increased by only 0.04 ± 0.01 °C between the two simulations. Overall this suggests that wintertime convection due to polynya activity is still strong enough to form DSW after the calving. However, the DSW properties have freshened (-0.1 north of Watt Bay, Table 5.1 and Figure 5.5), most likely in response to the decrease in sea ice formation and associated brine rejection.

The greatest change in bottom potential temperature is found over the Mertz Bank and Mertz Depression, north and northeast of the Adélie Depression, respectively. The bottom potential temperature increased by ∼1 °C (Figures 5.4 and Table 5.1). The Mertz depression is affected by the inflow from the east described previously (section 5.2.1) allowing warmer water to get closer to the ice shelf. Pre-calving the

B9B iceberg (grounded at the Ninnis bank) acted as a barrier against warmer water accessing the continental shelf from the east. In addition, in the PRE scenario, the latent heat polynya region in the lee of B9B iceberg modified any warmer water flowing underneath the fast ice near the B9B iceberg, via intense brine rejection. The salinity pattern (Figures 5.5) illustrates the freshening of the water masses on the continental shelf due in part to additional glacial meltwater being released by the increase of ice shelf basal melting, but also as a consequence of the decrease in sea ice production (brine rejection) in the area, reducing the salinity of High Salinity Shelf Water (similar density than DSW but at surface freezing temperature – HSSW) at the base of the depression.

In the PRE simulation, the maximum bottom salinity on the continental shelf is observed within the Adélie depression, the Ninnis trough, the Mertz cavity and within Commonwealth Bay in winter. Observations post-calving have noticed a decrease in bottom salinity of 0.12 between observations taken in 2010 and 2012 in an area between the Mertz Glacier and Watt Bay [Lacarra et al. 2014]. In the model POST simulation, the bottom salinity in the Adélie depression has decreased by 0.11 $\pm$ 0.01, which is in good agreement with the observations. On the other hand, in the model, the salinity on the Mertz bank has increased by 0.08 $\pm$ 0.03, with an increase of the potential temperature of 0.9 $\pm$ 0.2 °C, due to the inflow of mCDW that is less mixed by ambient cold and fresher water masses formed on the continental shelf. However, no measurements were taken near the Mertz bank post-calving to compare with the model as shown on Figure 1 from Lacarra et al. [2014].

Table 5.1: Time averaged bottom potential temperature (θ: °C) and salinity (S), for PRE and POST simulations, with the differences (POST-PRE) for several key areas on the continental shelf. For each area, 5 × 5 grid points at the bottom layer of the model are averaged to estimate the bottom water properties. The deepest part of the deep Adélie depression is defined for an area north of Watt Bay. The deepest area is used along the Adélie and Mertz sill sections and within the Mertz depression. The shallowest area of the Mertz bank is used to quantify the warming of the intruding water masses.

	PRE	POST	POST - PRE
Deep Adélie depression			
θ	-1.915 ± 0.007	-1.87 ± 0.01	+0.04 ± 0.01
S	34.62 ± 0.01	34.51 ± 0.01	-0.11 ± 0.01
Adélie sill			
θ	-1.89 ± 0.04	-1.4 ± 0.2	+0.5 ± 0.1
S	34.61 ± 0.02	34.56 ± 0.007	-0.05 ± 0.02
Top of Mertz bank			
θ	-1.87 ± 0.04	-1.0 ± 0.2	+0.9 ± 0.2
S	34.51 ± 0.03	34.589 ± 0.003	+0.08 ± 0.03
Deep Mertz depression			
θ	-1.86 ± 0.04	-0.85 ± 0.03	+1.01 ± 0.04
S	34.61 ± 0.01	34.616 ± 0.001	+0.01 ± 0.01
Mertz sill			
θ	-1.3 ± 0.1	-0.87 ± 0.06	+0.4 ± 0.2
S	34.608 ± 0.005	34.610 ± 0.004	+0.002 ± 0.005

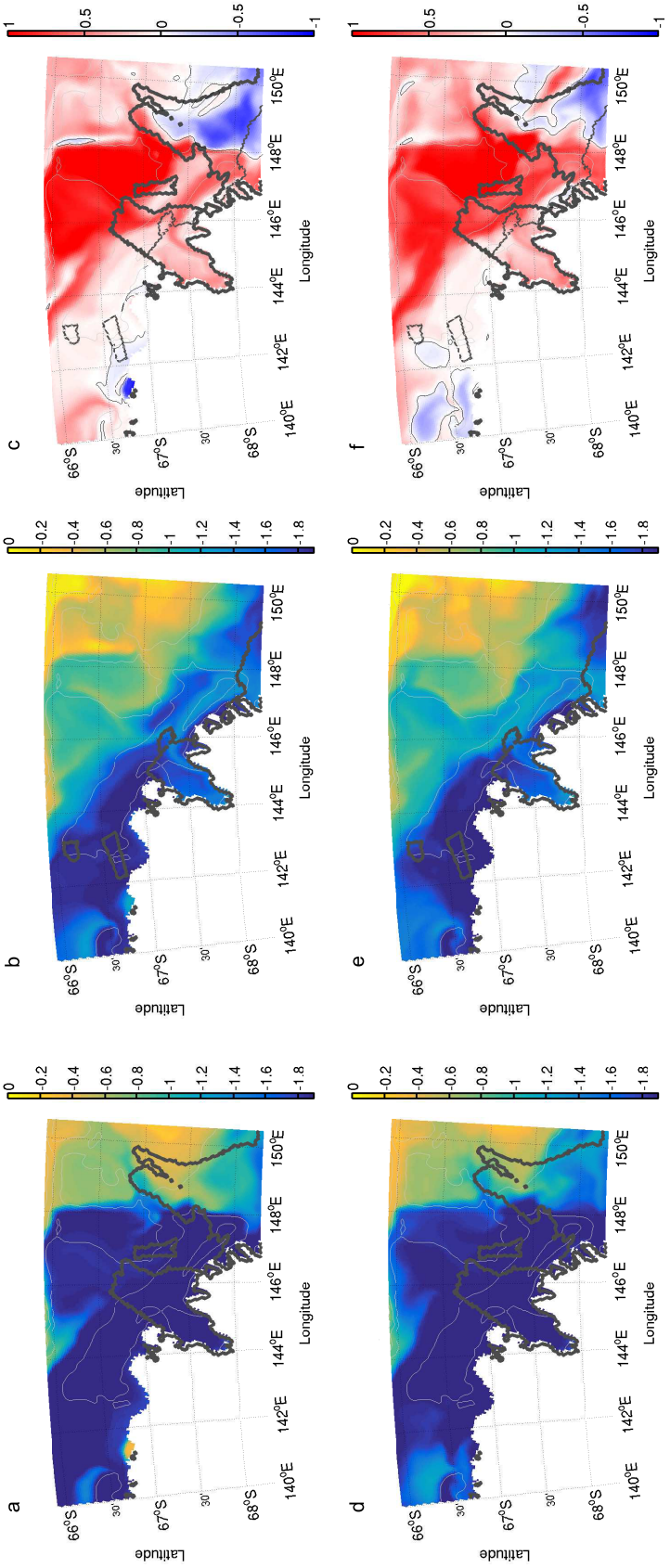

Figure 5.4: Potential temperature (°C) at the bottom layer of the model averaged over summer (December, January and February – a-c) and winter (June, July and August – d-f) for PRE (a and d), POST (b and e) and their differences (POST - PRE – c and f).

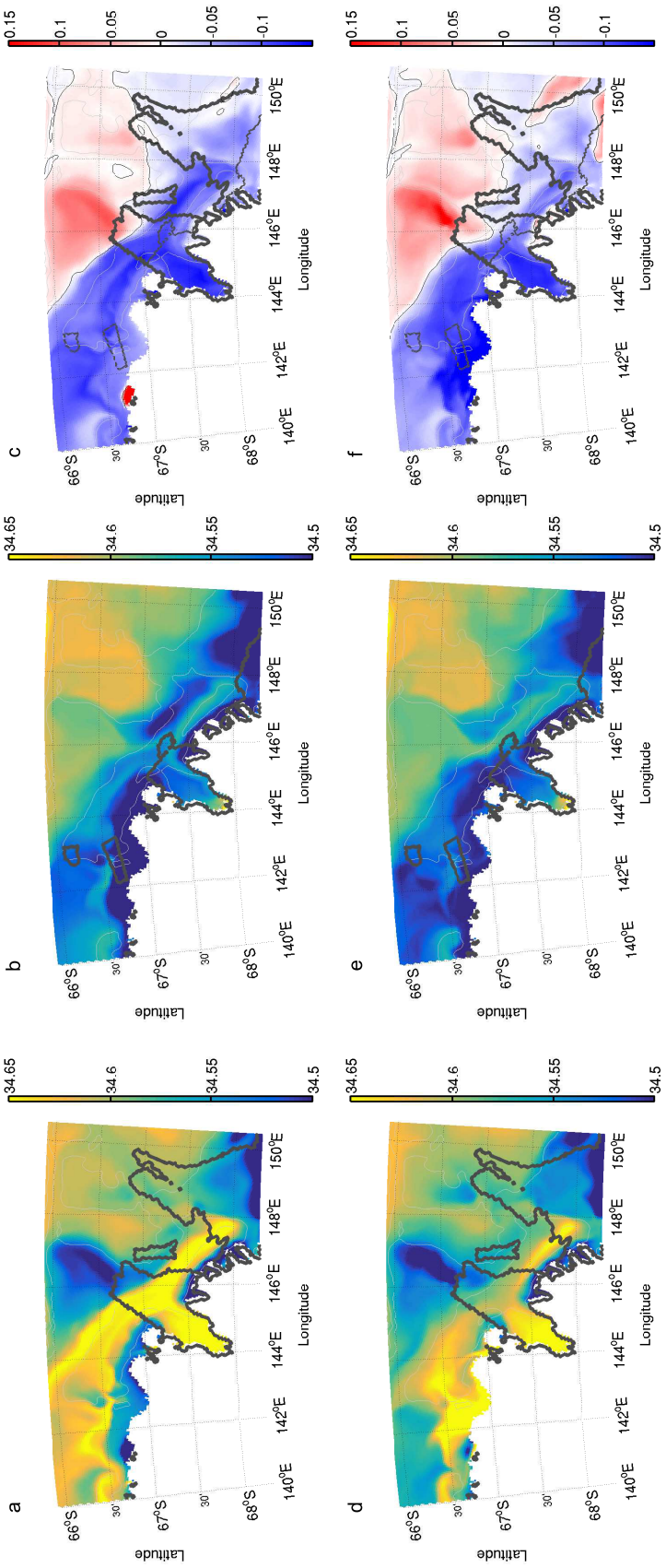

Figure 5.5: Salinity at the bottom layer of the model averaged over summer (December, January and February – a-c) and winter (June, July and August – d-f) for PRE (a and d), POST (b and e) and their differences (POST - PRE – c and f).

5.2.3 Transport through key sections before and after the Mertz calving

The transport through key parts of the previously defined Adélie and Mertz boxes is examined to link the water masses to the observed ocean circulation. The sections are defined as follows from east of the Mertz depression to west of the Adélie depression (Figure 5.6):

- MeE: eastern edge of the Mertz box, to capture any warm flow from the eastern side of the model domain
- MeN: northern edge of the Mertz box including the short section on the west joining the northern edge of the Mertz box to the northern edge of the Adélie box, to capture the inflow of mCDW across the shelf break near the Ninnis bank and the outflow of DSW across the Mertz sill
- AdN: northern edge of the Adélie box but not including the easternmost part common with the Mertz box, to capture the inflow of mCDW across the shelf break near the Mertz bank and the outflow of DSW across the Adélie sill
- AdW: western edge of the Adélie box, to capture the DSW outflow near the coast

Potential Temperature - Salinity (Θ-S) diagrams in Figure 5.6 illustrate the net transport across these sections binned by potential temperature and salinity. Intrusions of mCDW into the Mertz and Adélie boxes occurs via the sections MeE, MeN and AdN. The MeN, AdN and the AdW sections are the areas of main DSW outflow. DSW outflow along the MeN and AdN is located across the respective sill sections (Section 5.3). The transport of mCDW through the sections can be followed with Figure 5.6. In the PRE simulation, along MeE (Figure 5.6e, grey circle), mCDW flows westward into the Mertz depression. Through the MeN (Figure 5.6d, grey circle), a similar mCDW flows northward (Figure 5.6d, grey circle) resulting from the MeE mCDW being modified (mainly cooling) via interactions with the surrounding ice (B9B and fast ice) and local HSSW.

On the other hand, the AdN and AdW (Figure 5.6b and c) are not directly affected by water masses from the Mertz depression, as seen in the ocean circulation discussed in Section 5.2.1 for the PRE scenario. However, mCDW and other lighter

water masses (Antarctic Surface Water and Low Salinity Shelf Water – AASW and LSSW) flow towards the Adélie depression via the AdN section (blue) and denser, colder and saltier water (DSW and highly mCDW) is exported northward (red) after modifications within the Adélie depression due to the addition of HSSW (brine rejection) and interaction with the MGT.

In the POST scenario, mCDW from the MeE (Figure 5.6i) flows westward across the Mertz depression. The warmest (∼0 °C) and saltiest (∼34.6) mCDW along MeE (grey arrow in Figure 5.6i) flows through the MeN section (grey arrow in Figure 5.6h) after being modified (cooled) by the surrounding water masses. According to Figure 5.3, part of this mCDW flows towards the Adélie depression/Mertz bank and eventually crosses the AdN section after interaction with the surrounding HSSW and glacial meltwater resulting in a cooler and fresher mCDW flowing northward (grey arrow in Figure 5.6g). Only a small amount of relatively dense water (DSW – dense enough to flow at the bottom of the water column) is exported through the AdN section (grey circle in Figure 5.6g).

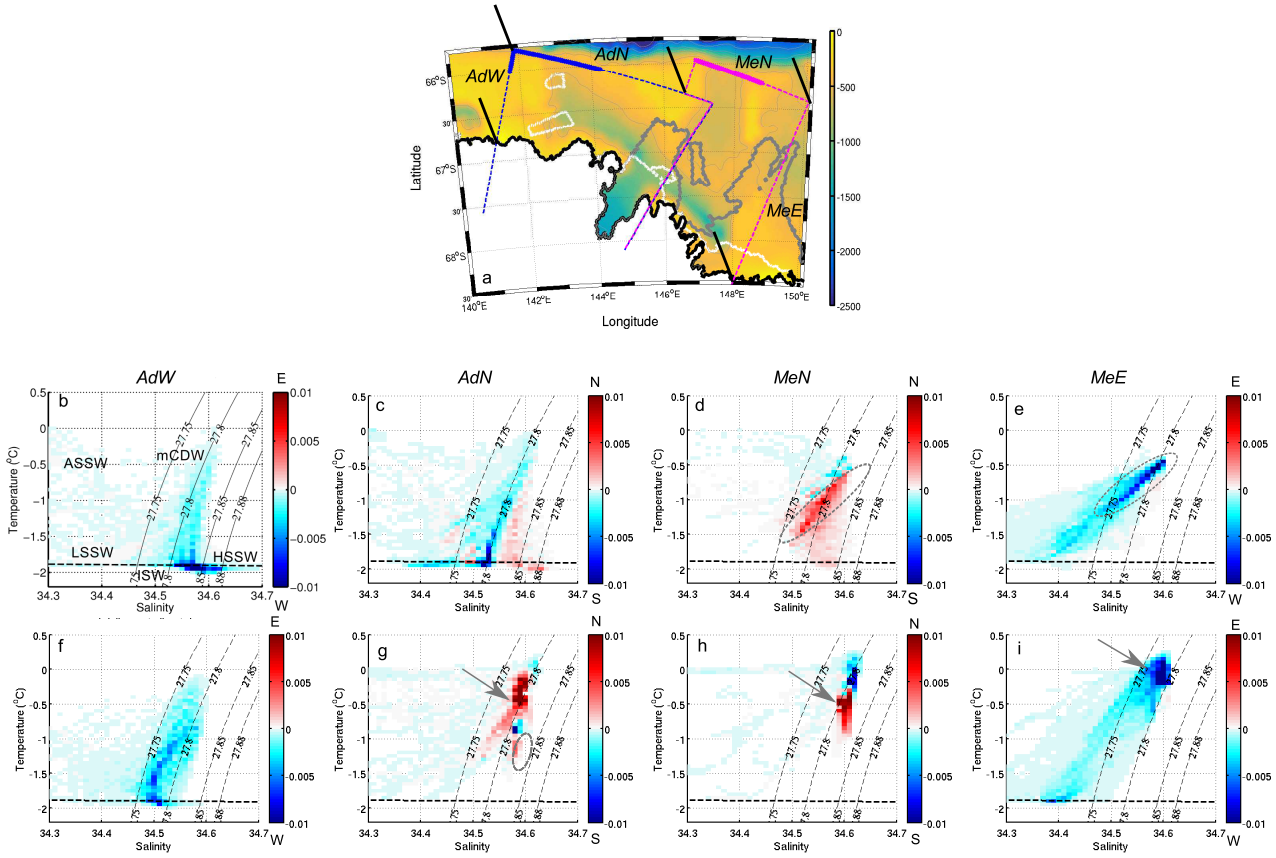

Figure 5.6: Bathymetry (m) and details of the sections around the Adélie and Mertz box (Figure 5.1) are shown in panel a. Potential Temperature - Salinity (Θ-S) diagrams coloured by the net transport (Sv – 10^6 m^3 s^{-1}) across sections for PRE (b-e) and POST (f-i) simulations. For b, e, f and i positive values are eastward and negative westward (normal to the sections). For c, d, e and h positive values are northward and negative values are southward (normal to the sections). The horizontal dashed line corresponds to the surface freezing temperature. Some potential density contours are shown on each diagram. Main water masses are indicated on panel b. Grey arrows and circles show specific features detailed in the text.

In Chapter 2, AdW was identified as a potential outflow section, suggesting that the flow of DSW along the coast could reach the D'Urville trough. Here, the AdW section (Figure 5.6f) is the section that is the least modified in terms of water masses PRE and POST simulations. In both simulations, HSSW and Ice Shelf Water (ISW), with a potential temperature below the surface freezing temperature, are present. However, in the POST scenario the salinity of both water masses is substantially fresher. In the PRE scenario, DSW was advected from the Adélie depression and Commonwealth Bay towards the western boundary of the Adélie box. Post-calving a polynya is formed in the lee of the post-calving position of the B9B iceberg, driving HSSW formation near AdW at a weaker rate and fresher than the HSSW present in the PRE simulation, as suggested in Fogwill et al. [2016].

5.3 DSW export before and after the Mertz calving

5.3.1 Defining DSW

Changes in the export rate of DSW and its water mass properties (salinity, potential temperature and potential density) is analysed in this section. As mentioned in Chapter 2 and in Williams et al. [2010], using a fixed critical limit to define DSW is not ideal and may underestimate the export of DSW. In addition, using water mass definitions based on observations may not be appropriate for modelling studies given biases in the model. Here, DSW export is estimated as being the densest water mass at the bottom of the water column (denser than any inflowing water masses into the Adélie or Mertz box) flowing across one of the sections defining each box, excluding HSSW that flows from the Adélie to the Mertz box in the PRE scenario.

A focus is given to the sill sections near the shelf break, where DSW flows off-shelf and is potentially able to contribute to AABW formation. This new way to define DSW in a model study allows the potential density limit of DSW to change over time and to differ between the Adélie and Mertz formation regions. The maximum potential density simulated around the Adélie box is approximately 1027.95 kg m^{-3} for the PRE simulation and approximately 1027.85 kg m^{-3} for POST (Figure 5.7a and b). This decrease in potential density of the densest exported water mass is a consequence of the freshening described in section 5.2.2 that drives less and lighter DSW formation in the POST simulation.

The maximum density of DSW export from the Mertz box is 1027.87 kg m^{-3} PRE and 1027.83 kg m^{-3} POST simulations (Figure 5.7c and d). As described in Chapter 2, pre-calving, dense HSSW from the Adélie depression flows underneath the MGT to access the Ninnis trough and eventually flows into the Mertz depression and mixes with the ambient HSSW formed via the B9B polynya. DSW exported from the Mertz box in the PRE scenario is a mixture of this dense HSSW coming from the Adélie depression, the HSSW formed locally via the polynya in the lee of the B9B iceberg and mCDW intrusions into the area. In the POST simulation, the connection between both depressions via the Ninnis trough is not as obvious as in the PRE simulation, in part because of the decrease in HSSW production within the Adélie depression. The densest water mass being exported through the Mertz box is very similar to the imported water masses within the Mertz box (Figure 5.7d). Very little water mass transformation occurs within the Mertz depression for the POST simulation.

It is interesting to note the substantial difference between the PRE simulation and the interannual forcing simulation discussed in Chapter 2. Potential density of DSW for the interannual forcing simulation was mainly greater than 1027.88 kg m^{-3} for a mean to strong polynya activity, while the PRE simulation has an averaged DSW potential density of 1027.84 kg m^{-3} for the Adélie depression. The PRE simulation described in this chapter is different from the Chapter 2 simulation mainly due to the modifications applied on the air/sea forcing that decreases the amount of salt released into the ocean (Appendix A).

Also, the heat and salt fluxes data from Tamura et al. [2016] used in the air/sea forcing for the PRE and POST simulations are derived from Special Sensor Microwave Imager (SSM/I) observations using the European Centre for Medium-Range Weather Forecast Re-Analysis data (ERA-Interim), while the simulation in Chapter 2 uses heat and salt fluxes derived from SSM/I observations using the National Centers for Environmental Prediction/Department of Energy Re-Analysis data (NCEP2). According to Tamura and Ohshima [2011] sea ice production calculated using the NCEP2 data is higher by $\sim$12% compared to the sea ice production calculated with ERA-Interim data. Differences in heat and salt fluxes imposed at the surface between the interannual forcing Mertz simulation (Chapter 2) and the PRE/POST simulations explain the differences in DSW export and water mass properties.

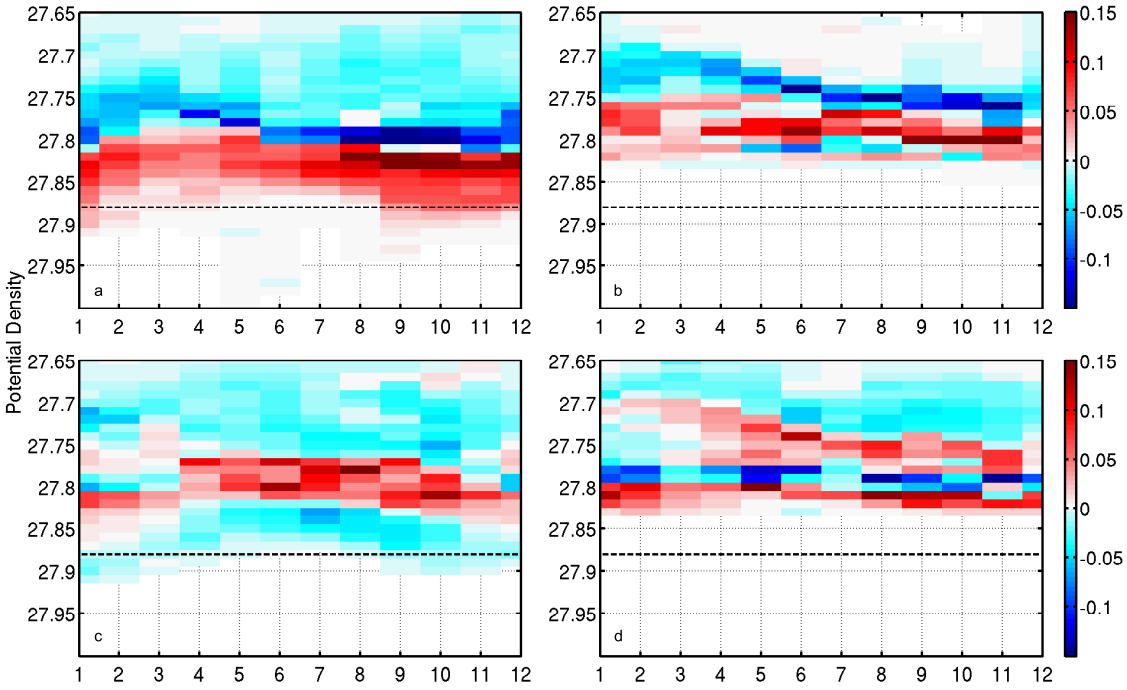

Figure 5.7: Transport (Sv or 10^6 m^3 s^{-1}) by potential density class (in kg m^{-3} -1000), monthly averaged from the 6-hourly climatology. Positive values (red) correspond to an export outside of the Adélie (a and b) and Mertz (c and d) box; negative values (blue) correspond to an import into the Adélie and Mertz box, for the PRE (a and c) and POST (b and d) simulations. Horizontal dashed line is the critical density 1027.88 kg m^{-3} usually used to define DSW able to contribute to the AABW formation.

5.3.2 Changes in DSW properties

DSW properties exported from the Adélie and Mertz depression are investigated in this section. As each box surrounds both depressions, DSW formed within each depression is exported across one of the sections. For the PRE scenario DSW is relatively easy to identify and estimate compared to the relatively light incoming mCDW (Figure 5.7a and b). In the POST scenario, two ranges of density are exported and two ranges of density are imported into both depressions (Figure 5.7c and d). The transition from outflow to inflow (red to blue in Figure 5.7) is taken as the minimum density defining the DSW layer in each box. However, very weak import is seen within the greatest density classes. For instance, a weak import into the Adélie box of the 1027.97 kg m^{-3} density class in June (Figure 5.7a), with a transport value less than 10^{-4} Sv (10^6 m^3 s^{-1}), is negligible. The minimum density

for DSW (evolving in time) defined for the Adélie and Mertz boxes are then used for the Adélie and Mertz sills respectively.

The averaged net DSW transport and its water properties through each box and sill for the monthly climatology from the PRE and POST simulations are given in Table 5.2. Transport-weighted DSW properties of the climatology are also given in Table 5.2, with the maximum and minimum to illustrate the distribution of each property within the exported layer. Around the Adélie box, the export of DSW decreased by 80% between the PRE and POST simulation. DSW potential density decreases by $\sim$0.03 kg m^{-3} around the Adélie box but the averaged salinity has not changed between both simulations ($\sim$34.59). On the other hand, the DSW potential temperature increases by $\sim$0.7 °C. The most interesting POST scenario change in the DSW export for the Adélie box is seen by examining the extrema. The maximum potential density simulated around the Adélie box for the POST simulation has decreased by $\sim$0.1 kg m^{-3} and the maximum salinity by $\sim$0.08 forming a more homogeneous DSW. Lighter, warmer and more homogeneous DSW exported around the Adélie box illustrates that DSW is more susceptible to mix with mCDW in the POST simulation.

Similarly, DSW export at the Adélie sill decreases by 33% in the POST simulation compared to the PRE, associated with a decreased in the averaged potential density of $\sim$0.03 kg m^{-3} and an increase of the potential temperature of $\sim$0.7 °C, with no change in the salinity. The increase in potential temperature and salinity across the Adélie sill is likely to be caused by the westward mCDW flow along the southern edge of the Mertz bank (see Section 5.2.1). This relatively warm mCDW flowing onto the continental shelf during the POST simulation is less modified by brine rejection than during the PRE simulation. Along the western edge of the Adélie box (south of the Adélie sill section) the potential temperature has not changed, but the potential density and the salinity have decreased by $\sim$0.5 kg m^{-3} and 0.6 respectively with DSW export decreased by 63 % (Table 5.2). The decrease in salinity, while temperature is unchanged and near the surface freezing point, implies a direct link to the decrease in sea ice production (brine rejection) in this region, as also suggested in Section 5.2.3.

Sea ice conditions within the Mertz box for the PRE scenario are different from the Adélie box. More fast ice and icebergs are present within the Mertz box pre-calving, decreasing the salinity compared to the Adélie box because of lower brine

rejection and increased meltwater. The sea ice production for the polynya area within the Mertz box (in the lee of the B9B iceberg – PRE) is less intense than for the polynya within the Adélie box. In addition, DSW from the Adélie depression accesses the Mertz depression via the Ninnis trough, preconditioning the volume of DSW from the Mertz depression within the Mertz box. In the POST simulation, the exported DSW has a similar potential density (1027.812 ± 0.005 kg m^{-3}) than in the PRE simulation (1027.80 ± 0.02 kg m^{-3}), but covers a smaller range between the maximum and the minimum potential density around the Mertz box.

Table 5.2: Twelve months average climatology DSW export, and transport-weighted properties per density class for DSW potential density (σ_0), potential temperature (θ) and salinity (S), associated with the average climatology of the maximum and minimum of each water property.

sections	DSW export (Sv)	σ_0 (kg m^{-3}) − 1000			θ (°C)			S		
		mean	min	max	mean	min	max	mean	min	max
Adélie box										
PRE	0.5 ± 0.2	27.84 ± 0.01	27.81	27.93	-1.7 ± 0.1	-1.919	-1.5	34.59 ± 0.01	34.56	34.69
POST	0.1 ± 0.1	27.81 ± 0.02	27.80	27.83	-1.0 ± 0.4	-1.2	-0.8	34.59 ± 0.02	34.57	34.605
POST-PRE	-80%	-0.03	-0.01	-0.10	+0.7	+0.72	+0.7	0.00	+0.01	-0.08
Adélie sill										
PRE	0.3 ± 0.1	27.83 ± 0.01	27.81	27.88	-1.4 ± 0.2	-1.93	-1.0	34.59 ± 0.01	34.58	34.63
POST	0.2 ± 0.3	27.80 ± 0.02	27.78	27.82	-0.7 ± 0.2	-1.0	-0.6	34.585 ± 0.007	34.57	34.594
POST-PRE	-33%	-0.03	-0.03	-0.06	+0.7	+0.93	+0.4	-0.00	-0.01	-0.04
Adélie west										
PRE	0.08 ± 0.07	27.84 ± 0.03	27.82	27.91	-1.8 ± 0.2	-1.9	-1.7	34.59 ± 0.03	34.57	34.67
POST	0.03 ± 0.05	27.79 ± 0.03	27.79	27.82	-1.8 ±0.1	-1.89	-1.8	34.53 ± 0.04	34.52	34.56
POST-PRE	-63%	-0.05	-0.03	-0.09	0.00	+0.01	-0.1	-0.06	-0.05	-0.11
Mertz box										
PRE	0.3 ± 0.1	27.80 ± 0.02	27.79	27.84	-1.3 ± 0.1	-1.7	-1.45	34.56 ± 0.02	34.54	34.59
POST	0.16 ± 0.08	27.812 ± 0.005	27.806	27.83	-0.6 ± 0.1	-0.83	-0.5	34.605 ± 0.003	34.603	34.613
POST-PRE	-47%	+0.01	+0.02	-0.01	+0.7	+0.87	+0.95	+0.05	+0.06	+0.02
Mertz sill										
PRE	0.3 ± 0.1	27.81 ± 0.01	27.79	27.854	-1.2 ± 0.1	-1.8	-0.9	34.58 ± 0.02	34.55	34.60
POST	0.12 ± 0.05	27.813 ± 0.005	27.806	27.829	-0.5 ± 0.1	-0.89	-0.4	34.611 ± 0.004	34.607	34.614
POST-PRE	-60%	0.00	+0.02	-0.02	+0.7	+0.9	+0.5	+0.03	+0.06	+0.01

The exported DSW in the POST simulation is warmer by ∼0.7 °C and saltier by ∼0.05 in average (Table 5.2). It is interesting to note that the minimum DSW potential temperature has increased by almost 0.9 °C in the POST simulation around the Mertz box, illustrating that near-freezing HSSW is no longer present in the Mertz depression. Warm and salty mCDW is modified within the Mertz box to become the densest water mass in the area (∼1027.81 kg m^{-3}) and is less likely to contribute to AABW formation than HSSW previously formed with the PRE conditions. However, this relatively warm DSW (densest exported water mass) that crosses the Mertz sill could precondition the inflowing water masses over the Mertz bank that reach the Adélie depression as it flows westwards.

5.3.3 DSW seasonality at the Adélie sill

This section focuses on the best-known and observed DSW export pathway, the Adélie sill. To evaluate the seasonality of DSW exported through the Adélie sill, the bottom layer of the model along the Adélie sill section is analysed (Figure 5.8). It is important to note that the Adélie sill section used here is just north of the shelf break to capture DSW exported from the continental shelf, with an averaged maximum depth of approximately 440 m ranging from 230 m to 600 m. As a result, the Adélie sill section in the model is impacted by different dynamics (downstream of the shelf break) than from the continental shelf and could explain some differences in water mass properties compared to observations (moorings) made just south of the shelf break, as the bottom water mass endures more mixing while descending the slope.

Pre-calving, the seasonality is similar to the observations from Williams et al. [2008], with a maximum potential density and salinity that plateaus in October/November for the observations and through October to December for the model (days 274 to 364). The maximum density period also corresponds to the minimum in potential temperature, near surface freezing temperature. However, the increase in potential density and salinity is later in the model (∼ September) than for the observations (∼ July). Also, the model simulates weaker salinity and potential density ranges than mooring observations taken at the Adélie sill during several years. Bottom potential density ranges between 1027.83 kg m^{-3} to 1027.97 kg m^{-3} in the mooring data (averaged between measurements from 1998, 1999 and 2008, from Williams et al. [2008] and Snow et al. [manuscript in preparation]), while the model simulates

potential density between 1027.81 kg m^{-3} to 1027.88 kg m^{-3} (Table 5.2) across the Adélie sill section for the PRE simulation.

The seasonal cycle of the potential temperature and density POST simulation in the bottom layer of the model follows a similar pattern to the PRE simulation through the Adélie sill section (Figure 5.8a and c), with a potential density maximum late November/December (days 305 to 350). However, this bottom layer (POST simulation) is warmer by 0.62 ± 0.09 °C and lighter by 0.04 ± 0.01 kg m^{-3} over the climatology compared to the PRE simulation. Very little seasonality is seen for the salinity in the POST climatology and is on average fresher by 0.03 ± 0.02 compared to the PRE simulation (Figure 5.8b). The seasonality in the model is different from the observations, where a clear seasonal cycle is present at the bottom of the sill with a salinity difference of about 0.13 (0.08) pre-(post-)calving between the spring and autumn means [Snow et al., manuscript in preparation].

The differences in salinity and potential density observed in the mooring data for the peak of the DSW export period pre- and post-calving are comparable to the model. The model simulates a freshening of 0.049 ± 0.003 with a decrease in potential density of 0.055 ± 0.003 kg m^{-3} for the period from day 305 to 350, while the moorings show a freshening of about 0.05 (34.71 pre-calving to 34.66 post-calving) in spring and a decrease in potential density of 0.05 kg m^{-3} (1027.96 to 1027.91kg m^{-3}) using measurements averaged over the years 1998, 1999 and 2008 for the pre-calving and 2011 and 2012 for the post-calving [Snow et al., manuscript in preparation].

Lighter HSSW is formed due to weaker polynya activity over the Adélie depression for the POST simulation resulting in a lighter DSW that mixes more easily with the surrounding mCDW. As described in Section 5.2, the Adélie sill section is impacted by the northwestward mCDW flow that carries warmer water and this in part explains the warming of the POST bottom layer. This could also explain the weakening of the seasonal cycle compared to the observations. However, in both model and observations DSW exported during the peak period has freshened and became lighter. It is also interesting to note that a higher temporal variability is seen in the POST climatology of the model compared to the PRE simulation, in particular during the winter months.

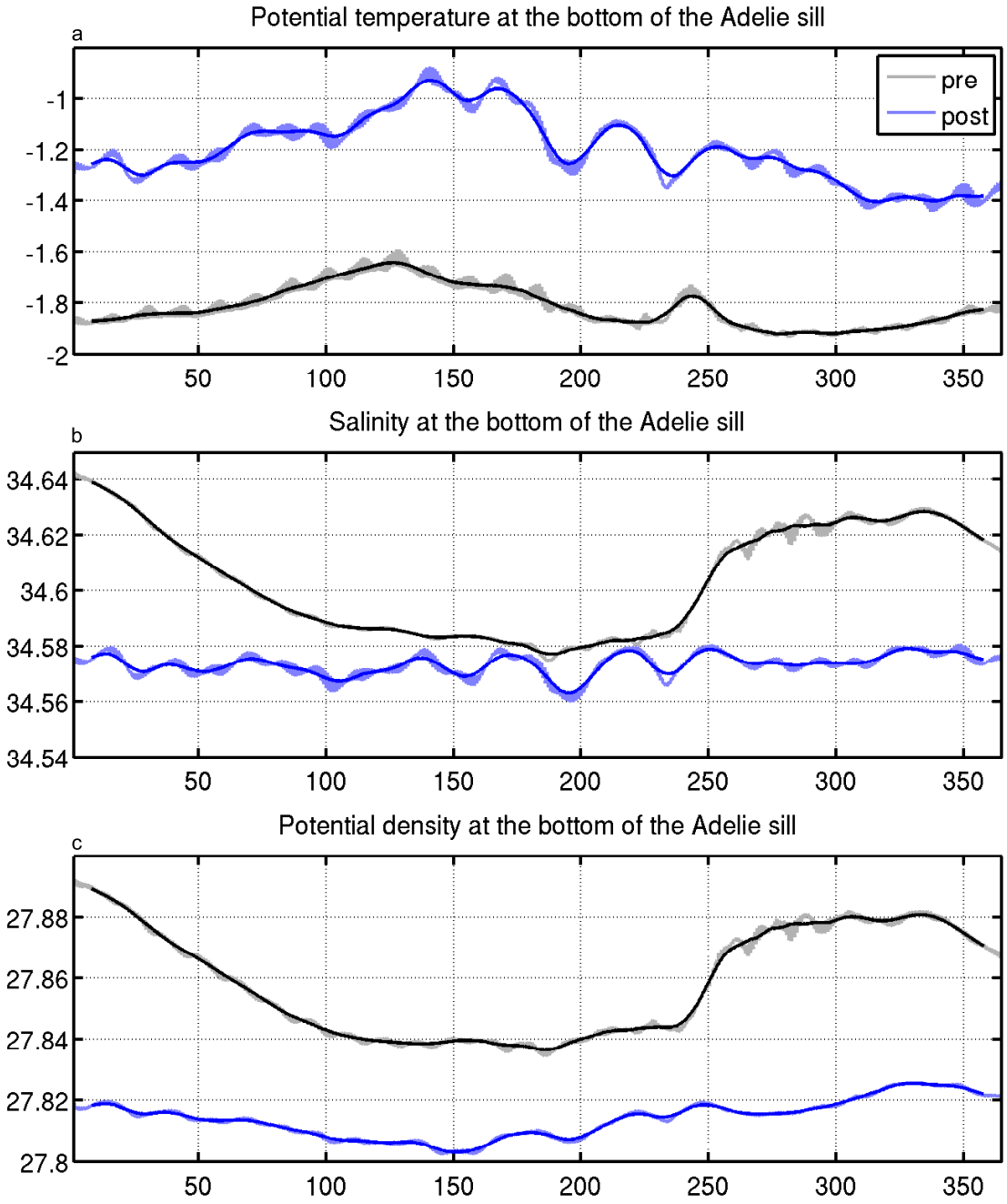

Figure 5.8: 6-hourly climatology with 14 days running average (to remove the tidal signal) of the potential temperature (a), salinity (b) and potential density (c) along the bottom layer of the Adélie sill section.

To illustrate the differences between PRE and POST conditions at the Adélie sill in the model, two snapshots of the potential temperature are shown in Figure 5.9 corresponding to the minimum potential density (day 150) seen in both simulations at the bottom layer and the maximum potential density (day 325) for both simulations

(Figure 5.8). PRE scenario, for both snapshots (Figure 5.9a and b), a clear contrast in potential temperature is seen all along the section between near surface freezing temperature at the bottom and relatively warm water (> -1 °C) above, illustrating the DSW outflow (Figure 5.9a and c).

POST scenario, at day 150 (Figure 5.9c), relatively warm water fills the bottom of the Adélie sill section except along the western edge of the section where relatively cold water dominates the water column. This relatively cold water (near surface freezing temperature) is associated with a deepening of the potential density contour. This light and cold water mass corresponds to the glacial meltwater formed by the basal melting of Ninnis iceberg located south of the Adélie sill section and being advected through the section. At day 325 (Figure 5.9d) a relatively cold water layer is seen along the bottom of the Adélie sill section at day 325, corresponding to the maximum in DSW export across the Adélie sill for the POST simulation.

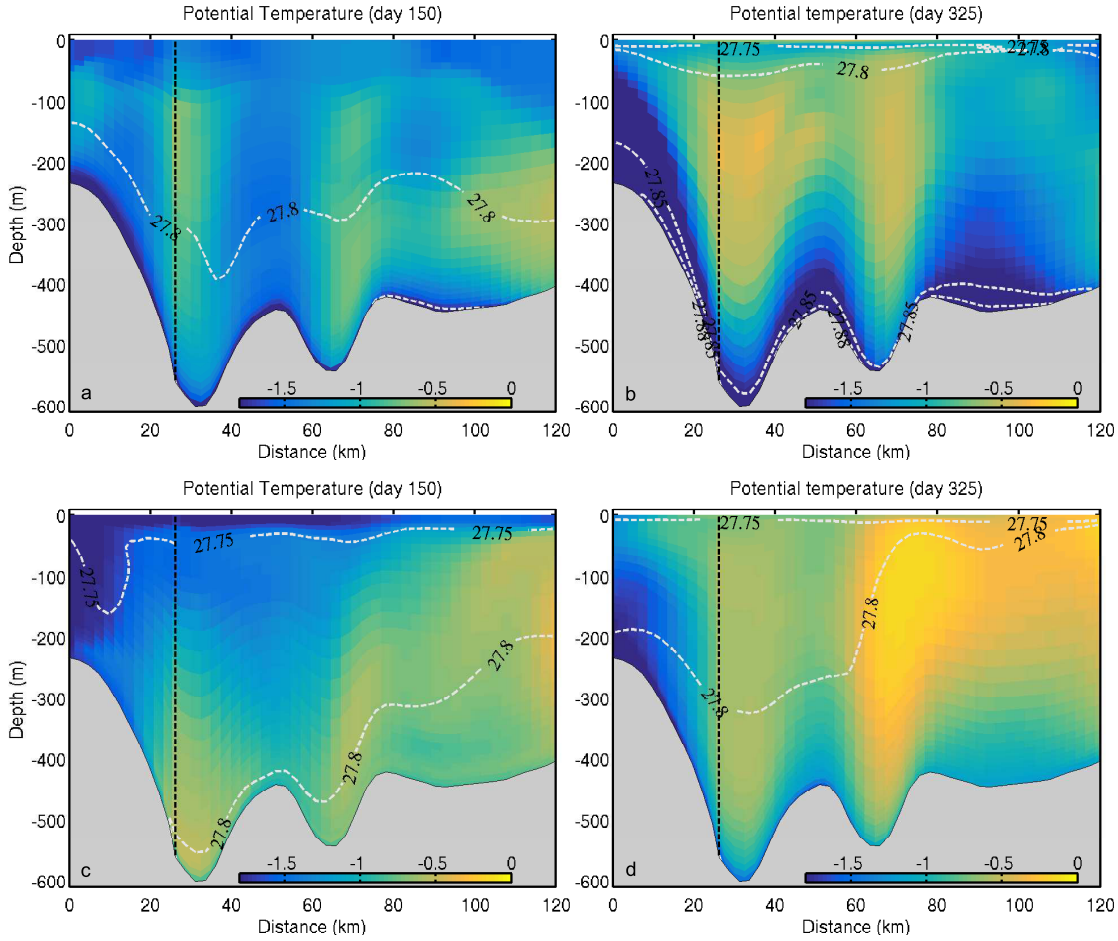

Figure 5.9: Snapshots of potential temperature (°C) for PRE (a-b) and POST (c-d) at day 150 (a and c) and 325 (b and d) along the Adélie sill section, as in Figure 5.1. Potential density (kg m^{-3} -1000) is shown with white contours. The vertical black dashed line shows the corner of the Adélie sill section (Figure 5.1).

5.4 Impact on the downstream production of ALBW

5.4.1 Spatial distribution of Bottom Water

Potential temperature and salinity at the bottom layer of the model (Figure 5.10) illustrate where the relatively cold and fresh Bottom Water (BW) formed on the continental shelf flows along the slope to the deep ocean to eventually become Adélie Land Bottom Water (ALBW). This BW is also referred to as modified Shelf Water in recent literature [Orsi and Wiederwohl 2009] before reaching 2500 m depth. It

is important to note that the lateral boundary forcing used for these simulations comes from a 22 year climatology (1992-2013) calculated from the monthly fields from ECCO2 reanalysis [Menemenlis et al. 2008; Wunsch et al. 2009]. However, the ECCO2 reanalysis does not represent the densest AABW variety and produces a warmer and less dense AABW compared to observations [Azaneu et al. 2014]. Also, within the Australian-Antarctic basin the AABW volume is underrepresented and there is no ALBW present in the reanalysis.

BW present in the model domain is thus formed on the continental shelf within the model domain. Due to the relaxation time scale of 30 days applied on the inflow and outflow along the boundaries, not all BW formed in the model domain is able to be exported outside of the model domain through the western boundary. Instead, BW re-circulates northward along the western boundary and eventually floods the deepest area of the model domain and exits slowly through the northern boundary.

In the observations, it is known that AABW found in the Australian-Antarctic basin is a mixture of ALBW, formed along the Adélie Land and George V coast, and the Ross Sea Bottom Water (RSBW) formed further east within the Ross Sea and flowing westward towards the Adélie Land Region [Rintoul 1998]. RSBW is relatively warm and salty, while ALBW is cold and fresh. In the area of the model domain, the two BW types can still be distinguished in the observations. In this model, only one type of BW is present, ALBW. Instead of mixing with a slightly warmer and salty BW (RSBW), ALBW formed in the model mixes with a warm (positive potential temperature) and salty water with properties similar to CDW at the boundaries.

Relatively cold and fresh BW is found mainly on the western area of the model domain for both the PRE and POST simulations (Figure 5.10), while warm and salty water fills the eastern area (between 145°E and 157°E) of the bottom layer of the model domain, originating from the boundary conditions. This warm and salty water does not change between both simulations as illustrated by the difference map (Figure 5.10c and f). However, the western area of the model domain (between 136°E and 145°E), is directly impacted by shelf water.

'Streams' of cold and fresh water can be followed from different points along the shelf break following bathymetry features (channels) for both simulations. In the PRE scenario, BW overflow along the slope are simulated at the Mertz sill, the Adélie sill and along the Adélie bank. These overflows do not flow directly north-

ward but are instead deflected westward by the Coriolis force and flow progressively northwestward down to the continental rise following bathymetry features. The bathymetry in this region is very important as the densest water mass follows a system of channels with steep edges [Caburlotto et al. 2006] present along the slope and continental rise.

In the POST simulation, similar BW overflow pathways down the continental rise are observed (Figure 5.10b and e) but, the bottom layer is warmer and saltier compared to the PRE simulation. No signal of BW is clearly observed between 140°E to 145°E and along 64.5°S. On the other hand, along the shelf break, the water mass at the bottom is fresher in response to fresher DSW flowing off-shelf. The fact that lower on the slope BW becomes saltier than the PRE simulation illustrates that the lighter BW in POST is more susceptible to mix with CDW than during the PRE simulation. Also, salty water from the boundary conditions across the slope and rise is less diluted due to less DSW exported through the shelf break.

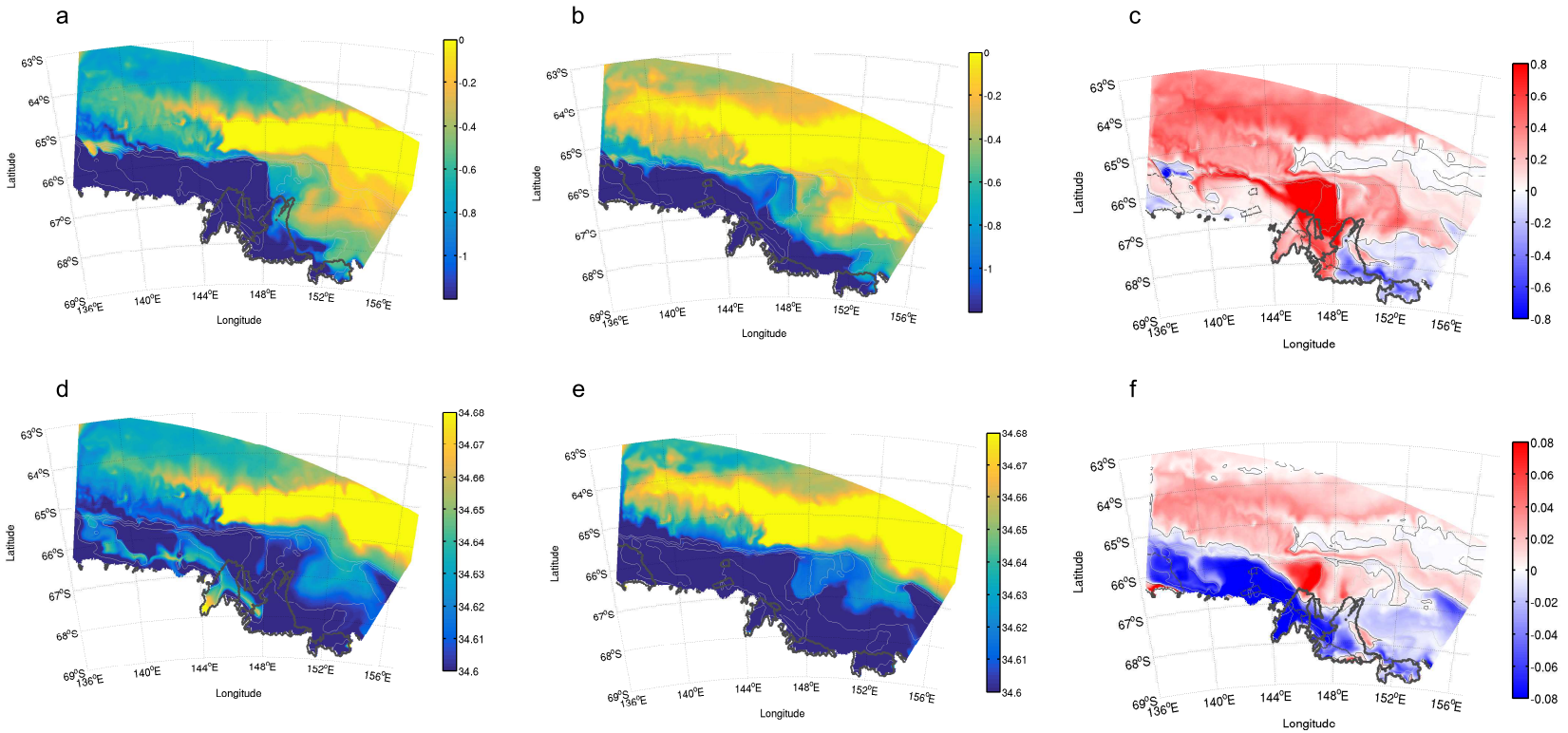

Figure 5.10: Potential temperature (°C: a-c) and salinity (d-f) at the bottom layer of the model for PRE (a and d) and POST (b and e) simulations averaged for the entire 6-hourly climatology with their differences (c and f). Thick grey contours highlight the ice mask for each simulation and the thin black contour highlight the zero contour on the differences panels (c and f).

5.4.2 Quantifying the downslope flow of Bottom Water

As demonstrated earlier, using a fixed density limit to define BW is not ideal. To follow the plume of DSW from the shelf break down to the continental rise, also called gravity current, and estimate its thickness and water properties, the method of Muench et al. [2009] is used to define the upper limit of the BW layer. Muench et al. [2009] used the inflection point in Θ - S space between the BW and the overlying CDW for each CTD (Conductivity, Temperature and Depth profiler) cast. In the model, warm and salty water is present at the sea floor of the eastern area of the model domain, due to the boundary conditions and cannot be defined as BW. To avoid defining a BW layer that is not formed via continental shelf processes, a potential temperature condition is used. The method is applied only if the bottom layer of the model has a potential temperature below 0 °C, then using Muench et al. [2009] method the upper limit of BW is defined. However, near the shelf break, the potential temperature at the bottom layer can be negative while the water column is relatively well mixed and the inflection point in Θ - S space is not clear. No BW is defined in this case to avoid defining the entire water column as BW. An example of the Muench method is shown in Figure 5.11.

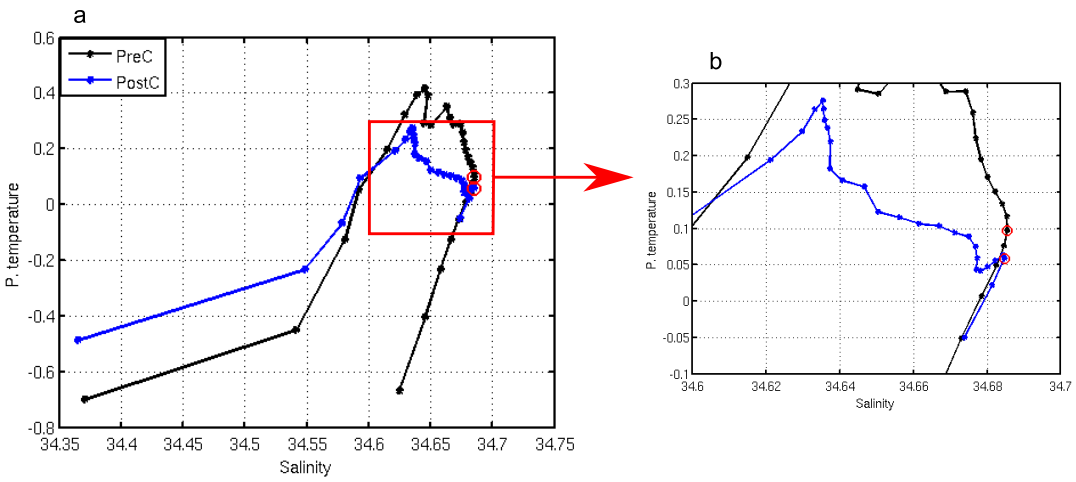

Figure 5.11: Example of the Muench et al. [2009] method (a) at the intersection of 'NS3' with 'EW1' for PRE (black) and POST (blue) simulations. The upper limit of BW layer is determined by the red circle. Panel b is a zoom in of the inflection point area.

To follow BW along the slope, a set of 7 sections following the model grid (Figure 5.12) are chosen to accommodate the slope and avoid the deepest area of the model domain that is directly affected by the BW re-circulation. The southernmost

point of the sections normal to the coast line (called 'NS' sections later) corresponds to the shelf break.

- NS1: west of the Adélie sill to capture BW flowing westward along the slope
- NS2: crossing the western area of the Adélie sill, to capture any BW from the Adélie depression
- NS3: directly east of the Adélie sill to quantify BW coming from the east and eventually preconditioning the Adélie sill outflow
- NS4: along the western corner of the Mertz sill to capture any BW from the Mertz depression
- NS5: eastern most section, aims to check if BW-like come from further east than the Mertz sill
- EW1: in line with the Mertz sill to identify channels used by BW along the slope
- EW2: near the upper continental rise to identify where BW flows and identify the channels downstream

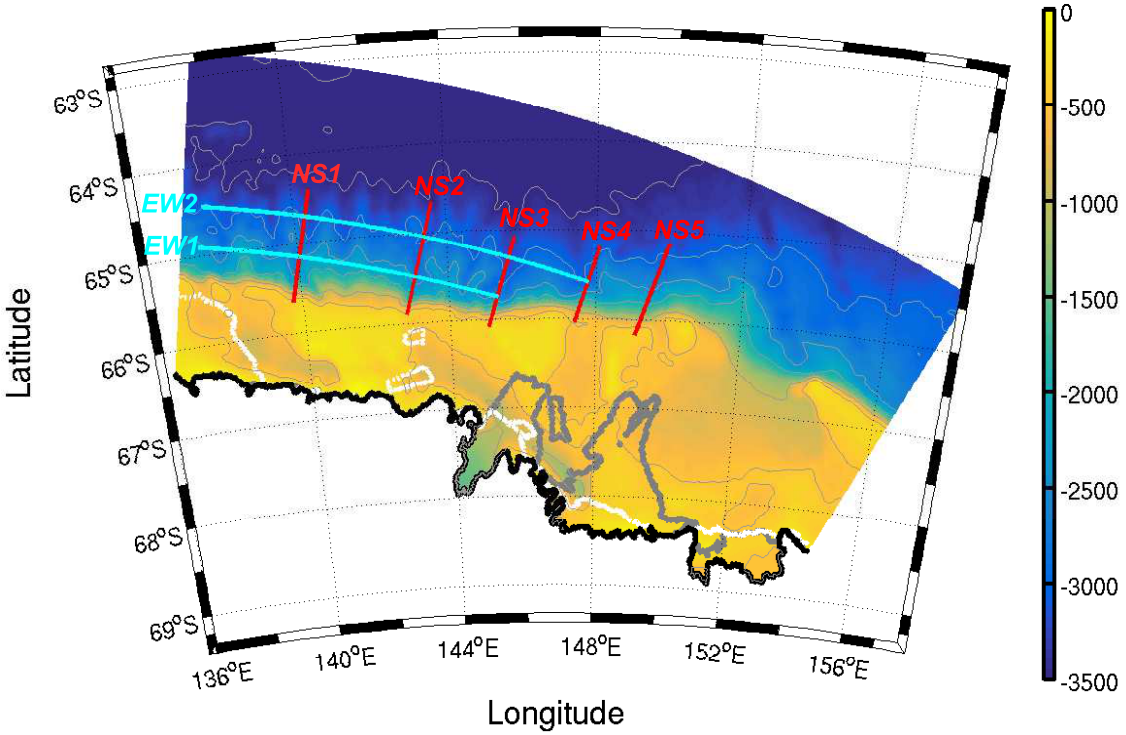

Figure 5.12: Bathymetry of the model domain (m). Grey (white) contours highlight the ice mask for the PRE (POST) simulations. Grey thin contours are bathymetry contours every 500m. Red and cyan lines are sections following the model grid and used in the bottom water layer analysis as described in the text.

5.4.3 Changes in Bottom Water properties and mixing pathways

On the continental shelf, potential density with a surface reference pressure can be used to compare water masses. However, to compare water masses along the slope and deeper that undertake important pressure changes, potential density is not ideal. Instead neutral density (γ^N: kg m^{-3}) is used in this section [Jackett and McDougall 1997]. Table 5.3 and Table 5.4 summarise neutral density, potential temperature and salinity along the defined BW layer along the rise (Table 5.3) and along the slope (Table 5.4). BW thickness estimated with the Muench method, along the 'NS' and 'EW' sections, is shown in Figure 5.13 for both simulations. 'NS4' and 'NS5' are very similar to 'NS3' and are not shown in Figure 5.13.

Along the continental rise, no BW is identified along 'NS3', 'NS4' and 'NS5'. BW

thickness along 'NS1' ('NS2') decreased by ∼90 m (130 m) after calving which corresponds to a decrease of 14% (32%) of the area along the continental rise (Table 5.3). Following the WOCE Hydrographic Programme standards for CTD (Conductivity-Temperature-Depth) sensors temperature and salinity precision (0.0005 °C and 0.001 respectively) [Joyce 1991], the potential temperature along 'NS1' ('NS2') increased by ∼0.09 °C (0.04 °C), and the salinity slightly increased by ∼+0.007 (0.001) for a corresponding decrease in neutral density of ∼0.006 kg m^{-3} (0.005 kg m^{-3}, Table 5.3). As seen on the continental shelf, the most important changes are in the extrema (γ^N_{max} and Θ_{min}). The maximum neutral density within the bottom layer has decreased by ∼0.03 kg m^{-3} for 'NS1' and 'NS2' sections. The minimum potential temperature increased by ∼0.3 °C for 'NS1' and 'NS2', but the maximum salinity is almost unchanged for any of the sections along the continental rise (Table 5.3).

Most of the differences within the BW layer are seen along the slope. The thickness is more variable than along the rise, showing different behaviour in the entrainment of the gravity current down the slope. In the POST simulation, water masses exported from the continental shelf are lighter and are less likely to flow down the slope. As seen between 'NS1' and 'NS2' (Figure 5.13a and b), the thickest area of BW in POST along 'NS2' is at the upper part of the slope near the shelf break, and is entrained westward and downward to 'NS1'. On the other hand, in the PRE simulation the thickest BW along the upper part of the slope is found along 'NS3', as a result of the dense outflow from the Mertz sill. This overflow from the Mertz sill is likely to precondition the mixing with the dense overflow descending from the Adélie sill and explain the thickest BW layer from mid to bottom of the slope along 'NS2' as the gravity current is deflected westward and downward along the slope.

In the POST simulation along 'NS3' a thinner BW layer is seen with an area decreased by ∼46% (Table 5.4), illustrating that the POST production of DSW within the Mertz depression has significantly decreased and is also less likely to flow all the way down to contribute to the production of ALBW. A significant warming along each of the sections is simulated, in particular along 'NS3' (+0.25 °C) associated with a decrease in neutral density of ∼0.05 kg m^{-3} while the salinity has not change significantly (+0.005). However, the most significant changes are seen for the extrema along the BW layer for all the sections. The minimum potential temperature within 'NS3' BW layer has increased by ∼0.9 °C with a decrease in neutral density by ∼0.04 kg m^{-3} (Table 5.4).

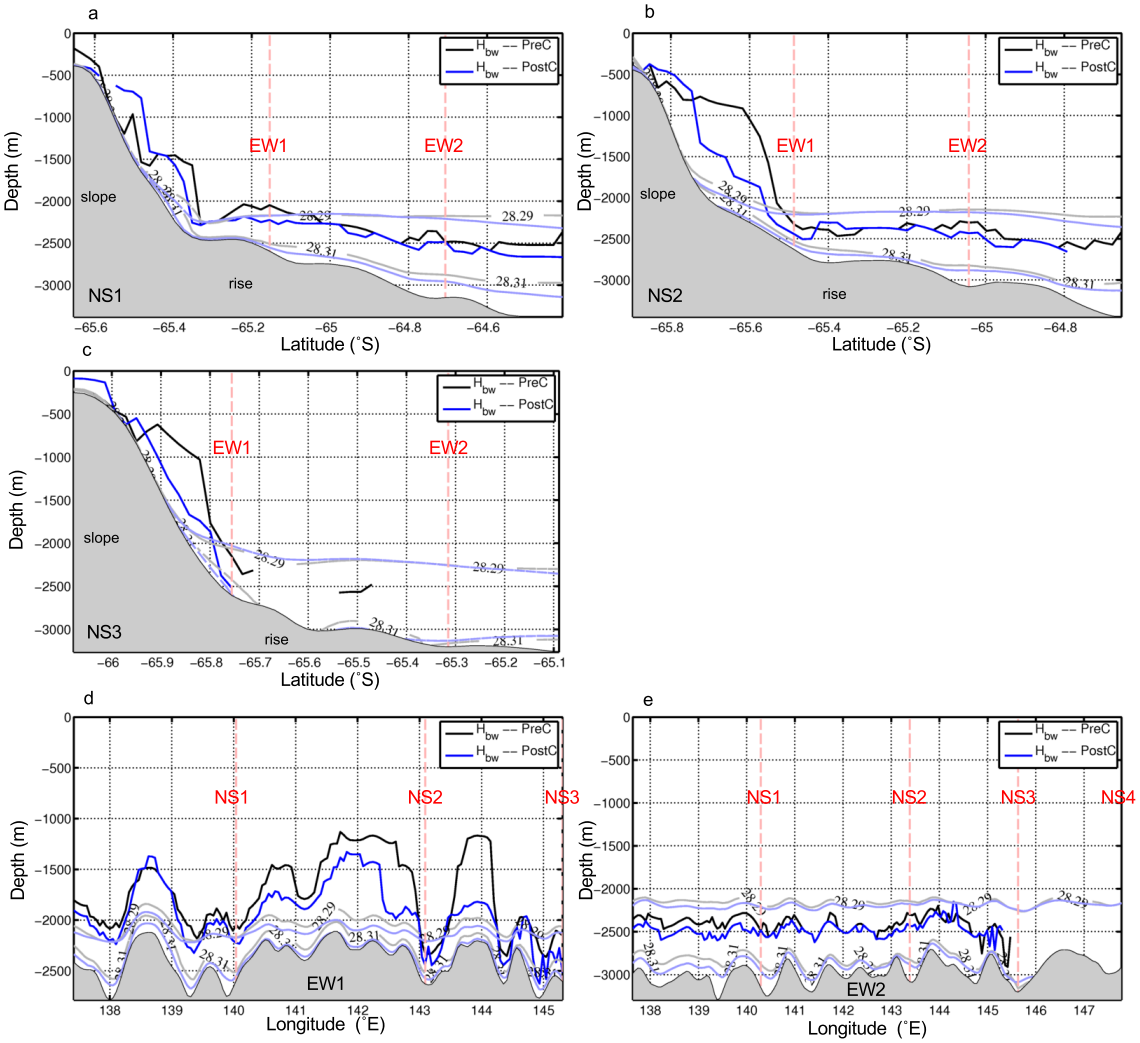

Figure 5.13: Bottom Water thickness (black and dark blue lines) and two neutral density (grey and light blue: kg m^{-3}) contours around the upper limit of the BW layer for 'NS1', NS2', 'NS3', 'EW1' and 'EW2' section, for PRE (black and grey lines) and POST (blue and light blue lines) simulations. Vertical dashed line show the intersection points with the other sections labelled along the line.

On average along the slope and the continental rise, the neutral density has decreased for each section of the POST simulation. Overall potential temperature has increased, in particular the minimum potential temperature within the BW has warmed by up to 0.9 °C on the slope. However, following the standard precision by Joyce [1991] the salinity does not change significantly between both simulations and has even slightly increased in the POST simulation. Along 'NS3' slope, the salinity has increased by 0.005 in average for the entire BW layer, while the maximum salinity decreased by ∼0.01. The densest water mass formed on the shelf has

freshened and become lighter, allowing the dense water to mix more easily with the saltier layer above as the gravity current of BW descends the slope.

In the observations a freshening of the BW layer is seen over recent decades in this area [eg Jacobs 2004; Aoki et al. 2005; Rintoul 2007; Shimada et al. 2012; Purkey and Johnson 2013; Shadwick et al. 2013; van Wijk and Rintoul 2014]. Also, Aoki et al. [2013] notice a negative trend in neutral density (-0.0082 $\pm$ 0.0062 kg m^{-3}) of the BW on the slope near the AGVL along the 140°E averaged over 1994 to 2012. More recent observations from the continental rise at 140°E and about 64.5°S (southern end of SR3 section: Rintoul [1998]) of the ALBW core, before mixing with RSBW, have shown a similar shift in neutral density of about -0.017 kg m^{-3}. This estimation is from an average of the bottom 200 m at a depth of 3000 to 3500 m, using data from 2003 and 2008 for the pre-calving period, and 2012, 2013 and 2015 for the post-calving period. This decrease in density is mainly due to an increase in potential temperature by $\sim$+0.13 °C and a negligeable increase of salinity of 0.002 (S. Rintoul personal communication). The closest section in the model is 'NS1', which shows a decrease in neutral density of 0.006 kg m^{-3} (0.03 kg m^{-3} for the maximum neutral density) along the continental rise, a potential temperature increase of $\sim$0.09 °C and a salinity increase of $\sim$0.007 (Table 5.3).

Table 5.3: Bottom Water properties along the continental rise for each section. $\bar{H}_{BW}$ is the averaged BW thickness estimated via the Muench method [Muench et al. 2009]. Neutral density ($\bar{\gamma}^N$), potential temperature ($\bar{\Theta}$) and salinity ($\bar{S}$) within the BW layer are averaged along the continental rise, and their maximum or minimum are also given in the table.

section	$\bar{H}_{BW}$ (m)	% change in area	$\bar{\gamma}^N$ (m kg^{-3})	γ^N_{max} (m kg^{-3})	$\bar{\Theta}$ (°C)	Θ_{min} (°C)	$\bar{S}$	S_{max}
NS1$_{pre}$	600 ± 180		28.313 ± 0.001	28.358	-0.05 ± 0.02	-0.65	34.674 ± 0.003	34.699
NS1$_{post}$	510 ± 160	-14	28.307 ± 0.001	28.328	0.04 ± 0.02	-0.31	34.681 ± 0.003	34.697
POST-PRE	-90		-0.006	-0.03	+0.09	+0.34	+0.007	+0.002
NS2$_{pre}$	570 ± 200		28.312 ± 0.004	28.362	-0.01 ± 0.06	-0.73	34.679 ± 0.006	34.70
NS2$_{post}$	440 ± 130	-32	28.307 ± 0.002	28.329	0.03 ± 0.03	-0.41	34.680 ± 0.003	34.697
POST-PRE	-130		-0.005	-0.03	+0.04	+0.32	+0.001	+0.003
NS3$_{pre}$	–	–	–	–	–	–	–	–
NS3$_{post}$	–	–	–	–	–	–	–	–
NS4$_{pre}$	–	–	–	–	–	–	–	–
NS4$_{post}$	–	–	–	–	–	–	–	–
NS5$_{pre}$	–	–	–	–	–	–	–	–
NS5$_{post}$	–	–	–	–	–	–	–	–
EW2$_{pre}$	580 ± 120		28.313 ± 0.003	28.370	0.004 ± 0.039	-0.76	34.681 ± 0.004	34.702
EW2$_{post}$	520 ± 100	-12	28.308 ± 0.001	28.329	0.07 ± 0.02	-0.32	34.686 ±0.003	34.698
POST-PRE	-60		-0.005	-0.04	+0.07	+0.44	+0.005	-0.004

Table 5.4: Bottom Water properties along the slope for each section. $\bar{H}_{BW}$ is the averaged BW thickness estimated via the Muench method [Muench et al. 2009]. Neutral density ($\bar{\gamma}^N$), potential temperature ($\bar{\Theta}$) and salinity ($\bar{S}$) within the BW layer are averaged along the slope, and their maximum or minimum are also given in the table.

section	$\bar{H}_{BW}$ (m)	% change in area	$\bar{\gamma}^N$ (m kg^{-3})	γ^N_{max} (m kg^{-3})	$\bar{\Theta}$ (°C)	Θ_{min} (°C)	$\bar{S}$	S_{max}
NS1$_{pre}$	350 ± 290		28.29 ± 0.01	28.40	-0.36 ± 0.06	-1.45	34.629 ± 0.004	34.672
NS1$_{post}$	400 ± 290	+7	28.268 ± 0.009	28.340	-0.35 ± 0.05	-1.02	34.618 ± 0.006	34.679
POST-PRE	+50		-0.02	-0.06	+0.01	+0.43	-0.011	+0.007
NS2$_{pre}$	780 ± 510		28.285 ± 0.007	28.455	-0.40 ± 0.06	-1.87	34.628 ± 0.006	34.668
NS2$_{post}$	510 ± 290	-33	28.26 ± 0.01	28.33	-0.26 ± 0.04	-1.08	34.628 ± 0.004	34.663
POST-PRE	-270		-0.025	-0.125	+0.14	+0.79	0	-0.005
NS3$_{pre}$	430 ± 390		28.297 ± 0.008	28.367	-0.49 ± 0.07	-1.63	34.625 ± 0.007	34.697
NS3$_{post}$	250 ± 150	-46	28.25 ± 0.02	28.33	-0.24 ± 0.05	-0.74	34.630 ± 0.005	34.685
POST-PRE	-180		-0.05	-0.04	+0.25	+0.89	+0.005	-0.01
NS4$_{pre}$	430 ± 360		28.29 ± 0.01	28.43	-0.3 ± 0.08	-1.81	34.639 ± 0.003	34.694
NS4$_{post}$	180 ± 100	-65	28.25 ± 0.02	28.33	-0.17 ± 0.07	-0.85	34.638 ± 0.003	34.670
POST-PRE	-250		-0.04	-0.1	+0.13	+0.96	-0.001	+0.006
NS5$_{pre}$	450 ± 320		28.268 ± 0.008	28.304	-0.19 ± 0.04	-0.65	34.643 ± 0.003	34.692
NS5$_{post}$	200 ± 160	-54	28.25 ± 0.01	28.30	-0.07 ± 0.04	-0.36	34.647 ± 0.001	34.683
POST-PRE	-250		-0.018	-0.006	+0.12	+0.29	+0.004	-0.009
EW1$_{pre}$	660 ± 240		28.302 ± 0.007	28.399	-0.14 ± 0.05	-1.19	34.656 ± 0.003	34.690
EW1$_{post}$	470 ± 180	-28	28.297 ± 0.005	28.347	-0.08 ± 0.05	-0.79	34.659 ± 0.005	34.689
POST-PRE	-190		-0.005	-0.052	+0.06	+0.41	+0.003	+0.001

5.5 Summary

In this chapter, the impact of the Mertz Glacier Tongue (MGT) calving and associated decrease in sea ice production on Dense Shelf Water (DSW) export from the continental shelf is investigated. The set of simulations used in this chapter do not show the evolution of the impact of the calving, but instead simulate the ocean conditions for two stable ice geometries and corresponding air/sea forcing before and after the Mertz Glacier calving event. The impact of a major change in ice shelf configuration together with associated changes in sea ice production is then investigated for a key region in DSW formation that contributes to the AABW formation, the Adélie and George V Land.

The main conclusions of this chapter are as follows:

- The near surface freezing temperature at the bottom of the Adélie depression in both pre- and post-calving simulations shows that HSSW formation continues after calving. However, the salinity in the bottom layer of the model decreases by ∼0.11 in the post-calving simulation, illustrating the weaker polynya forms less and fresher HSSW within the Adélie depression.
- DSW export from the Adélie depression decreased by 80% after calving.
- DSW exported from the Adélie depression in the post-calving simulation is warmer by ∼0.7 °C. The maximum salinity decreased by 0.08 while the average salinity has not changed, illustrating a more homogeneous DSW layer in terms of salinity. This lighter DSW is more likely to mix with the surrounding water masses while descending the slope.
- The bottom potential temperature within the Mertz depression has increased by ∼1 °C and no HSSW is present along the Mertz box during the post-calving simulation, as there is no latent heat polynya near the Mertz depression.
- A westward flow in the post-calving simulation carries warmer water closer to the Mertz Glacier and near the Adélie depression. This pathway was blocked by the icebergs and fast ice in the pre-calving configuration.
- After calving, the Bottom Water (BW) on the slope and continental rise became warmer, saltier, lighter and decreased in thickness. Because less DSW

is produced on the shelf, warm and salty ambient water from the boundary conditions is less diluted but also, DSW is lighter post-calving and mixes more easily with surrounding water masses while descending the slope. Changes in bottom water properties on the continental shelf and along the continental slope and rise will eventually have consequences on AABW properties and production rates downstream.

- No BW is seen in the post-calving simulation in the eastern area of the model domain, illustrating that DSW capable of forming AABW is no longer produced from the Mertz Depression.

Future work is necessary to identify the source of the freshening simulated on the continental shelf. These changes observed between the two model simulations can be caused by the increase of glacial meltwater released by the Mertz Glacier post-calving, or by the decrease of $\sim$36% in sea ice production and brine rejection within the Mertz polynya. At least three additional simulations would be needed to differentiate these two causes:

- Pre- and post-calving configurations without ocean/ice shelf thermodynamics to test the impact of the glacial meltwater on dense water formation for both pre- and post-calving simulation.

- Post-calving ice configuration with pre-calving air/sea forcing to test whether the icescape or the air/sea forcing has the most importance in blocking the westward flow into the Mertz depression.

Chapter 6

Conclusions

6.1 Main findings

This thesis improves our understanding of the causes of variability in the Antarctic Bottom Water (AABW) observed in the Australian-Antarctic Basin, as a result of interactions between sea ice production, ice shelf basal melting, and Dense Shelf Water (DSW) formation and export. The impact of the calving of the Mertz Glacier Tongue (MGT) on basal melting and ocean conditions has also been quantified, with a focus on DSW properties. Some key themes presented through several chapters, are summarised together to give an overview of the sensitivity of DSW formation to sea ice formation and ice shelf basal melting:

1. Interannual variability of the sea ice production, applied to the model via heat and salt fluxes for a stable Adélie and George V Land (AGVL) icescape (before calving), shows that weak polynya activity (sea ice production) over a sustained period reduces DSW formation and export across the shelf break. DSW export across the Adélie sill decreased by 86% between a normal period of polynya activity to a weak polynya state (from 138 mSv to 20 mSv during the peak period). A sustained period of strong polynya activity (high rate of sea ice production) is needed to re-build a large enough volume of DSW to enable the flow across the shelf break into the deep ocean, with a lag of about a year between the change in polynya activity and the response in DSW export (Chapter 2).

2. The MGT melt rate follows a similar pattern to the DSW export due to the interannual variability of the heat and salt fluxes applied at the air/sea

interface of the model. The polynya and associated brine rejection "protect" the ice shelf from the warm mCDW flowing onto the Antarctic continental shelf. Similarly, a weaker polynya activity (weaker cooling) produces a thinner protective band against the mCDW intrusions. The MGT melt rate triples during the sustained period of weak polynya activity (from 1.2 ± 0.4 m yr^{-1} to 3.8 ± 1.5 m yr^{-1}) due to the increased presence of relatively warm water interacting with the base of the ice shelf. Warmer water is present near the MGT in part because of a decrease in High Salinity Shelf Water (HSSW) formation within the Mertz Glacier Polynya. Similarly to the DSW export, the MGT basal melt rate responds after a year of change in polynya activity (Chapter 2).

3. Idealised numerical simulations with a simple two-dimensional domain illustrate the competing roles of the air/sea forcing and warm modified Circumpolar Deep Water (mCDW) intrusion on the ice shelf basal melting and DSW formation (Chapter 3). Depending on the strength of the freezing conditions at the air/sea surface, there is a change in ocean circulation. Two distinct regimes are simulated, driving two modes of sub-ice shelf melting.

   – Ice shelf basal melting driven by HSSW (mode 1 of sub-ice shelf melting), insulates the ice shelf cavity from warm mCDW intrusions by forming an homogeneous water column at surface freezing temperature. Mode 1 of sub-ice shelf melting is associated with formation of DSW and is typical for the Mertz Glacier Polynya region (Chapter 3 and also introduced in Chapter 2).

   – In mode 1, heat can only be transferred to the ice shelf cavity by lateral diffusion across the dynamical barrier, which results from the convection that forms HSSW. The location of the dynamical barrier is dependent on the strength of the surface heat and salt fluxes and inhibits the advection of warm mCDW towards the ice shelf. If the air/sea fluxes are weak (weak sea ice formation) the dynamical barrier moves closer to the ice shelf front (Chapter 3).

   – Subsequently, if weak sea ice production forms a water mass lighter than the inflowing mCDW, there is no dynamical barrier as no HSSW convects to the sea floor. Warm mCDW can flow near the bottom of the domain to the ice shelf cavity, driving mode 2 of sub-ice shelf melting. This mode

of sub-ice shelf melting increases the melt rate of the ice shelf due to the warm mCDW within the ice shelf cavity which increases the thermal forcing at the ocean/ice shelf interface. The buoyant water mass resulting from the ice shelf melting stratifies the water column and insulate the warm bottom mCDW from the surface fluxes. As a result no DSW is formed, which is typical for the Pine Island Glacier region (Chapter 3).

4. Pre- and post- Mertz calving simulations have shown that the change in icescape and associated air/sea forcing (heat and salt fluxes from sea ice production) drive an 89% increase in the area-averaged basal melt rate, after a ∼50% reduction in the MGT area available for melting. Higher melt rates in the post-calving simulation are related to warmer (+0.2 °C) water accessing the Mertz cavity, and an intensification of the velocity within the Mertz cavity due to a 33% increase of the transport into the cavity (Chapter 4). Pre-calving, formation of cold and salty HSSW results in a homogeneous water column in the ice shelf cavity, with potential temperatures at or below the surface freezing point. Post-calving, the water column in the cavity is stratified, with a warmer and saltier layer near the sea floor. The post-calving stratification is therefore similar to the weak polynya regime, with weak formation of HSSW and greater presence of MCDW (Chapter 2 and 4).

5. DSW export changed dramatically between the pre- and post-calving simulations. Within the Adélie depression, the export of DSW decreased by 80%, with changes in water mass properties forming a more homogeneous DSW (warmer, fresher and lighter). Across the Adélie sill, DSW potential density decreases during the post-calving simulation by about 0.03 kg m^{-3} over the climatology, while the densest DSW becomes lighter by about 0.06 kg m^{-3} which is in agreement with preliminary analyses on mooring observations that measure a decrease of about 0.05 kg m^{-3} during the period of the densest DSW export in spring [Snow et al., manuscript in preparation]. Also the model simulates a relatively warm DSW across the Mertz sill (-0.5 °C) during the post-calving simulation, due to mCDW accessing the Mertz depression from the east, and this is unlikely to contribute to the downslope production of AABW (Chapter 5).

6. Analyses of the overflows of exported DSW in the model have shown that the lighter, warmer and fresher DSW formed on the continental shelf in the

post-calving simulation mixes more easily with the salty and warm water mass above to form a lighter, warmer and slightly saltier Bottom Water (BW) that is able to contribute to the Adélie Land Bottom Water (ALBW) formation. Also, no BW is seen in the post-calving simulation in the eastern area of the model domain, confirming that the DSW seen at the Mertz sill post-calving is not able to contribute to ALBW (Chapter 5). Such modifications from the source of ALBW on the continental shelf (DSW) and downstream along the continental slope and rise (BW layer) will have consequences on AABW properties and production rates.

6.2 Future work

The analyses presented in this thesis improve our understanding of the changes in bottom water properties due to changes in polynya activity and major icescape modifications, as a result of the MGT calving event. These results are important for the understanding of the AGVL region but also give information on processes that are responsible for local changes in DSW properties that can impact circumpolar AABW properties. Here are some suggestions for possible future work that would extend and build upon outcomes of this thesis.

- This thesis focuses on the main drivers of the DSW formation, the sea ice formation (brine rejection) and the ocean/ice shelf interactions. However, little discussion around mCDW intrusions is given in this thesis. Even if no changes in mCDW intrusions onto the continental shelf are seen in the analyses presented in the 'realistic' simulations of this thesis, a study of the cross-shelf exchange of DSW and mCDW in both pre- and post-calving conditions is needed to fully understand the behaviour in the model.

- Further investigations with the idealised simulations to understand the threshold between the two regimes of circulation detailed in Chapter 3 is necessary to investigate the possibility of switching between the two regimes under predicted climate change. This threshold has implications on understanding how the heat from warm Circumpolar Deep Water north of the shelf break can flow onto the continental shelf and ultimately interact with the ice shelf [e.g. Klinck and Dinniman 2010; Nøst et al. 2011; St-Laurent et al. 2013; Hattermann et al. 2014; Stewart and Thompson 2015].

- The changes in the pre- and post-calving simulations are driven by both changes in the air/sea fluxes and an increase in glacial meltwater input due to the increase of the ice shelf basal melting. To quantify the impact of the glacial meltwater on DSW formation, the same simulations should be run with no ocean/ice shelf thermodynamics, as has been done in Chapter 2.

Appendix A

Application of satellite-derived surface heat and salt fluxes into ROMS

Heat and salt fluxes are prescribed at the surface of the ocean/ice shelf model used in this study, instead of using a dynamic sea ice model to resolve the fine-scale polynya activity. This appendix describes how these fluxes from Special Sensor Microwave Imager (SSM/I) observations [Tamura et al. 2011] are applied in the modified version of the Regional Ocean Modeling System (ROMS) [Shchepetkin and McWilliams 2005] used in this study. Initially, the simulation in Chapter 2, and presented in Cougnon et al. [2013], followed the parameterisation described by Galton-Fenzi et al. [2012]. Subsequently modifications were made to the transfer of heat and salt during the freezing season and applied to the simulations in Chapters 4 and 5 for reasons described below.

The Tamura et al. [2011; 2016] data set provides monthly (and daily) heat and salt fluxes derived with the assumption that the sum of radiative and turbulent fluxes at the ice surface is balanced by the conductive heat flux in the ice. For this calculation, sea ice thickness estimated with the SSM/I observations using the Tamura et al. [2007] algorithm, that estimates thin ice thickness, and the European Centre for Medium-Range Weather Forecast Re-Analysis data (ERA-Interim) or the National Centers for Environmental Prediction/Department of Energy Re-Analysis data (NCEP2) data are used. In the model, monthly heat and salt fluxes from Tamura et al. [2011; 2016] data set are used in the surface forcing.

During winter (freezing season), negative heat flux (the ocean loses heat from the atmosphere) is set to zero when the surface temperature is equal to the surface freez-

ing temperature. This avoids freezing the surface temperature of the ocean falling below the surface freezing temperature. Also, during summer (sea ice melting season) a factor of 0.5 is applied to the positive heat flux imposed at the surface of the ocean (the ocean gains heat from the atmosphere). An issue using the Tamura et al. [2011; 2016] data set with ROMS is that during the sea ice melting season (spring and summer), the prescribed heat flux is positive (adding heat into the ocean) and drives high surface ocean temperatures in the model. This factor was implemented to avoid parameterising warm surface temperature at the surface of the Southern Ocean. The simulation used in Chapter 2 [Cougnon et al. 2013] uses this 0.5 factor on positive imposed heat flux. However, surface temperature of up to about +8 °C are noticed for the summer months in some areas, away from the coast but over the continental shelf. As a reference, Lacarra et al. [2011] show a maximum surface temperature of 0.25°C in summer, near the shelf break in the Adélie and George V Land region (on the Adélie Bank, see Figure 5.1 – Chapter 5).

At the start of the freezing season (autumn), negative heat flux (cooling) and positive salt flux are forced at the surface of the ocean coincidently in the same time step. In reality, the convection of cold and salty water begins in early autumn due to surface cooling. Only after the remnant heat from the summer mixed layer is eroded, the surface layer maintains its temperature to the freezing point and sea ice begins to grow and rejects salt into the ocean. This autumnal conditioning of the upper surface layer has been explored in the Mertz region by Williams et al. [2011]. In the model, salt is input into the ocean at the same time than the heat flux cools the surface of the ocean, without taking in consideration the sea surface temperature [Cougnon et al. 2013]. Hereinafter this is referred to as the 'OLD' parametrisation.

The pre-calving air/sea fluxes are associated with strong negative heat flux (strong and fast cooling) during the winter months. The warm surface layer is eroded in only a few model time steps. The surface of the ocean is cooled to the surface freezing temperature quickly enough to form a water mass at the surface freezing temperature with the addition of salt that can sink to the sea floor. However, this issue became a problem for the post-calving simulation, where heat and salt fluxes have decreased by 36% in a small area within the most intense polynya area (see Section 5.2.2 – for more details) and by 14-20% over the Mertz Glacier Polynya area [Tamura et al. 2012]. With the 'OLD' scheme, in some areas during weak

freezing scenarios, the heat flux is insufficient to cool the ocean surface to the freezing temperature and yet salt is still injected into the ocean. As a result, warmer water is convected to the sea floor, with implications for oceanic heat input to the base of the ice shelves.

To improve the ocean surface temperature and the salt flux during the freezing season, two modifications have been made in the 'NEW' parameterisation of the model air/sea imposed fluxes:

1. During a melting event (positive heat flux) the ocean surface temperature is limited to a maximum of 0 °C

2. During freezing conditions (negative heat flux), the surface temperature must reach the freezing point before the positive salt flux is applied:
   Let the heat flux to cool the surface of the ocean to $T_f + 0.1$ °C before applying the prescribed salt flux (T_f is the *in situ* freezing temperature) as illustrated in Figure A.1.

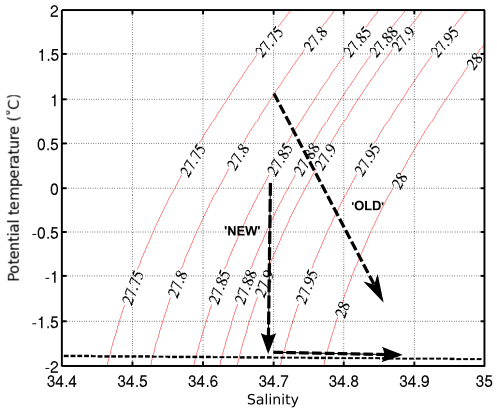

Figure A.1: Schematic showing the effect of the 'NEW' parameterisation of the air/sea fluxes in potential temperature - salinity space compared to the 'OLD'.

To illustrate this issue, an area north of the Mertz Glacier, over the Mertz Bank (for localisation see Figure 5.1), is chosen to analyse heat and salt fluxes into the ocean for both pre- and post-calving simulations using the 'OLD' and the 'NEW' parameterisation used in Chapter 4 and 5 (Figure A.2). Heat and salt fluxes from the Tamura et al. [2011] data simulate sea ice formation north of the Mertz Glacier Tongue (MGT), in the lee of icebergs grounded along the eastern flank of the Mertz Bank (see Figure 1.6). These grounded icebergs are not part of the ice mask of the

model but the surface heat and salt fluxes are imposed in this area simulating the sea ice growth in the lee of these icebergs, north of the MGT.

Heat and salt fluxes used in the model for this area are relatively similar in both pre- and post-calving simulations for the 'OLD' set up (Figure A.2a-d, black line). However, the ocean surface temperature for the same area illustrates some inconstancy (Figure A.2e and f). First of all, during summer months (December, January and February) of the pre-calving simulation (Figure A.2a, c and e, black line) the surface temperature increases up to 5 °C, which is not expected in this area. Besides, in March (month 3) of the pre-calving simulation, the heat flux is negative (Figure A.2a) due to the cooling of the ocean during the sea ice formation, and the salt flux is positive (Figure A.2c) because of the brine rejection. However, the surface temperature is -1.2 °C (Figure A.2e), far from the surface freezing temperature of about -1.9 °C. As the temperature is still above the freezing temperature, sea ice formation should not be simulated, and the salt flux should be equal to zero.

In the post-calving simulation, similar issue is seen but the consequences are more dramatic (Figure A.2b, d and f). For instance, in March the sea ice formation is forced at the surface with negative heat flux (Figure A.2b) and positive salt flux (Figure A.2d), however the surface temperature (Figure A.2f) is -0.23 °C. In addition, from March to October, the temperature is fairly constant around -0.23 °C while salt keeps being injected into the ocean, driving a relatively warm and salty water mass that is dense enough to sink at the sea floor and eventually drive higher ice shelf basal melting if it flows towards the ice shelf cavity.

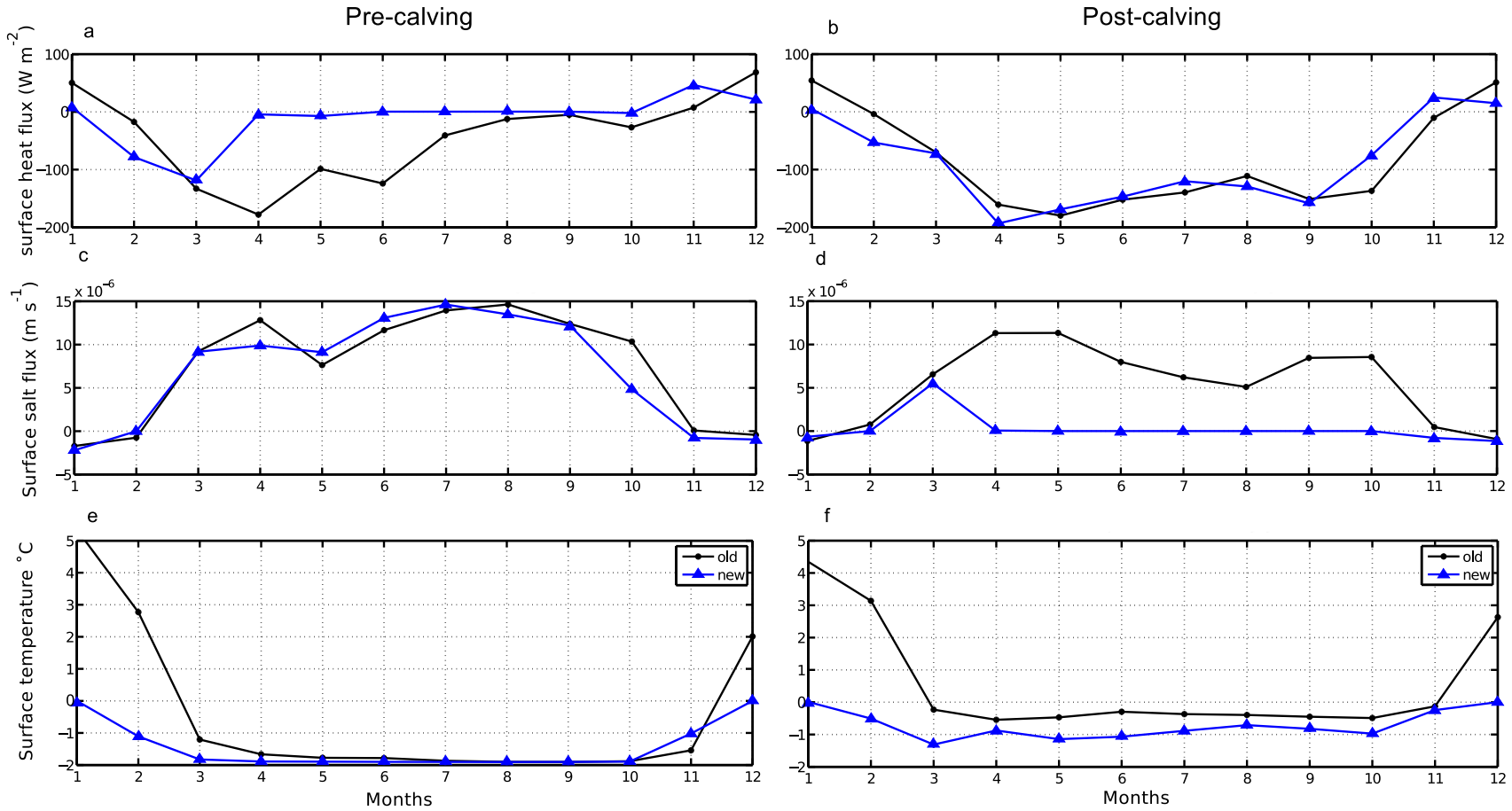

Figure A.2: Surface heat (a and b) and salt (c and d) fluxes for the pre-calving (left panels) and the post-calving (right panels) simulations averaged for a small area over the Mertz Bank (north of the main polynya).

These two modifications are not perfect but are an improvement for the model that simulate more realistic brine rejection within the model during the freezing season (sea ice formation season) as seen on Figure A.2 (blue lines). For instance for the post-calving simulation (Figure A.2b, d and f) during the cooling period (negative surface heat flux) from April till October (month 4 to 10) the surface temperature is around -1 °C, which is greater than the surface freezing temperature, so no salt flux is prescribe in this case (Figure A.2d). An issue with this parameterisation is that it may lead to under estimating the amount of salt injected into the ocean. Ultimately a coupled sea-ice model is needed to resolve the seasonal changes in upper ocean stratification in response to sea ice formation and melt. However, coastal polynya and icebergs are often poorly resolved in models and imposing heat and salt fluxes better resolve the fine-scale polynya in the region, as used in similar studies [eg: Dinniman et al. 2003; 2007; Galton-Fenzi et al. 2012; Hattermann et al. 2014].

Appendix B

Additional Figures

In this appendix extra figures are displayed to give more information about the model. The ice draft for the whole domain is shown for the Mertz pre-calving and post-calving set up, along with the water column thickness beneath the three major ice shelves in the domain. The time series of the surface fluxes within the Mertz Glacier Polynya from the Tamura et al. [2016] data set are also shown, as well as the cumulative sea ice production for the two years used to force the model (2009 and 2012).

B.1 Ice draft

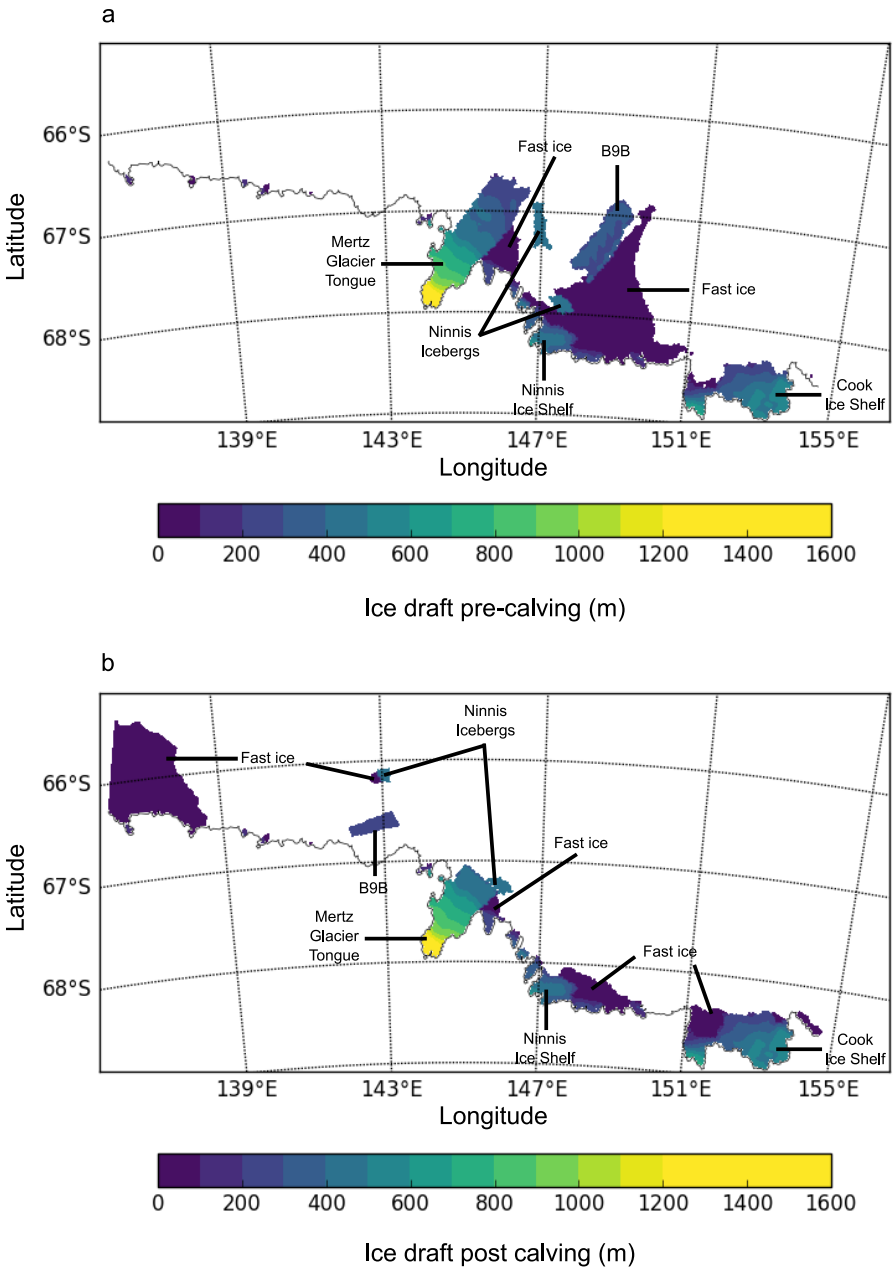

Figure B.1: Ice draft (m) of the PRE (a) and POST (b) simulations detailed in Chapter 4 and 5. Dark blue on the colour bar corresponds to the fast ice with a draft of 10 m, except for the fast ice located east of the Mertz Glacier Tongue which has a draft of 35 m.

B.2 Water column thickness

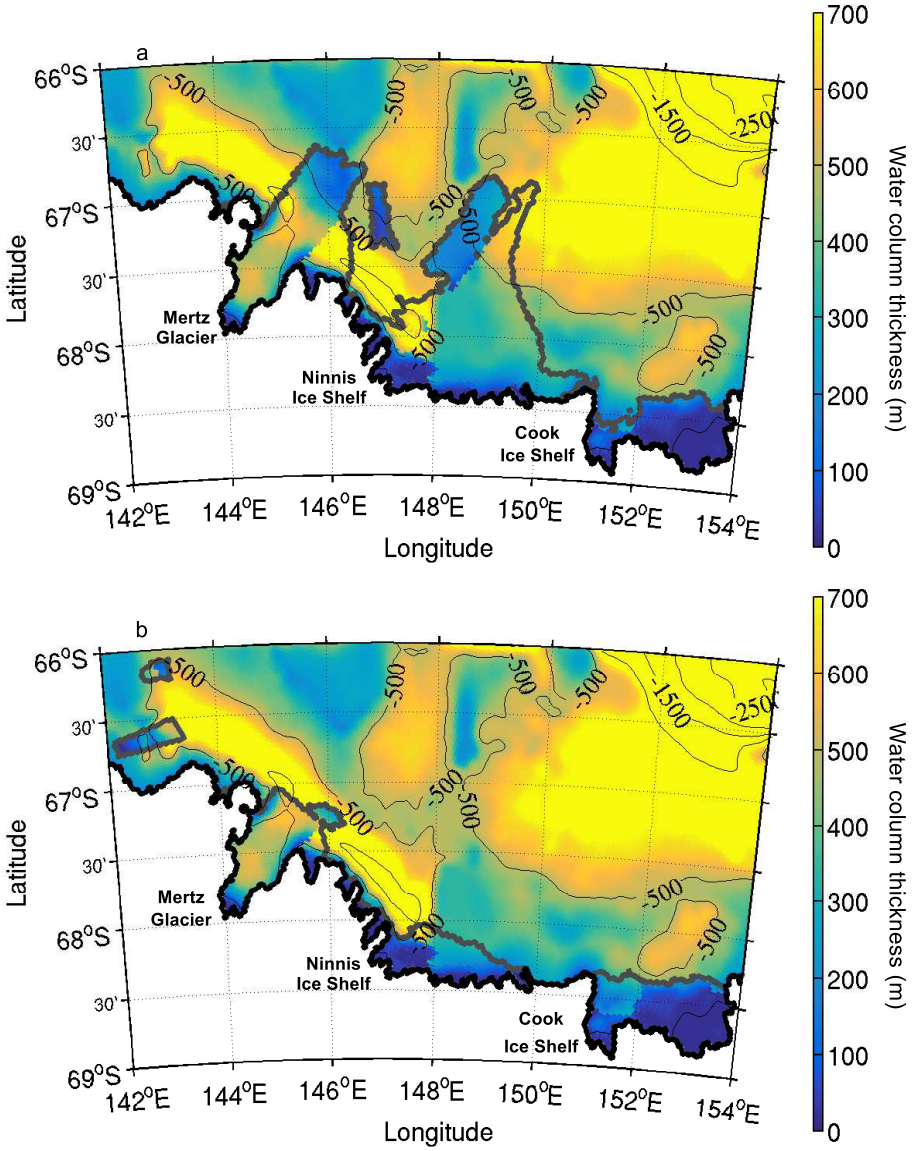

Figure B.2: Water column thickness (m) of the PRE (a) and POST (b) simulations used in Chapter 4 and 5, in the area of the three main ice shelves (Mertz, Ninnis and Cook), with bathymetry contours every 500 m.

B.3 Surface heat and salt fluxes

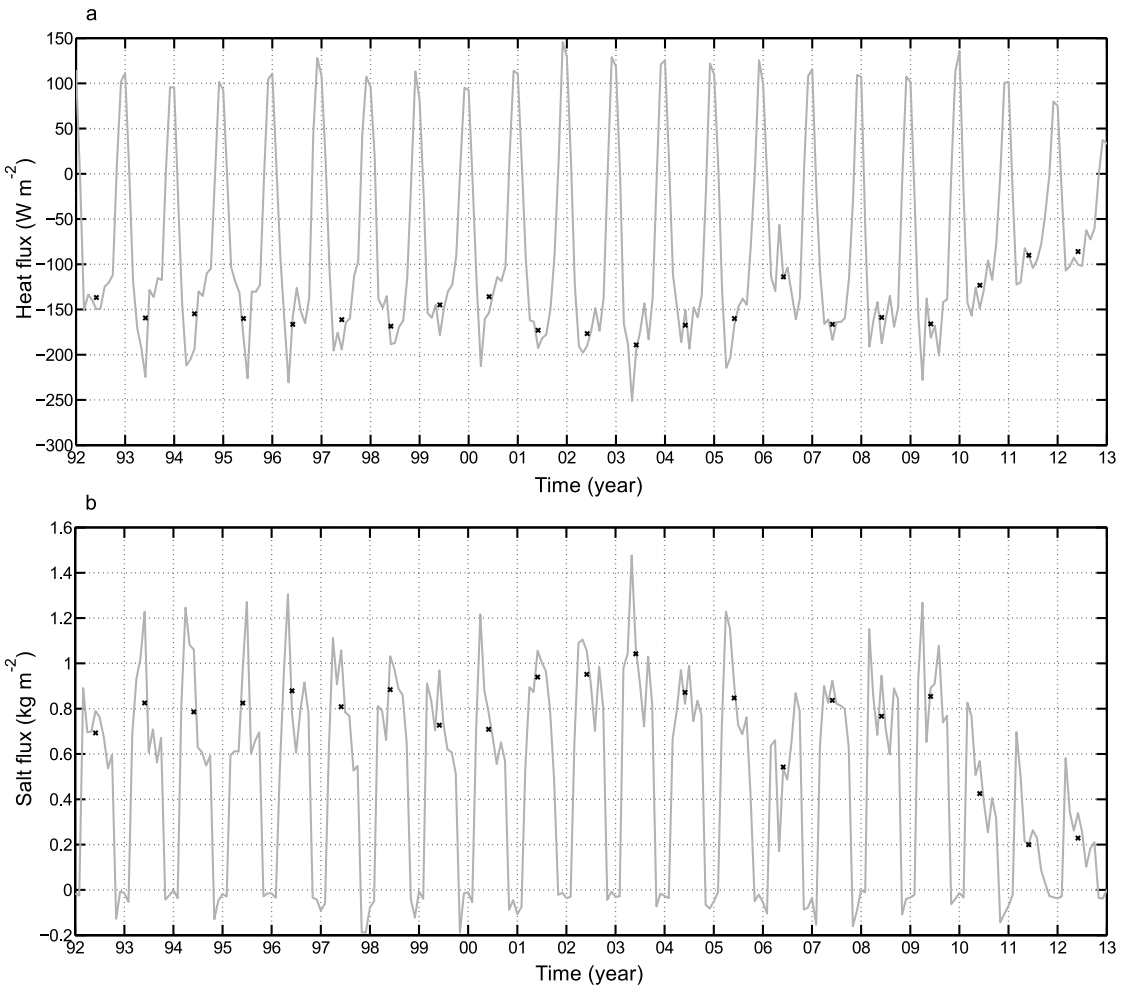

Figure B.3: Monthly surface heat (a) and salt (b) fluxes averaged over the Mertz Glacier Polynya (MGP) from Tamura et al. [2016] data set, with winter time average (May to September inclusive) shown with the crosses.

B.4 Cumulative sea ice production

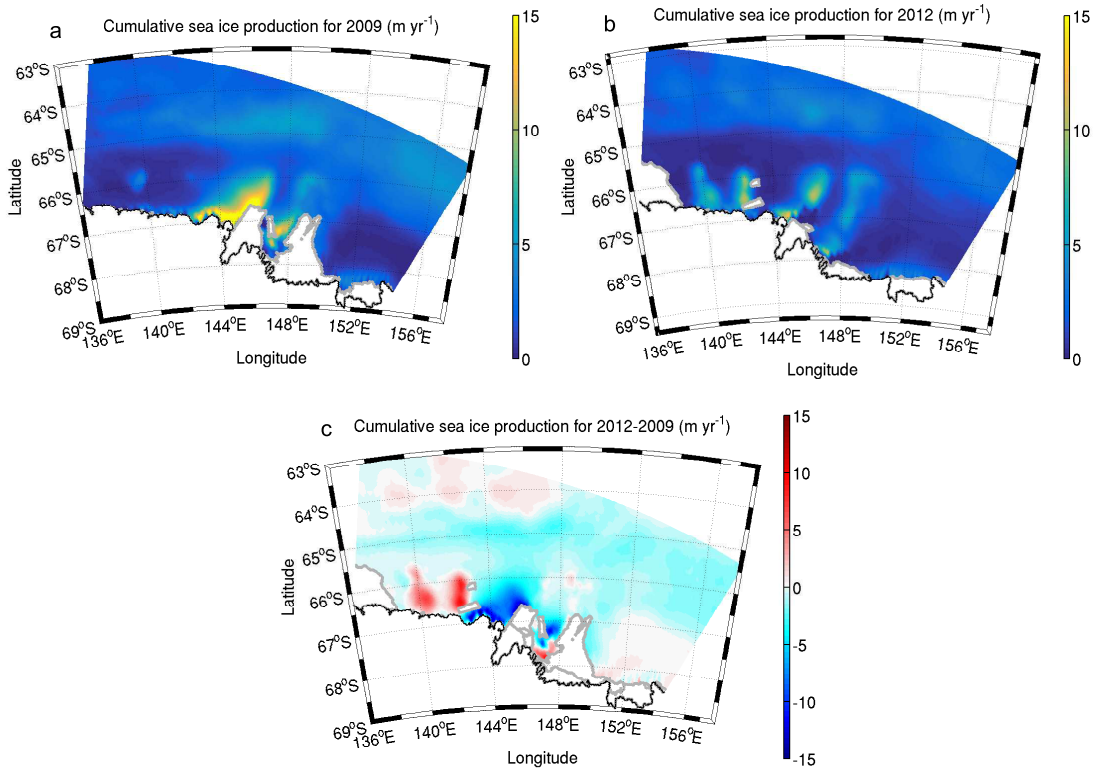

Figure B.4: Cumulative sea ice production (m yr^{-1}) from Tamura et al. [2016] data set for the years of the model forcing; 2009 (a) and 2012 (b). Difference in cumulative sea ice production (2012-2009: c). The black line outlines the coast line in the model and the grey contour outlines the ice mask in the model.

BIBLIOGRAPHY

Adcroft, A., Hill, C., and Marshall, J. (1999). A new treatment of the Coriolis terms in C-grid models at both high and low resolutions. *Monthly Weather Review*, 127(8):1928–1936.

Aoki, S., Kitade, Y., Shimada, K., Ohshima, K. I., Tamura, T., Bajish, C. C., Moteki, M., and Rintoul, S. R. (2013). Widespread freshening in the Seasonal Ice Zone near 140°E off the Adélie Land Coast, Antarctica, from 1994 to 2012. *Journal of Geophysical Research: Oceans*, 118(11):6046–6063.

Aoki, S., Rintoul, S. R., Ushio, S., and Watanabe, S. (2005). Freshening of the Adélie Land Bottom Water near 140°E. *Geophysical Research Letters*, 32.

Arakawa, A. and Lamb, V. R. (1977). Computational design of the basic dynamical processes of the UCLA General Circulation Model. *Methods Computational Physics*, 17.

Azaneu, M., Kerr, R., and Mata, M. M. (2014). Assessment of the ECCO2 reanalysis on the representation of Antarctic Bottom Water properties. *Ocean science discussion*, pages 1023–1091.

Beaman, R. J., O'Brien, P. E., Post, A. L., and Santis, L. D. (2011). A new high-resolution bathymetry model for the Terre Adélie and the George V continental margin, East Antarctica. *Antarctic Science*, 23:95–103.

Berthier, E., Raup, B., and Scambos, T. (2003). New velocity map and mass-balance estimate of Mertz Glacier, East Antarctica, derived from landsat sequential imagery. *Journal of Glaciology*, 49:503–511.

Bindoff, N. L., Rintoul, S. R., and Massom, R. (2000). Bottom water formation and polynyas in Adélie Land, Antarctica. *Papers and Proceedings of the Royal Society of Tasmania*, 133(3):51–56.

Bindoff, N. L., Williams, G. D., and Allison, I. (2001). Sea-ice growth and water mass modification in the Mertz Glacier polynya, East Antarctica, during winter. *Annals of Glaciology*, 33:399–406.

Caburlotto, A., De Santis, L., Zanolla, C., Camerlenghi, A., and Dix, J. K. (2006). New insights into Quaternary glacial dynamic changes on the George V Land continental margin (East Antarctica). *Quaternary Science Reviews*, 25(21-22):3029–3049.

Carmack, E. C. (1977). Water characteristics of the Southern Ocean south of the Polar Front. In *Voyage of discovery*, volume 24, pages 15 – 41. Pergamon.

Cottin, J., Raymond, B., Kato, A., Amélineau, F., Maho, Y. L., Raclot, T., Galton-Fenzi, B., Meijers, A., and Ropert-Coudert, Y. (2012). Foraging strategies of male Adélie penguins during their first incubation trip in relation to environmental conditions. *Marine Biology*.

Cougnon, E. A., Galton-Fenzi, B. K., Meijers, A. J. S., and Legrésy, B. (2013). Modeling interannual dense shelf water export in the region of the Mertz Glacier Tongue (1992–2007). *Journal of Geophysical Research: Oceans*, 118(10):5858–5872.

Craven, M., Allison, I., Fricker, H. A., and Warner, R. (2009). Properties of a marine ice layer under the Amery Ice Shelf, East Antarctica. *Journal of Glaciology*, 55(192):717–728.

Dansereau, V., Heimbach, P., and Losch, M. (2013). Simulation of subice shelf melt rates in a general circulation model: Velocity-dependent transfer and the role of friction. *Journal of Geophysical Research (Oceans)*, 119:1765–1790.

Dee, D., Uppala, S., Simmons, A., Berrisford, P., Poli, P., Kobayashi, S., Andrae, U., Balmaseda, M., Balsamo, G., Bauer, P., et al. (2011). The ERA-Interim reanalysis: Configuration and performance of the data assimilation system. *Quarterly Journal of the Royal Meteorological Society*, 137(656):553–597.

Depoorter, M. a., Bamber, J. L., Griggs, J. a., Lenaerts, J. T. M., Ligtenberg, S. R. M., van den Broeke, M. R., and Moholdt, G. (2013). Calving fluxes and basal melt rates of Antarctic ice shelves. *Nature*, 502(7469):89–92.

Dinniman, M. S., Klinck, J. M., and Hofmann, E. (2012). Sensitivity of Circumpolar Deep Water transport and ice shelf basal melt along the west Antarctic Peninsula to changes in wind. *Journal of Climate*, 25(14):4799–4816.

Dinniman, M. S., Klinck, J. M., and Jr., W. O. S. (2007). Influence of sea ice cover and icebergs on circulation and water mass formation in a numerical circulation model of the Ross Sea, Antarctica. *Journal of Geophysical Research*, 112(C1013).

Dinniman, M. S., Klinck, J. M., and Smith, W. O. (2011). A model study of Circumpolar Deep Water on the West Antarctic Peninsula and Ross Sea continental shelves. *Deep Sea Research Part II: Topical Studies in Oceanography*, 58(13-16):1508–1523.

Dinniman, M. S., Klinck, J. M., and Smith Jr., W. O. (2003). Cross-shelf exchange in a model of the Ross Sea circulation and biogeochemistry. *Deep Sea Research II*, 50:3103–312.

Dutrieux, P., De Rydt, J., Jenkins, A., Holland, P. R., Ha, H. K., Lee, S. H., Steig, E. J., Ding, Q., Abrahamsen, E. P., and Schröder, M. (2014). Strong sensitivity of Pine Island ice-shelf melting to climatic variability. *Science*, 343(6167):174–8.

Flament, T. and Rémy, F. (2012). Dynamic thinning of Antarctic glaciers from along-track repeat radar altimetry. *Journal of Glaciology*, 58(211):830–840.

Fogwill, C., van Sebille, E., Cougnon, E., Turney, C., Rintoul, S., Galton-Fenzi, B., Clark, G., Marzinelli, E., Rainsley, E., and Carter, L. (2016). Under review: Brief Communication: Impacts of a developing polynya off Commonwealth Bay, East Antarctica, triggered by grounding of iceberg B09B. *The Cryosphere*.

Fraser, A. D., Massom, R. A., Michael, K. J., Galton-Fenzi, B. K., and Lieser, J. L. (2012). East Antarctic Landfast Sea Ice Distribution and Variability, 2000-08. *Journal of Climate*, 25(4):1137–1156.

Fretwell, P., Pritchard, H. D., Vaughan, D. G., Bamber, J. L., Barrand, N. E., Bell, R., Bianchi, C., Bingham, R. G., Blankenship, D. D., Casassa, G., Catania, G., Callens, D., Conway, H., Cook, A. J., Corr, H. F. J., Damaske, D., Damm, V., Ferraccioli, F., Forsberg, R., Fujita, S., Gim, Y., Gogineni, P., Griggs, J. A., Hindmarsh, R. C. A., Holmlund, P., Holt, J. W., Jacobel, R. W., Jenkins, A., Jokat, W., Jordan, T., King, E. C., Kohler, J., Krabill, W., Riger-Kusk, M., Langley, K. A., Leitchenkov, G., Leuschen, C., Luyendyk, B. P., Matsuoka, K., Mouginot, J., Nitsche, F. O., Nogi, Y., Nost, O. A., Popov, S. V., Rignot, E., Rippin, D. M., Rivera, A., Roberts, J., Ross, N., Siegert, M. J., Smith, A. M., Steinhage, D., Studinger, M., Sun, B., Tinto, B. K., Welch, B. C., Wilson, D., Young, D. A., Xiangbin, C., and Zirizzotti, A. (2013). Bedmap2: improved ice bed, surface and thickness datasets for Antarctica. *The Cryosphere*, 7(1):375–393.

Frezzotti, M., Cimbelli, A., and Ferrigno, J. (1998). Ice-front change and iceberg behaviour along Oates and George V coasts, Antarctica, 1912-96. *Annals of Glaciology*, 27(167):643–650.

Fukamachi, Y., Rintoul, S. R., Church, J. A., Aoki, S., Sokolov, S., Rosenberg, M. A., and Wakatsuchi, M. (2010). Strong export of Antarctic Bottom Water east of the Kerguelen plateau. *Nature Geoscience*, 3(5):327–331.

Fukamachi, Y., Wakatsuchi, M., Taira, K., Kitagawa, S., Ushio, S., Takahashi, A., Oikawa, K., Furukawa, T., Yoritaka, H., Fukuchi, M., et al. (2000). Seasonal variability of bottom water properties off Adélie Land, Antarctica. *Journal of Geophysical Research: Oceans*, 105(C3):6531–6540.

Gade, H. G. (1979). Melting of ice in sea water: A primitive model with application to the Antarctic ice shelf and icebergs. *Journal of Physical Oceanography*, 9(1):189–198.

Galton-Fenzi, B. K. (2009). *Modelling Ice-Shelf/Ocean Interaction*. PhD thesis, University of Tasmania, Hobart, Tasmania, Australia.

Galton-Fenzi, B. K. (2010). Modelling the interaction between Antarctica and the Southern Ocean. Technical Report 33, Hollis AJ, Day KA (eds.) Centre for Australian Weather and Climate Research Technical Report.

Galton-Fenzi, B. K., Hunter, J. R., Coleman, R., Marsland, S. J., and Warner, R. (2012). Numerical modelling of melt/freeze beneath the Amery Ice Shelf. *Journal of Geophysical Research*, 117(C09031).

Gordon, A. (1991). The Role of Thermohaline Circulation in Global Climate Change. Technical report, Lamont-Doherty Geological Observatory of Columbia University, Palisades, New York.

Gordon, A. L. and Tchernia, P. L. (1972). Waters of the continental margin off Adélie Coast, Antarctica. *Antarctica Oceanology II: The Australian-New Zealand Sector*, pages 59–69.

Greenbaum, J. S., Blankenship, D. D., Young, D. A., Richter, T. G., Legrésy, B., Galton-Fenzi, B. K., and Gim, Y. (2010). Basal characteristics and inferred bathymetry beneath the Mertz Glacier Tongue, Antarctica, from coupled airborne radar sounding and gravity prior to the February 12th 2010 breakup event. In *4th SCAR Open Science Conference - Antarctica: Witness to the Past and Guide to the Future, Buenos Aires, 3-6 August 2010*.

Greenbaum, J. S., Blankenship, D. D., Young, D. A., Richter, T. G., Roberts, J. L., Aitken, A. R. A., Legrésy, B., Schroeder, D. M., Warner, R. C., van Ommen, T. D., et al. (2015). Ocean access to a cavity beneath Totten Glacier in East Antarctica. *Nature Geoscience*, 8(4):294–298.

Griffies, S., Biastoch, A., Bning, C., Bryan, F., Danabasoglu, G., Chassignet, E. P., England, M. H., Gerdes, R., Haak, H., Hallberg, R. W., Hazeleger, W., Jungclaus, J., Large, W. G., Madec, G., Pirani, A., Samuels, B. L., Scheinert, M., Gupta, A. S., Severijns, C. A., Simmons, H. L., Treguier, A. M., Winton, M., Yeager, S., and Yin, J. (2009). Coordinate Ocean-ice Reference Experiment (COREs). *Ocean Modelling*, 26:1–46.

Gudmundsson, G. (2013). Ice-shelf buttressing and the stability of marine ice sheets. *The Cryosphere*, 7(2):647–655.

Gwyther, D., Galton-Fenzi, B., Hunter, J., and Roberts, J. (2013). Simulated melt rates for the Totten and Dalton ice shelves. *Ocean Science Discussions*, 10:2109–2140.

Gwyther, D. E. (2015). *Investigating the Impact of Ocean Warming on Antarctic Ice Shelves*. PhD thesis, University of Tasmania, Hobart, Tasmania, Australia.

Gwyther, D. E., Cougnon, E. A., Galton-Fenzi, B. K., Roberts, J. L., Hunter, J. R., and Dinniman, M. S. (2016). Modelling the response of ice shelf basal melting to different ocean cavity environmental regimes. *Annals of Glaciology*, pages 1–11.

Gwyther, D. E., Galton-Fenzi, B. K., Dinniman, M. S., Roberts, J. L., and Hunter, J. R. (2015). The effect of basal friction on melting and freezing in ice shelf-ocean models. *Ocean Modelling*, 95:38–52.

Hanna, E., Navarro, F. J., Pattyn, F., Domingues, C. M., Fettweis, X., Ivins, E. R., Nicholls, R. J., Ritz, C., Smith, B., Tulaczyk, S., et al. (2013). Ice-sheet mass balance and climate change. *Nature*, 498(7452):51–59.

Hannah, C. G., Dupont, F., and Dunphy, M. (2009). Polynyas and tidal currents in the Canadian Arctic Archipelago. *Arctic*, pages 83–95.

Hasumi, H. (2006). Ocean Component Model (COCO) version 4.0. *CCSR Report 25, Center for Climate System Research, University of Tokyo*.

Hattermann, T., Smedsrud, L. H., Nøst, O. A., Lilly, J. M., and Galton-Fenzi, B. K. (2014). Eddy-resolving simulations of the Fimbul Ice Shelf cavity circulation: Basal melting and exchange with open ocean. *Ocean Modelling*, 82:28–44.

Hellmer, H. H. (2004). Impact of Antarctic ice shelf basal melting on sea ice and deep ocean properties. *Geophysical Research Letters*, 31(10).

Hemery, L. G., Galton-Fenzi, B. K., Améziane, N., Riddle, M. J., Rintoul, S. R., Beaman, R. J., Post, A. L., and Eléaume, M. (2011). Predicting habitat preferences for Anthometrina adriani (Echinodermata) on the East Antarctic continental shelf. *Marine Ecology Progress Series*, 441:105–116.

Herraiz-Borreguero, L., Allison, I., Craven, M., Nicholls, K. W., and Rosenberg, M. A. (2013). Ice shelf/ocean interactions under the Amery Ice Shelf: Seasonal variability and its effect on marine ice formation. *Journal of Geophysical Research: Oceans*, 118(12):7117–7131.

Herraiz-Borreguero, L., Coleman, R., Allison, I., Rintoul, S. R., Craven, M., and Williams, G. D. (2015). Circulation of modified Circumpolar Deep Water and basal melt beneath the Amery Ice Shelf, East Antarctica. *Journal of Geophysical Research: Oceans*, 120(4):3098–3112.

Holland, D. M. and Jenkins, A. (1999). Modelling thermodynamic ice ocean interactions at the base of an ice shelf. *Journal of Physical Oceanography*, 29:1787–1800.

Holland, P. R., Corr, H. F., Vaughan, D. G., Jenkins, A., and Skvarca, P. (2009). Marine ice in Larsen Ice Shelf. *Geophysical Research Letters*, 36(11).

Holland, P. R., Jenkins, A., and Holland, D. M. (2008). The response of ice shelf basal melting to variations in ocean temperature. *Journal of Climate*, 21(11):2558–2572.

Hunter, J. R. (2006). Specification for Test Models of Ice Shelf Cavities. Technical Report June, Antarctic Climate and Ecosystems Cooperative Research Centre, Hobart, Tasmania, Australia.

Jackett, D. R. and McDougall, T. J. (1997). A Neutral Density Variable for the World's Oceans. *Journal of Physical Oceanography*, 27:237–263.

Jacobs, S., Jenkins, A., Giulivi, C., and Dutrieux, P. (2011). Stronger ocean circulation and increased melting under Pine Island Glacier ice shelf. *Nature Geoscience*, 4(8):519–523.

Jacobs, S. S. (2004). Bottom water production and its link with the thermohaline circulation. *Antarctic Science*, 16(4):427–437.

Jacobs, S. S. and Giulivi, C. F. (2010). Large multidecadal salinity trends near the Pacific-Antarctic Continental Margin. *Journal of Climate*, 23(17):4508–4524.

Jacobs, S. S., Helmer, H. H., Doake, C. S. M., Jenkins, A., and Frolich, R. M. (1992). Melting of ice shelves and the mass balance of Antarctica. *Journal of Glaciology*, 38(130):375–387.

Joyce, T. (1991). Introduction to the collection of expert reports compiled for the WHP Programme. *WHP Operations and MethodsJuly 1991*.

Kanamitsu, M., Ebisuzaki, W., Woollen, J., Yang, S.-K., Hnilo, J., Fiorino, M., and Potter, G. (2002). NCEP-DOE AMIP-II reanalysis (R-2). *Bulletin of the American Meteorological Society*, 83(11):1631–1643.

Kitade, Y., Shimada, K., Tamura, T., Williams, G. D., Aoki, S., Fukamachi, Y., Roquet, F., Hindell, M., Ushio, S., and Ohshima, K. I. (2014). Antarctic Bottom Water production from the Vincennes Bay Polynya, East Antarctica. *Geophysical Research Letters*, 41(10):3528–3534.

Klinck, J. M. and Dinniman, M. S. (2010). Exchange across the shelf break at high southern latitudes. *Ocean Science*, 6(2):513–524.

Kusahara, K. and Hasumi, H. (2013). Modeling Antarctic ice shelf responses to future climate changes and impacts on the ocean. *Journal of Geophysical Research: Oceans*.

Kusahara, K., Hasumi, H., and Tamura, T. (2010). Modeling sea ice production and dense shelf water formation in coastal polynyas around East Antarctica. *Journal of Geophysical Research (Oceans)*, 115(C14).

Kusahara, K., Hasumi, H., and Williams, G. D. (2011a). Dense shelf water formation and brine-driven circulation in the Adélie and George V Land region. *Ocean Modelling*, 37(3):122–138.

Kusahara, K., Hasumi, H., and Williams, G. D. (2011b). Impact of the Mertz Glacier Tongue calving on dense water formation and export. *Nature communications*, 2:159.

Lacarra, M., Houssais, M.-N., Herbaut, C., Sultan, E., and Beauverger, M. (2014). Dense shelf water production in the Adélie Depression, East Antarctica, 2004–2012: Impact of the Mertz Glacier calving. *Journal of Geophysical Research: Oceans*, 119(8):5203–5220.

Lacarra, M., Houssais, M.-N., Sultan, E., Rintoul, S., and Herbaut, C. (2011). Summer hydrography on the shelf off Terre Adélie/George V Land based on the ALBION and CEAMARC observations during the IPY. *Polar Science*, 5(2):88–103.

Large, W. G. and Yeager, S. G. (2009). The global climatology of an interannually air-sea flux data set. *Climate Dynamic*, 33:341–364.

Le Brocq, A. M., Payne, A. J., and Vieli, A. (2010). An improved Antarctic dataset for high resolution numerical ice sheet models (ALBMAP v1). *Earth system science data.*, 2(2):247–260.

Le Quéré, C., Raupach, M. R., Canadell, J. G., Marland, G., Bopp, L., Ciais, P., Conway, T. J., Doney, S. C., Feely, R. A., Foster, P., et al. (2009). Trends in the sources and sinks of carbon dioxide. *Nature Geoscience*, 2(12):831–836.

Legrésy, B., Wendt, A., Tabacco, I., Rémy, F., and Dietrich, R. (2004). Influence of tides and tidal current on Mertz Glacier, Antarctica. *Journal of Glaciology*, 50(170).

Lescarmontier, L., Legrésy, B., Young, N., Coleman, R., Testut, L., Mayet, C., and Lacroix, P. (2015). Rifting processes and ice-flow modulation observed on Mertz Glacier, East Antarctica. *Journal of Glaciology*, 61(230):1183–1193.

Lewis, E. L. and Perkin, R. G. (1986). Ice pumps and their rates. *Journal of Geophysical Research*, 91(C10):11756–11762.

Lieser, J. L., Massom, R. A., and Heil, P. (2013). Sea ice reports for the season 2012-2013. Technical report, Antarctic Climate & Ecosystems Cooperative Research Centre, Hobart, Tasmania.

Little, C. M., Gnanadesikan, A., and Oppenheimer, M. (2009). How ice shelf morphology controls basal melting. *Journal of Geophysical Research*, 114(C12).

Liu, Y., Moore, J. C., Cheng, X., Gladstone, R. M., Bassis, J. N., Liu, H., Wen, J., and Hui, F. (2015). Ocean-driven thinning enhances iceberg calving and retreat of Antarctic ice shelves. *Proceedings of the National Academy of Sciences*, 112(11):3263–3268.

Losch, M. (2008). Modeling ice shelf cavities in a z coordinate ocean general circulation model. *Journal of Geophysical Research: Oceans*, 113(C8).

Lumpkin, R. and Speer, K. (2007). Global ocean meridional overturning. *Journal of Physical Oceanography*, 37(10):2550–2562.

Makinson, K., Holland, P. R., Jenkins, A., Nicholls, K. W., and Holland, D. M. (2011). Influence of tides on melting and freezing beneath Filchner-Ronne Ice Shelf, Antarctica. *Geophysical Research Letters*, 38(6):n/a–n/a.

Marchesiello, P., McWilliams, J. C., and Shchepetkin, A. (2001). Open boundary conditions for long-term integration of regional oceanic models. *Ocean modelling*, 3(1):1–20.

Marsland, S. J., Bindoff, N. L., Williams, G. D., and Budd, W. F. (2004). Modeling water mass formation in the Mertz Glacier Polynya and Adelie Depression, East Antarctica. *Journal of Geophysical Research*, 109(C11003).

Marsland, S. J., Haak, H., Jungclaus, J. H., Latif, M., and Röske, F. (2007). Antarctic coastal polynya response to climate change. *Journal of Geophysical Research (Oceans)*, 112(C11).

Massom, R. A., Giles, A. B., Fricker, H. A., Warner, R. C., Legrésy, B., Hyland, G., Young, N., and Fraser, A. D. (2010). Examining the interaction between multi-year landfast sea ice and the Mertz Glacier Tongue, East Antarctica: Another factor in ice sheet stability? *Journal of Geophysical Research*, 115(C12027).

Massom, R. A., Harris, P. T., Michael, K. J., and Potter, M. J. (1998). The distribution and formative processes of latent-heat polynyas in East Antarctica. *Annals of Glaciology*, 27:420–426.

Massom, R. A., Hill, K., Barbraud, C., Adams, N., Ancel, A., Emmerson, L., and Pook, M. J. (2009). Fast ice distribution in Adélie Land, East Antarctica: inter annual variability and implications for emperor penguins Aptenodytes forsteri. *Marine Ecology Progress Series*, 374:243–257.

Massom, R. A., Hill, K. L., Lytle, V. I., Worby, A. P., Paget, M. J., and Allison, I. (2001). Effects of regional fast-ice and iceberg distributions on the behaviour of the Mertz Glacier polynya, East Antarctica. *Annals of Glaciology*, 33:391–398.

Mawson, D. (1915). *The home of the blizzard: being the story of the Australasian Antarctic Expedition 1911-1914*. Heineman, London.

Mayet, C., Testut, L., Legrésy, B., Lescarmontier, L., and Lyard, F. (2013). High-resolution barotropic modeling and the calving of the Mertz Glacier, East Antarctica. *Journal of Geophysical Research: Oceans*, 118(10):5267–5279.

McMillan, M., Shepherd, A., Sundal, A., Briggs, K., Muir, A., Ridout, A., Hogg, A., and Wingham, D. (2015). Increased ice losses from Antarctica detected by CryoSat-2. *Geophysical Research Letters*, 41(11):3899–3905.

Meijers, A., Galton-Fenzi, B. K., Rintoul, S., and Sokolov, S. (in prep). Observations and modeling of dense shelf water production and seasonal circulation near the Mertz Glacier. *Journal of Geophysical Research*, Oceans (in-prep).

Menemenlis, D., Campin, J. M., Heimbach, P., Hill, C., Lee, T., Nguyen, A., Schodlock, M., and Zhang, H. (2008). ECCO2: High resolution global ocean and sea ice data synthesis. *Mercator Ocean Quarterly Newsletter*, 31:13–21.

Moffat, C., Owens, B., and Beardsley, R. C. (2009). On the characteristics of Circumpolar Deep Water intrusions to the west Antarctic Peninsula continental shelf. *Journal of Geophysical Research: Oceans*, 114(C5).

Morales Maqueda, M., Willmott, A., and Biggs, N. (2004). Polynya dynamics: A review of observations and modeling. *Reviews of Geophysics*, 42(1).

Mueller, R. D., Padman, L., Dinniman, M. S., Erofeeva, S. Y., Fricker, H. A., and King, M. A. (2012). Impact of tide-topography interactions on basal melting of Larsen C Ice Shelf, Antarctica. *Journal of Geophysical Research: Oceans*, 117(C5).

Muench, R., Padman, L., Gordon, A., and Orsi, A. (2009). A dense water outflow from the Ross Sea, Antarctica: Mixing and the contribution of tides. *Journal of Marine Systems*, 77(4):369–387.

Nicholls, K. W., Abrahamsen, E. P., Buck, J. J. H., Dodd, P. A., Goldblatt, C., Griffiths, G., Heywood, K. J., Hughes, N. E., Kaletzky, A., Lane-Serff, G. F., McPhail, S. D., Millard, N. W., Oliver, K. I. C., Perrett, J., Price, M. R., Pudsey, C. J., Saw, K., Stansfield, K., Stott, M. J., Wadhams, P., Webb, A. T., and Wilkinson, J. P. (2006). Measurements beneath an Antarctic ice shelf using an autonomous underwater vehicle. *Geophysical Research Letters*, 33(8):2–5.

Nicholls, K. W., Corr, H. F. J., Stewart, C. L., Lok, L. B., Brennan, P. V., and Vaughan, D. G. (2015). A ground-based radar for measuring vertical strain rates and time-varying basal melt rates in ice sheets and shelves. *Journal of Glaciology*, 61(230):1079–1087.

Nicholls, K. W., Østerhus, S., Makinson, K., and Johnson, M. R. (2001). Oceanographic conditions south of Berkner Island, benath Filchner-Ronne Ice Shelf, Antarctica. *Journal of Geophysical Research*, 106:11481–11492.

Nøst, O., Biuw, M., Tverberg, V., Lydersen, C., Hattermann, T., Zhou, Q., Smedsrud, L., and Kovacs, K. (2011). Eddy overturning of the Antarctic Slope Front controls glacial melting in the Eastern Weddell Sea. *Journal of Geophysical Research: Oceans*, 116(C11).

Ohshima, K. I., Fukamachi, Y., Williams, G. D., Nihashi, S., Roquet, F., Kitade, Y., Tamura, T., Hirano, D., Herraiz-Borreguero, L., Field, I., et al. (2013). Antarctic Bottom Water production by intense sea-ice formation in the Cape Darnley polynya. *Nature Geoscience*, 6:235–240.

Olbers, D. and Hellmer, H. (2010). A box model of circulation and melting in ice shelf caverns. *Ocean Dynamics*, 60(1):141–153.

Orsi, A. H. (2010). Oceanography: recycling bottom waters. *Nature Geoscience*, 3(5):307–309.

Orsi, A. H., Johnston, G. C., and Bullister, J. B. (1999). Circulation, mixing and production of Antarctic Bottom Water. *Progress in Oceanography*.

Orsi, A. H. and Wiederwohl, C. L. (2009). A recount of Ross Sea waters. *Deep Sea Research Part II: Topical Studies in Oceanography*, 56(13):778–795.

Paolo, F. S., Fricker, H. A., and Padman, L. (2015). Volume loss from Antarctic ice shelves is accelerating. *Science*, 348(6232):327–332.

Pingree, R. D. and Griffiths, D. K. (1981a). S2 tidal simulations on the north-west European shelf. *Journal of the Marine Biological Association of the United Kingdom*, 61:609–616.

Pingree, R. D. and Griffiths, D. K. (1981b). The N2 tide and semidiurnal amphidromes around the British Isles. *Journal of the Marine Biological Association of the United Kingdom*, 61:617–625.

Pritchard, H. D., Ligtenberg, S. R. M., Fricker, H. a., Vaughan, D. G., van den Broeke, M. R., and Padman, L. (2012). Antarctic ice-sheet loss driven by basal melting of ice shelves. *Nature*, 484(7395):502–5.

Purkey, S. G. and Johnson, G. C. (2013). Antarctic Bottom Water Warming and Freshening: Contributions to Sea Level Rise, Ocean Freshwater Budgets, and Global Heat Gain*. *Journal of Climate*, 26(16):6105–6122.

Reid, J. L. (1979). On the contribution of the Mediterranean Sea outflow to the Norwegian-Greenland Sea. *Deep Sea Research Part A, Oceanographic Research Papers*, 26(11):1199–1223.

Rhein, M. a., Rintoul, S., Aoki, S., Campos, E., Chambers, D., Feely, R., Gulev, S., Johnson, G., Josey, S., Kostianoy, A., et al. (2013). *Observations: ocean. Climate change 2013: The Physical Science Basis. Contribution of Working Group I to the Fifth Assessment Report of the Intergovernmental Panel on Climate Change.* Cambridge University Press, Cambridge, United Kingdom and New York, NY, USA, 255-315, Stocker, T. F., D. Qin, G.-K. Plattner, M. Tignor, S. K. Allen, J. Boschung, A. Nauels, Y. Xia, V. Bex and P. M. Midgley edition.

Rignot, E. (2002). Mass balance of East Antarctic glaciers and ice shelves from satellite data. *Annals of Glaciology*, 34(1):217–227.

Rignot, E., Jacobs, S., Mouginot, J., and Scheuchl, B. (2013). Ice-shelf melting around Antarctica. *Science (New York, N.Y.)*, 341(6143):266–70.

Rignot, E. and Jacobs, S. S. (2002). Rapid bottom melting widespread near antarctic ice sheet grounding lines. *Science*, 296(5575):2020–2023.

Rintoul, S. (1998). On the origin and influence of Adélie Land Bottom Water. In Jacobs, S. and Weiss, R., editors, *Ocean, Ice, and Atmosphere: Interaction at the Antarctic Continental Margin, Antarct. Res. Ser.*, volume 75, pages 151–172. AGU, Washington, D. C.

Rintoul, S. (2007). Rapid freshening of Antarctic Bottom Water formed in the Indian and Pacific oceans. *Geophysical Research Letters*, 34(L06606, doi:10.1029/2006GL028550).

Sabine, C. L., Feely, R. A., Gruber, N., Key, R. M., Lee, K., Bullister, J. L., Wanninkhof, R., Wong, C., Wallace, D. W., Tilbrook, B., et al. (2004). The oceanic sink for anthropogenic CO_2. *Science*, 305(5682):367–371.

Sallée, J.-B., Shuckburgh, E., Bruneau, N., Meijers, A., Bracegirdle, T., Wang, Z., and Roy, T. (2013). Assessment of Southern Ocean water mass circulation and characteristics in CMIP5 models: historical bias and forcing response. *Journal of Geophysical Research: Oceans*.

Schmitz, W. J. (1996). On the World Ocean Circulation: Volume 1: Some Global Features/North Atlantic Circulation. Technical report, Woods Hole Oceanographic Institution, WHOI-96-03, Woods Hole, MA.

Schodlok, M. P., Menemenlis, D., Rignot, E., and Studinger, M. (2012). Sensitivity of the ice-shelf/ocean system to the sub-ice-shelf cavity shape measured by nasa icebridge in Pine Island Glacier, West Antarctica. *Annals of Glaciology*, 53(60):156–162.

Schoof, C. (2007). Ice sheet grounding line dynamics: Steady states, stability, and hysteresis. *Journal of Geophysical Research: Earth Surface*, 112(3):1–19.

Shadwick, E. H., Rintoul, S. R., Tilbrook, B., Williams, G. D., Young, N., Fraser, a. D., Marchant, H., Smith, J., and Tamura, T. (2013). Glacier tongue calving reduced dense water formation and enhanced carbon uptake. *Geophysical Research Letters*, 40(5):904–909.

Shchepetkin, A. F. and McWilliams, J. C. (2005). The Regional Oceanic Modeling system (ROMS): a split-explicit, free-surface, topography-following-coordinate oceanic model. *Ocean Modelling*, 9:347–404.

Shimada, K., Aoki, S., Ohshima, K., and Rintoul, S. (2012). Influence of Ross Sea Bottom Water changes on the warming and freshening of the Antarctic Bottom Water in the Australian-Antarctic Basin. *Ocean Science*, 8(4):419–432.

Siedler, G., Griffies, S. M., Gould, J., and Church, J. A. (2013). *Ocean Circulation and Climate: a 21st Century Perspective*, volume 103. Academic Press.

Smith, W. H. and Sandwell, D. T. (1997). Global sea floor topography from satellite altimetry and ship depth soundings. *Science*, 277(5334):1956–1962.

St-Laurent, P., Klinck, J. M., and Dinniman, M. S. (2013). On the Role of Coastal Troughs in the Circulation of Warm Circumpolar Deep Water on Antarctic Shelves. *Journal of Physical Oceanography*, 43(1):51–64.

Steig, E. J., Ding, Q., Battisti, D. S., and Jenkins, A. (2012). Tropical forcing of Circumpolar Deep Water Inflow and outlet glacier thinning in the Amundsen Sea Embayment, West Antarctica. *Journal of Glaciology*, 53(60):19–28.

Stewart, A. L. and Thompson, A. F. (2015). Eddy-mediated transport of warm Circumpolar Deep Water across the Antarctic Shelf Break. *Geophysical Research Letters*, 42(2):432–440.

Talley, L. D. (2011). *Descriptive physical oceanography: an introduction*. Academic press.

Tamura, T. and Ohshima, K. I. (2011). Mapping of sea ice production in the Arctic coastal polynyas. *Journal of Geophysical Research*, 116(C7):C07030.

Tamura, T., Ohshima, K. I., Fraser, A. D., and Williams, G. D. (2016). Sea ice production variability in Antarctic coastal polynyas. *Journal of Geophysical Research: Oceans*.

Tamura, T., Ohshima, K. I., Markus, T., Cavalieri, D. J., Nihashi, S., and Hirasawa, N. (2007). Estimation of Thin Ice Thickness and Detection of Fast Ice from SSM/I Data in the Antarctic Ocean. *Journal of Atmospheric and Oceanic Technology*, 24(10):1757–1772.

Tamura, T., Ohshima, K. I., and Nihashi, S. (2008). Mapping of sea ice production for Antarctic coastal polynyas. *Geophysical Research Letters*, 35.

Tamura, T., Ohshima, K. I., Nihashi, S., and Hasumi, H. (2011). Estimation of Surface Heat/Salt fluxes associated with Sea Ice growth/melt in the Southern Ocean. *Geophysical Research Letters*, 35.

Tamura, T., Williams, G. D., Frazer, A. D., and Ohshima, K. I. (2012). Potential regime shift in decreased sea ice production after the Mertz Glacier calving. *Nature communications*, 3:826.

Timmermann, R., Brocq, A. L., Deen, T., Domack, E., Dutrieux, P., Galton-Fenzi, B., Hellmer, H., Humbert, A., Jansen, D., Jenkins, A., Lambrecht, A., Makinson, K., Niederjasper, F., Nitsche, F., Nøst, O. A., Smedsrud, L. H., and Smith, W. H. F. (2010). A consistent dataset of Antarctic ice sheet topography, cavity geometry, and global bathymetry. *Earth Syst. Sci. Data*, 3:231–257.

van Wijk, E. and Rintoul, S. (2014). Freshening drives contraction of Antarctic Bottom Water in the Australian Antarctic Bassin. *Geophysical Research Letters*, pages 1657–1664.

Wåhlin, A., Yuan, X., Björk, G., and Nohr, C. (2010). Inflow of Warm Circumpolar Deep Water in the Central Amundsen Shelf. *Journal of Physical Oceanography*, 40(6):1427–1434.

Walker, D. P., Brandon, M. A., Jenkins, A., Allen, J. T., Dowdeswell, J. A., and Evans, J. (2007). Oceanic heat transport onto the Amundsen Sea shelf through a submarine glacial trough. *Geophysical Research Letters*, 34(2).

Wendler, G., Ahlna, K., and Lingle, C. S. (1996). On Mertz and Ninnis glaciers, East Antarctica. *Journal of Glaciology*, 42(142).

Wendler, G., Stearns, C., Weidner, G., Dargaud, G., and Parish, T. (1997). On the extraordinary katabatic winds of Adélie Land. *Journal of Geophysical Research: Atmospheres*, 102(D4):4463–4474.

Williams, G. D., Aoki, S., Jacobs, S. S., Rintoul, S. R., Tamura, T., and Bindoff, N. L. (2010). Antarctic Bottom Water from the Adélie and George V Land coast, East Antarctica (140-149°E). *Journal of Geophysical Research*, 115(C04027).

Williams, G. D. and Bindoff, N. L. (2003). Wintertime oceanography of the Adélie Depression. *Deep Sea Research Part II*, 50:1373–1392.

Williams, G. D., Bindoff, N. L., Marsland, S. J., and Rintoul, S. R. (2008). Formation and export of dense shelf water from the Adélie Depression, East Antarctica. *Journal of Geophysical Research (Oceans)*, 113(C12):4039.

Williams, G. D., Hindell, M., Houssais, M. N., Tamura, T., and Field, I. C. (2011). Upper ocean stratification and sea ice growth rates during the summer-fall transition, as revealed by Elephant seal foraging in the Adélie Depression, East Antarctica. *Ocean Science*, 7:185–202.

Wunsch, C., Heimbach, P., Ponte, R., and Fukumori, I. (2009). The global general circulation of the ocean estimated by the ECCO-Consortium. *Oceanography*, 22:88–103.